5-13-2022

Phase-field simulations of the precipitation kinetics and microstructure development in nickel-based superalloys

Caleb O. Yenusah
Mississippi State University, cyenusah@gmail.com

Phase-field simulations of the precipitation kinetics and microstructure development in nickel-based superalloys

By

Caleb O. Yenusah

Approved by:

Tonya W. Stone (Major Professor/Graduate Coordinator)
Yucheng Liu (Co-Major Professor)
Lei Chen (Co-Major Professor)
Youssef Hammi
Like Li
Jason M. Keith (Dean, Bagley College of Engineering)

A Dissertation
Submitted to the Faculty of
Mississippi State University
in Partial Fulfillment of the Requirements
for the Degree of Doctor of Philosophy
in Mechanical Engineering
in the Department of Mechanical Engineering

Mississippi State, Mississippi

May 2022

Name: Caleb O. Yenusah

Date of Degree: May 13, 2022

Institution: Mississippi State University

Major Field: Mechanical Engineering

Major Professor: Yucheng Liu

Title of Study: Phase-field simulations of the precipitation kinetics and microstructure development in nickel-based superalloys

Pages in Study: 111

Candidate for Degree of Doctor of Philosophy

The continual research and development of nickel-based superalloys is driven by the global demand to improve efficiency and reduce emissions in the aerospace and power generation industries. Integrated Computational Material Engineering (ICME) is a valuable tool for reducing the cost, time, and resources necessary for the development and optimization of the mechanical properties of materials. In this work, an ICME approach for understanding the microstructure development and optimizing the mechanical properties in nickel-based superalloys is employed. Most nickel-based superalloys are precipitate strengthened by either the γ' phase, γ'' phase, or both. Therefore, understanding the precipitation kinetics and morphological evolution of these phases is critical for evaluating their hardening effects during heat treatment and degradation of the microstructure during high temperature service. To this end, a phase-field model has been developed to analyze the nucleation, growth and coarsening kinetics during isothermal and non-isothermal aging conditions. Utilizing the phase-field model, the γ'' phase microstructure development and its coherency strengthening effect in Inconel 625 is studied. A novel multistage aging strategy to optimize the γ'' phase strengthening effect and reduce aging times for Inconel 625 is proposed. Secondly, the coarsening kinetic and microstructure development of γ'

strengthening phase in nickel-based superalloys is studied, with the goal of understanding the effect of elastic inhomogeneity on the microstructure evolution at high volume fractions of the γ' phase. The result shows deviation of the coarsening kinetics from the classical Lifshitz-Slyozov-Wagner (LSW) due to the effect of elastic inhomogeneity, highlighting the need for incorporating elastic energy into coarsening theories.

DEDICATION

This dissertation is dedicated to my parents Mr. Maji Yenusah, M.D. and Mrs. Ojonogecha Yenusah for their support and encouragement throughout my life.

ACKNOWLEDGEMENTS

I would like to express my sincere gratitude to my advisors, Dr. Tonya W. Stone, Dr. Yucheng Liu, and Dr. Lei Chen for their constant guidance, advice, and encouragement through the course of my Ph.D. graduate study. None of this work would be possible without their supervision. I thank Dr. Youssef Hammi and Dr. Like Li for serving on my committee and providing insightful comments. I am grateful to Dr. Mark Horstemeyer for his mentorship through the course of my graduate studies. I thank Dr. Yanzhou Ji at Pennsylvania State University for helping me learn and implement the phase-field method. I am grateful for the financial support from the National Science Foundation (NSF), in United States under an award CMMI 1662854 that made this research possible. Finally, I express my gratitude to the Center for Advanced Vehicular Systems (CAVS) and High Performance Computing Collaboratory (HPC2) at Mississippi State University for providing the computational resource needed to carry out this research.

TABLE OF CONTENTS

LIST OF TABLES

LIST OF FIGURES

CHAPTER I

INTRODUCTION

1.1 Motivation

Materials microstructures are compositional or structural inhomogeneities that develop during processing. The properties of a material are dictated by its microstructure, which are in turn dependent on the processing conditions. Therefore, knowledge of the evolution of microstructure during processing is important in correctly predicting the mechanical properties of the resulting material. Given the multiscale nature of microstructures, fundamental understanding and representation of each scale and connections of the scales is required to accurately predict the mechanical properties that results from processing (Figure 1.1). Integrated Computational Materials Engineering (ICME) paradigm, embodies the idea of multiscale modeling of process, structure, property, and performance of materials [1, 2]. Density Functional Theory (DFT) provides electronic scale properties of materials, atomic properties are calculated using molecular dynamics (MD) analysis, phase-field representations provide the description of microstructure at the mesoscale, Internal Scale Variable (ISV) models are used to describe the macroscale, and Finite Element Analysis is used to predict the mechanical properties of materials [1, 2]. ICME is a valuable tool for reducing the cost, time, and resources necessary for the development and optimization of the mechanical properties of materials [3, 4, 5, 6, 7, 8]. The future of ICME could leverage machine learning technology to promote understanding of process-structure-property relations of materials, reducing the computational cost of physics based ICME [9, 10].

Microstructure development such as precipitation of secondary phases has proven to be a valuable mechanism to improve the mechanical properties of metallic alloys. To improve the effectiveness and efficiency of the processing conditions needed to achieve the optimal precipitation characteristics, knowledge of the microstructure development during the precipitation process in required. Concentrating on the precipitation kinetics in metallic alloys at the mesoscale, the current research will be focused on the application of the phase-field method to quantitatively model the precipitate microstructure development and evolution in metallic alloys, specifically nickel-based superalloys, given their technological importance in the aerospace, chemical processing, power, and marine industries.

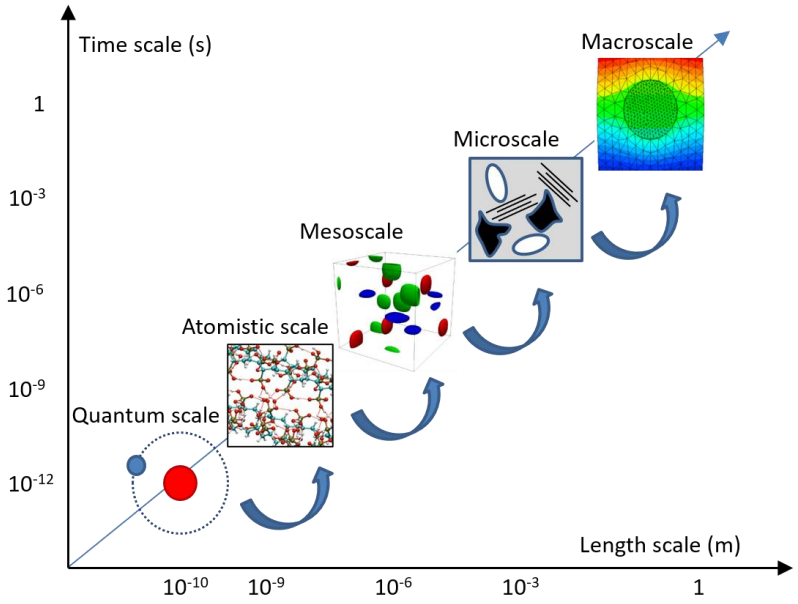

Figure 1.1 Multiscale modeling paradigm for simulating and linking the microstructure of materials to their mechanical properties.

1.2 Precipitation strengthening in metallic alloys

Precipitation strengthening is one of the techniques used for increasing the mechanical strength of metals. The process uses heat treatment to facilitate the formation of secondary particles (precipitates) in the metal's grain structure that help hinder the motion of dislocation, or defects in a crystal's lattice and thereby strengthening the alloy [11]. Precipitation kinetics can be divided into nucleation, growth and coarsening stages [12]. During the nucleation stage, nuclei of the precipitating phase form in the supersaturated matrix due to spatially localized composition fluctuation. The growth stage is categorized by the diffusional growth of a precipitate by solute transfer from the surrounding matrix without competing with the growth of other particles. After sufficient depletion of the solute in the matrix during the growth stage, the free growth of individual precipitates ceases, and the coarsening regime starts. During coarsening, the growth of larger particles continues at the expense of smaller particles which dissolve due to diffusive mass transfer from smaller particles to larger ones.

Experimental and theoretical understanding of each stage of the precipitation process is critical for evaluating precipitate hardening effects and improving the yield strength of the alloy during heat treatment. To optimize the heat treatment strategy and accelerate alloy design, predicting precipitate hardening effects via theoretical analysis or computer simulations is a promising complement to trial-and-error-based experiments, making it possible to efficiently explore the whole heat treatment design space, reducing the alloy development time and cost. The ability to determine the precipitate hardening effects significantly relies on the correct prediction of the evolution of precipitate morphology, size, volume fraction, and spatial distribution during heat treatment. Different models have been developed to concurrently capture all stages of precipitation reaction. Most prominent among them are Kampmann & Wagner Numerical (KWN)

method [12], Svoboda-Fischer-Fratzl-Kozeschnik (SFFK) framework [13], and Johnson-Mehl-Avrami-Kolmogorov (JMAK) kinetics [14]. However, given that these models are a mean description of the precipitation kinetics, they do not capture the details of the precipitation morphology and interactions. Furthermore, contributions from elastic energy and other sources that may impact the precipitation kinetics (e.g. applied stress or radiation) are not captured by these models. Therefore, it is beneficial to capture the precipitate kinetics and morphology using a multiscale approach.

1.3 Multiscale modeling of precipitation kinetics and microstructure

Given the multiscale nature of microstructures, fundamental understanding and representation of each scale and connections of the scales is required to accurately predict the microstructure development in materials.

1.3.1 Atomic scale calculations

The microstructure of materials exhibits different characteristics at varying length scales. Atomic scale variations prevail at the angstrom scale giving rise to the structure that are noticeable at the meso- and micro-scales. First-principles calculations based on density functional theory (DFT) have proven to be a valuable tool for probing the properties of materials at the atomic scale. Since these first-principles calculations are parameter-free, requiring knowledge of only the atomic species and crystal structure, they allow for accurate assessment of several thermodynamic quantities such as formation energy, interfacial energy, surface energy, elastic constants, and lattice parameters can be evaluated at 0K [15]. With the aid of the Debye model [16], supercell phonon computations [17], or Monte Carlo simulations [18], these quantities, as well as other thermodynamic variables like entropy, heat capacity, thermal expansion, and Helmholtz free

energy, may be determined at finite temperatures. In the absence of calorimetry data, first-principles calculations can be used to compute compound formation enthalpies and supplement alloy thermodynamic databases used in CALPHAD (computational thermodynamic) phase diagram modeling [19]. Once an accurate parameterization of the alloy energetics has been derived from first-principles calculations, scale bridging approaches such as mixed-space cluster expansion approach, Monte Carlo simulations, or diffuse-interface model can be used to predict precipitate morphologies [18, 20]. Furthermore, first-principle calculations of stacking fault energy and generalized stacking fault energy surface offer significant insights for understanding the dislocation-precipitate interactions and the deformation modes of precipitates under externally applied stress [21]. Correct prediction of diffusional precipitation kinetics relay on the accurate quantification of the atomic diffusivities in the alloy. First-principles calculations can also be used to calculate the self- and impurity diffusivities of alloying elements in the matrix phase [22, 23]. Also, atomic scale calculations can be used to elucidate the mechanical behavior of materials [24, 25, 26, 27, 28].

1.3.2 Phase-field simulations

The phase-field method has emerged as a powerful computational technique for modeling and predicting mesoscale morphological and microstructure evolution in materials. It describes a microstructure using a set of conserved and/or non-conserved field variables that are continuous across the interfacial regions. Phase-field method has seen widespread application in the modeling of solidification, solid-state transformation, grain growth and coarsening, electromigration, dislocation dynamics, etc. [29, 30]. The reasons for its widespread use are:

(1) The advantage of avoiding the explicit tracking of interfaces through the introduction of a diffuse interface.

(2) The capability to accurately predict complex morphological evolution of precipitates without any presumption on their shape or mutual distribution.

(3) The general formulation of the phase-field model allows for the inclusion of all energy terms such as chemical, interfacial, strain, magnetic, and electrostatic energy and inclusion of external fields such as applied stress, electrical, temperature, and magnetic fields that contribute to the evolution of the microstructure of interest [29].

(4) The fundamental thermodynamic and kinetic information can be used as the input parameters to the model.

(5) The results from the phase-field method are usually 2D or 3D visual representations of microstructure, which often matches experimental observations; hence, the model can be viewed as a computational time series micrograph of the evolving microstructure.

The phase-field method was simultaneously developed for solidification and solid-state transformation. Herein, a brief review of its development for solid state transformation, specifically precipitation is reviewed. The work of Cahn and his co-workers is considered the first introduction of the phase-field concept for solid-state transformation and chemical ordering. Their work resulted in the renowned Cahn-Hilliard [31] and Allen-Cahn [32] equations which have found widespread application in phase-field models till date. By solving the Onsager microscopic diffusion equations, Khachaturyan established the concentration wave theory, which eventually evolved into microscopic phase-field models for ordering [33, 34]. Kachaturyan also established the microelasticity theory, which has proven a significant tool in analyzing the coherency strain energy in phase transformations and is incorporated in phase-field simulation of precipitation [33]. The microscopic discrete phase-field models were applied to simulate microstructure of ordered precipitates [35, 36]. However, a few precipitates exhibit an ordered crystal structure in metallic

alloy systems. Many of the precipitates display complicated crystal structures that are different from the matrix phase. Also, the simulation size scale of the microscopic phase-field model is limited because the atomic scale order structure must be resolved. Besides, the atomic interaction parameters are also difficult to obtain in many alloy systems. To address the limitations of microscopic discrete phase-field models, Chen *et al*. [37] introduced continuous phase-field variables for precipitation [38] and other solid-state transformation modeling [39, 40], replaced the Onsager equations with the Cahn-Hilliard [31] and Allen-Cahn [32] equations, and included the elastic energy contribution using microelasticity theory [33]. These enhancements to the phase-field method resulted in successful simulation of microstructure development during the precipitation process in metallic alloys under isothermal heat treatments or applied external stress [41, 42, 43]. To improve the phase-field model's predictive capability for modeling precipitation microstructure development in realistic materials systems, energetics descriptions from CALPHAD-type thermodynamic databases were introduced, as well as parameterization of the phase-field model using first-principles calculations [44, 45]. The work of Vaithyanathan *et al*. on the morphology of θ' precipitates in AlCu alloys showed the predictive capability of the first-principle parameterized phase-field models, demonstrating the effect of anisotropy of interfacial energy, misfit strains, and interfacial mobility on the morphology, interaction, and growth kinetics of θ' precipitates in AlCu alloys (Figure 1.2). As computational power and resources became available, 3D phase-field simulation incorporating CALPHAD-type thermodynamic databases became more accessible, giving the capability of understanding the precipitation kinetics with full spatial resolution, although still computationally intensive [46, 47]. Shen *et al*. [48] showed that for quantitative phase field modeling with material-specific parameters as inputs, when considering the individual processes such as growth or coarsening, one can always diffuse the

interface and hence increase the simulation length scale by adjusting certain parameters in the model without altering the kinetics. The work of Kim *et al*. [49] to remove the extra double-well potential of composition due to the equal composition assumption at interfaces [50, 51] by considering local equilibrium with equal diffusion chemical potential, rather than equal composition, at interfaces, serve to greatly increase the length scale of phase field simulations of precipitation kinetics. Although the precipitation kinetics and morphology of the precipitates could be simulated with great accuracy and simulation results comparable well with experimental results, the quantitative description of the nucleation process was not considered in these simulations. Simmons *et al*. [52, 53] developed the Poisson seeding algorithm, in which viable nuclei are introduced in the simulation microstructure at a rate matched by the observed nucleation rate to facilitate the modeling of nucleation and growth kinetics during non-isothermal heat treatment conditions. Jokisaari *et al*. [54] simplified the nucleation algorithm for a coupled conserved–nonconserved phase field model putting forth the order-parameter-only seeding method which naturally satisfies the conservation law for the conserved order parameter.

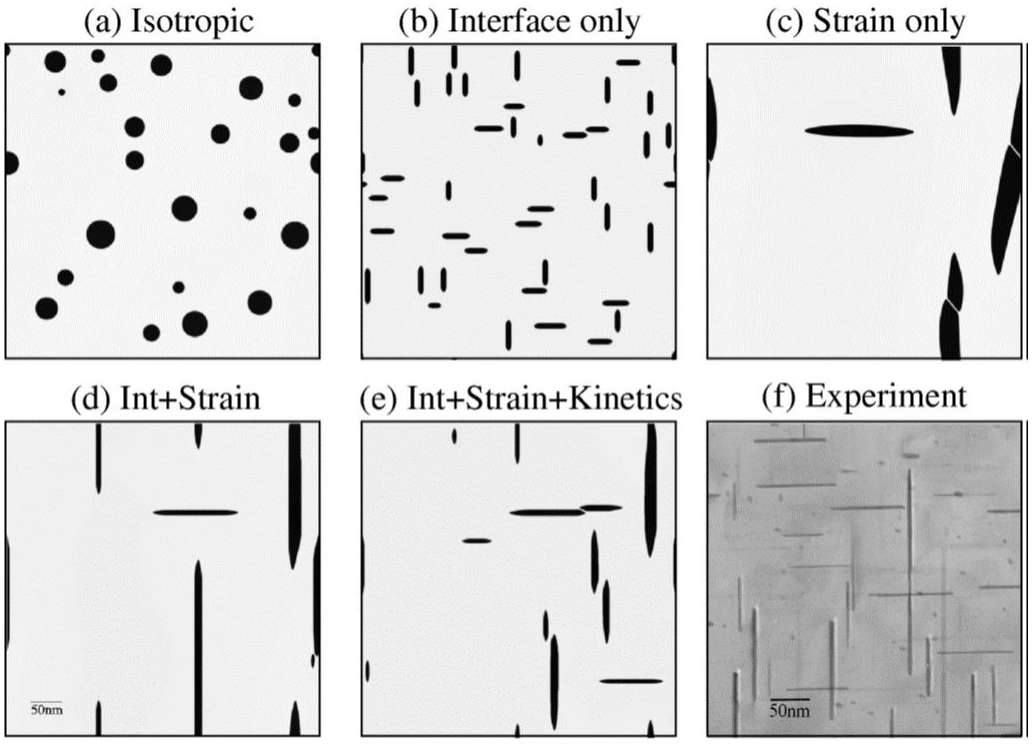

Figure 1.2 Phase-field simulation of θ' precipitates morphology demonstrating different anisotropic contributions on its morphology development. (a) No anisotropies (b) only interfacial energy anisotropy (c) only misfit strain energy anisotropy (d) the combination of interfacial energy and misfit strain energy anisotropies (e) all anisotropies are considered, including the anisotropies in interfacial energy, misfit strain energy and interface mobility anisotropy (f) comparison with experimental observations. Adapted from [18].

To formulate a phase-field model for precipitation modeling, different phases of interest (precipitates and matrix phases) must be represented with physical variables that distinguish between them. Because precipitate phases often have different crystal structures and compositions than matrix phases, these physical variables typically are the structure/order parameters and the species concentration. After which, a free energy functional is constructed as a function of the specified physical parameters:

$$F = \int_V f(\eta_1, \eta_2, \dots, \eta_n, X_1, X_2, \dots, X_n, \nabla\eta_1, \nabla\eta_2, \dots, \nabla\eta_n, \nabla X_1, \nabla X_2, \dots, \nabla X_n, P, T, \dots)\, dV \tag{1.1}$$

where η_i are the non-conserved order parameters identifying the precipitates and the matrix phases and X_i are the conserved parameter describing the species concentration. The exact form of the free energy density f is problem specific. Typically for a precipitation model it includes: (1) a potential with local minima in the two or more coexisting phases (for instance a "double-well" or "double-obstacle" potential [55]), (2) the gradient terms of the order parameters, $\nabla\eta_i$ and the species concentration, ∇X_i that relates the energetic contribution of interfaces and (3) bulk energy density terms (e.g. chemical free energy, elastic strain energy, etc.) as a function of the physical variables η_i an X_i, and local state variables (e.g. temperature, T, pressure P, etc.). Since the evolution of microstructure is driven by a reduction of the system free energy, the evolution of the conserved fields, X_i , and non-conserved fields, η_i can be obtain from the functional (or variational) derivatives of the free energy functional as:

$$\frac{\partial X_i}{\partial t} = \nabla \cdot \left(M_i \nabla \frac{\delta F}{\delta X_i} \right) = \nabla \cdot \left[M_i \nabla \left(\frac{\partial f}{\partial X_i} - \nabla \cdot \frac{\partial f}{\partial \nabla X_i} \right) \right] \tag{1.2}$$

$$\frac{\partial \eta_i}{\partial t} = -L_i \frac{\delta F}{\delta \eta_i} = -L_i \left(\frac{\partial f}{\partial \eta_i} - \nabla \cdot \frac{\partial f}{\partial \nabla \eta_i} \right) \tag{1.3}$$

Eq. (1.2) and Eq. (1.3) are usually referred to as the Cahn-Hilliard [31] and Allen-Cahn [32] (or time-dependent Ginzburg-Landau) equations, respectively. Parameters M_i and L_i are positive mobilities which may represent atomic or interfacial mobilities and may depend on local state variables and interface orientation.

CHAPTER II

PRECIPITATION IN NICKEL-BASED SUPERALLOYS

2.1 Introduction

The global demand to improve efficiency and reduce emissions in the aerospace and power generation industries serve as the driving factor for the continual development of new gas turbine engines with higher operating temperatures and faster rotational speeds (thus higher operating loads due to centrifugal forces) [56]. However, the realization of these new engines is limited by the speed of innovation of materials that can meet the design requirements. Some of these material requirements include excellent static and cyclic mechanical strength at high operating temperatures, superb corrosion and oxidation resistance, resistance to mechanical degradation over extended periods of time [57]. The materials that meet these stringent requirements are commonly referred to as the superalloys. There are three classes of superalloys, defined by their majority constituent, i.e., the Co-based, Ni-based, and Fe-based alloys. Ni-based superalloys are the most widely utilized of all three types of superalloys, owing to their superior high-temperature characteristics compared to Fe-based superalloys and their lower cost compared to Co-based superalloys [57, 58].

2.2 Nickle-based superalloys

Nickel-based superalloys generally account for 40–50% of the overall weight of an aviation engine and are commonly found in the combustor and turbine sections, where high temperatures are maintained throughout operation [59]. Intensive alloy and process development operations

over the last several decades have resulted in alloys that can withstand temperatures ranging from 1050 ℃ to 1200 ℃, which is nearly 90% of the material's melting point [59, 60]. Ni-based superalloys have been developed and utilized to achieve high strength, low density, increased environmental resistance, processability, fabricability, and cost effectiveness. Other design factors include Young's modulus, Poisson's ratios, thermal conductivity, heat capacity, and thermal expansion [61]. Ni-based superalloys can compose of ten or more alloying elements. The metallurgy of Ni-based alloys comprises of the face-centered cubic (FCC) matrix and the other elements are added to improve the mechanical properties of the alloys. These include precipitation strengthening elements (Al, Ta, and Ti), solid solution strengthening elements (Cr, Co, Mo, W, Re, and Ru), and grain boundary strengthening elements (C and B) [62]. Note that some of these elements can serve multiple roles. For example Co and Mo can also serve to increase the corrosion resistance of the alloy [57, 63], Al and Cr may both strengthen the alloy matrix and improve oxidation resistance [62], and Re, W, Ta, Mo and Ru contribute to creep-strengthening [57]. The high alloying contents and complex chemistry of Ni-based superalloys results in the precipitation of secondary phases, some of which are beneficial or detrimental to the mechanical properties.

The precipitation of secondary phases in Ni-based superalloys occur due to sufficient thermodynamic driving force (for nucleation and evolution), resulting from the supersaturation of the matrix phase (commonly known as the γ phase) at a given temperature. Precipitation usually occurs during the cooling stages after solidification, heat treatment, or in-service operation at high temperatures. Given that the formation of secondary phases has significant impact on the mechanical properties of the alloys, it is advantageous to understand the formation process and evolution of these phases for the purpose of either obtaining a desirable microstructure (consequently, mechanical properties) or for monitoring the evolution/degradation of the

microstructure of the alloy during in-service use. Some of the commonly observed secondary phases in Ni-based superalloys are γ', γ'' , δ, η, topologically-close-packed (TCP) phases, and carbides.

2.2.1 Gamma prime (γ') phase

The γ' phase in nickel-based alloys have been extensively studied in the literature because of it beneficial precipitation hardening effects. It has an ordered $L1_2$ type FCC unit cell structure with a chemical formula in the form of A_3B and a cube-cube orientation relationship with the matrix of $\{100\}_{\gamma}//\{100\}_{\gamma'}$ and $<010>_{\gamma}//<100>_{\gamma'}$ [63]. The γ' phase is usually found in Ni-based superalloys containing considerable amounts of aluminum and titanium where it forms as $(Ni)_3(AlTi)$ with nickel atoms occupying the face of the FCC unit cell and aluminum/titanium at the corners [57]. In terms of structure and lattice parameters, the γ' phase and the disordered austenitic matrix phase γ are quite comparable. However, the difference in lattice parameters between the γ/γ' phase results in misfit strain responsible for the morphology of the γ' precipitate microstructure. Figure 2.1 shows the morphology of γ' in Ni-based superalloys with different degree of lattice misfit strain. When the γ' precipitate phase display almost identical lattice parameters (less than 1% lattice misfit) to the γ matrix phase, the two phases are considered coherent. The kind and amount of additional alloying elements in the alloy have a considerable influence on the lattice misfit. Coherency and lattice misfit are key alloy design factors for preserving microstructural stability, particularly at higher temperatures.

The γ' precipitates with a volume fraction more than 70%, when combined with a solid-solution reinforced γ matrix, give exceptional mechanical strength. Alloys containing up to 75% volume fraction of γ' phase have been examined. Murakumo *et al*. [64] revealed that an optimal creep rupture strength is attained at a volume fraction of γ' phase of about 70-75%. Alloys with such

higher volume fraction of γ' phase are designed by raising the concentrations of Al, Ti, and Ta. The remarkable high mechanical strength of Ni-based alloys at high fractions of their melting temperature is attributed to the presence of a large volume fraction of γ' precipitates which geometrically constrain plastic deformation through a process known as anti-phase-boundary (APB) hardening [65, 66]. That is, dislocations traveling through the γ matrix cannot enter a γ' precipitate without first forming an APB, posing a significant energy barrier and hindering dislocation motion. Furthermore, the constraint on dislocation movement is exacerbated by the fact that the antiphase boundary generated for γ' is of such high energy that dislocations must travel in pairs, so that the subsequent dislocation decreases system energy by erasing the APB created by the first. Due to their size, distribution, and coherency, γ' particles can further boost deformation resistance by forcing dislocations to bow or loop around rather than cut through the precipitates (Orowan strengthening) [63].

The γ' phase formation usually occurs by disperse nucleation in the γ matrix, followed by growth and coarsening. To optimize the strengthening effect of the γ' phase, alloys are subjected to carefully designed heat treatments in order to produce a homogeneous intragranular precipitate population with an average particle size where the yield mechanism transitions from shearing of γ' precipitates by weakly coupled pair of dislocations to strongly coupled pair of dislocations [66, 67]. This morphology provides maximal hardening because, in the weakly coupled regime, the critical shear stress needed to cut through a precipitate of radius r has a dependency of $r^{1/2}$, but in the strongly coupled regime, the dependence is $r^{-1/2}$ [68, 69]. When the governing functions characterizing the two regimes are equated, the precipitate size that gives the greatest resistance to dislocation shearing is determined to be $r \approx 2T/\gamma_{APB}$ where T is the absolute temperature and γ_{APB} is the anti-phase boundary energy.

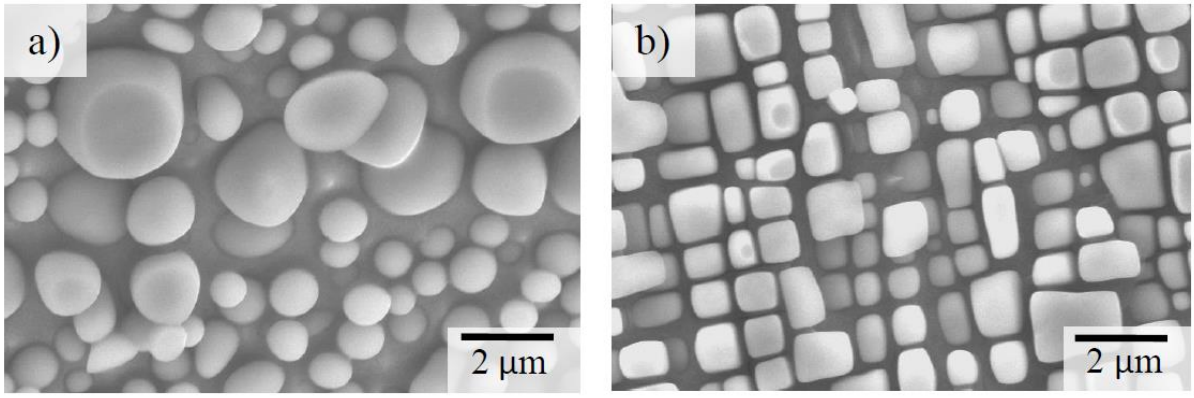

Figure 2.1 Effect of lattice misfit on the morphology of γ' precipitates. (a) Near-zero misfit (b) 0.005 misfit. Adapted from [70]

2.2.2 Gamma double prime (γ'') phase

The γ'' phase in Ni-based alloy possesses a body-centered tetragonal (BCT) $D0_{22}$ unit cell structure with the chemical formula of Ni_3Nb. As shown in Figure 2.2a, the unit cell of γ'' possesses a c_0 parameter (tetragonal length) approximately twice that of the a_0 cubic lattice parameter of the γ phase, making it possible for the coherent precipitation of γ'' in the γ matrix. The γ'' phase exhibits a tetragonal-cubic orientation relationship with the γ matrix of $\{100\}_{\gamma''}//\{100\}_{\gamma}$ and $[001]_{\gamma''}//<100>_{\gamma}$. Therefore, three orientation variants with different {100} habit planes will appear under normal precipitation conditions. The γ'' precipitates have a plate-shaped morphology and are distributed in three spatial orientations perpendicular to one another (Figure 2.2b). For this phase to develop, a nickel-based alloy must include significant amounts of niobium and iron content. The principal strengthening mechanism of the γ'' phase is coherent hardening caused by tetragonal matrix distortion, which results in large coherency stresses that impede dislocation motion [71]. The hardening effect imparted by the γ'' phase is greater than that by the γ phase at the same volume fraction and can occur at much smaller precipitate size [71]. As a result, careful

heat treatment design is required to maximize the coherent hardening effect of the γ'' phase, as it has been reported that the phase begins to lose full coherency with the matrix at major radii greater than 25nm and complete coherency loss occurs at major radii greater than 130nm. [72, 73, 74].

Furthermore, because of the three orientation variants of γ'', the microstructure may be manipulated by aging under stress. For example, by aging a [001] crystal under a tensile elastic stress, will produce a microstructure where only the γ'' particle variant with major axis normal to the [001] stress axis is present. When the stress direction is reversed, the two variants lying parallel to the stress axis are favored at the expense of the former [71, 75]. Manipulation of the variants present in the microstructure offers another degree of freedom for optimizing the mechanical properties of γ'' strengthened nickel-based superalloys. Zhang *et al*. [76] reported that "single-variant" microstructure can be used to tailor the creep resistant of the material. It should be emphasized that in most nickel-based superalloys, the γ'' phase is metastable. As a result, γ'' will convert to the stable δ phase during heat treatment or service operation, which is not as favorable to the mechanical properties of the material. As a result, Ni-based alloys strengthened by the γ'' phase are often utilized at temperatures below 650℃, where the γ'' phase coarsening kinetics are sluggish.

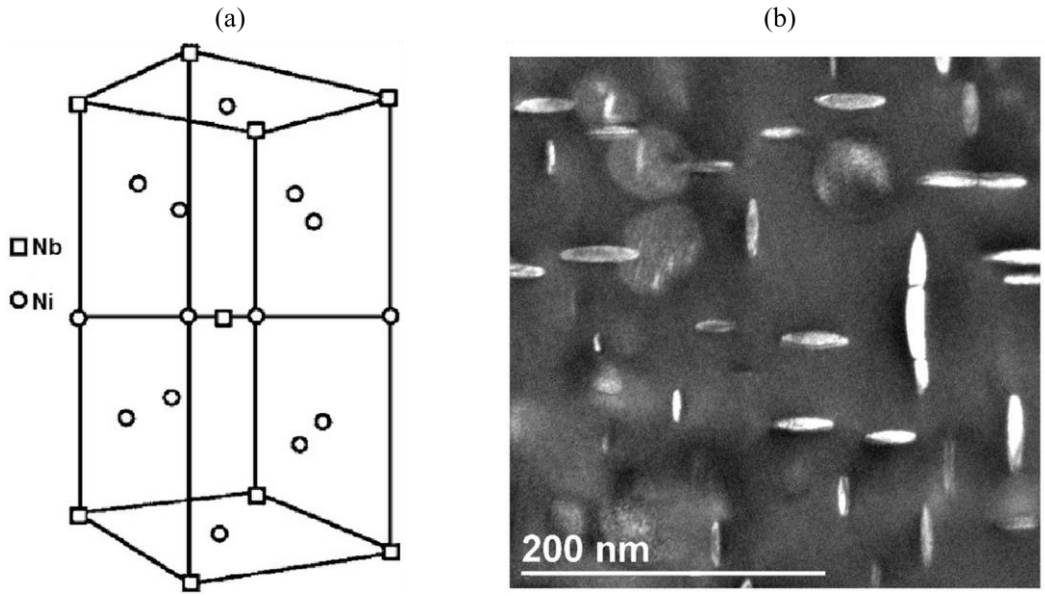

Figure 2.2 (a) BCT $D0_{22}$ unit cell of γ'' (Ni_3Nb), adapted from [77] (b) [001]-orientated darkfield TEM images of γ'' precipitates in aged Inconel 625 showing all three variants of the γ'' phase, adapted from [78].

2.2.3 Delta (δ) phase

The δ phase is the stable counterpart of the γ'' phase, both of which are of the stochastic Ni_3Nb composition. It exhibits a $D0_a$ orthorhombic structure and has an orientation relationship with the γ matrix of the form $(010)_\delta//\{111\}_\gamma$ and $[100]_\delta//<110>_\gamma$ [79, 80]. Therefore, twelve orientational variants of the phase are possible [80]. At relatively lower temperature the precipitation of δ phase is usually preceded by γ''. When aging is performed at temperature lower that the γ'' solvus, the δ phase has been observed to nucleate at grain boundary, twin boundary, and on stacking faults lying on the close packed planes within γ'' precipitates [79, 81]. However, at higher temperature, δ phase can precipitate directly form the supersaturated γ matrix. The δ precipitates exhibit a plate shaped morphology in most cases (Figure 2.3), but globular particles have also been reported [79].

Since the δ phase is incoherent with the γ matrix, and its growth results in the dissolution of the strengthening γ'' phase, it is not usually utilized for precipitation strengthening in Ni-based superalloys. It should also be mentioned that the working temperatures of γ'' strengthen superalloys are typically below 650℃ to prevent the coarsening and transformation of γ'' to δ phase, since this change can lead to deterioration in mechanical properties such as strength and fracture toughness. [82, 63]. However, the controlled precipitation of δ phase at grain can be used for grain refinement in polycrystalline superalloys [83, 84], where the small grain microstructures is desirable for increased strength and toughness due to the Hall-Petch effect [85, 86]. Furthermore, intergranular δ phase can be used to stabilize grain boundaries via Zener pinning and improve the high temperature rapture properties of some Ni-base superalloys [87, 88].

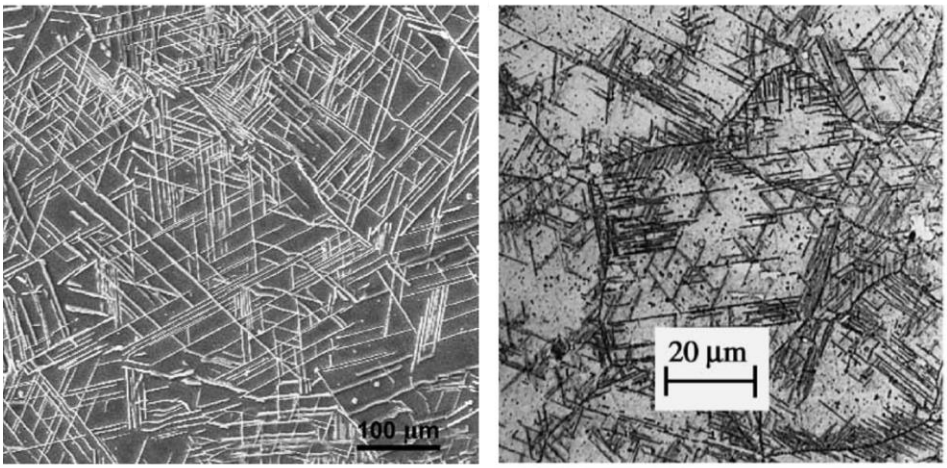

Figure 2.3 δ phase observed in aged (a) IN 718 [88] (b) IN 625 [89]

2.2.4 Eta (η) phase

The η phase exhibits a hexagonal close-packed, $D0_{24}$ structure with a Ni_3Ti composition. They are observed as large platelets (Figure 2.4) having an orientation relationship with the γ matrix of the form $<011>_{\gamma}//<2110>_{\eta}$ and $\{111\}_{\gamma}//\{0001\}_{\eta}$ [90]. The formation of η phase is usually observed in alloys with higher Ti, Ta, Nb, and Hf compared to Al composition, and have been reported to destabilize the strengthening γ' phase [91]. They are observed to form during casting due to local segregation of the elements [91], during prolonged thermal exposure and heat treatment [90, 92]. The η phase does not contribute to the strengthening of Ni-based superalloys because of its low coherency with the γ matrix [91]. Large amounts of η phase can reduce the strength and ductility of the material due to the reduction of the γ' phase and solid solution strengthening elements in the γ matrix. In smaller amounts, η phase can be utilized for grain stability and refinement [63].

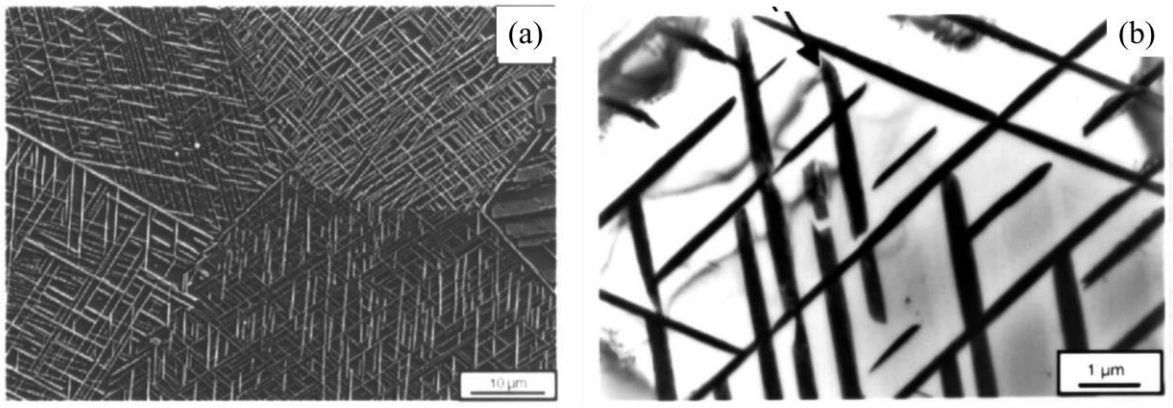

Figure 2.4 η phase observed in aged IN 706 [90] (a) distribution of η phase in different grains (b) high magnification showing η phase distribution in a single grain.

2.2.5 Topologically close packed (TCP) phases

The use of refractory elements for solid solution strengthening and to enhance the stability of the γ and γ' phases can leave the Ni-based superalloy vulnerable to the precipitation of the deleterious topologically closed pack (TCP) phases, whenever the alloy is exposed to high temperature or stress. TCP phases often develop in Ni-based alloys with a high concentration of refractory elements such as Re, W, Cr, MO, and Ta, and they have a high-density complex crystal structure [93, 94]. TCP phases usually have a "basket weave" morphology, which is made up of ribbons of precipitates that overlap at 90-degree angles (Figure 2.5a) [93]. In general, three TCP phases are observed in Ni-based superalloys, depending on the size ratio of the component atoms: σ phase (tetragonal), P phase (orthorhombic), and μ phase (rhombohedral) (Figure 2.5b) [93, 94].

Excessive precipitation of TCP phases in Ni-base superalloys has frequently been observed to result in significant degradation in mechanical properties such as ductility, fatigue resistance, and stress rupture life [61]. This is because, precipitation of TCP phases decreases the solid solution strengthening effect due to the depletion of Re, W and Cr in the matrix [61]. Secondly, since TCP phases are brittle compared to the matrix, they can delaminate in the fracture zone [95]. Thirdly, the formation of TCP phases at high temperatures is typically accompanied with the production of voids, which may function as fracture initiation sites [96, 97]. Therefore, during the alloy design process, prudent selection of the types and amounts of alloying elements is needed to obtain the beneficial effect of the elements (e.g., solid solution strengthening and phase stabilization) while minimizing the formation of TCP phases.

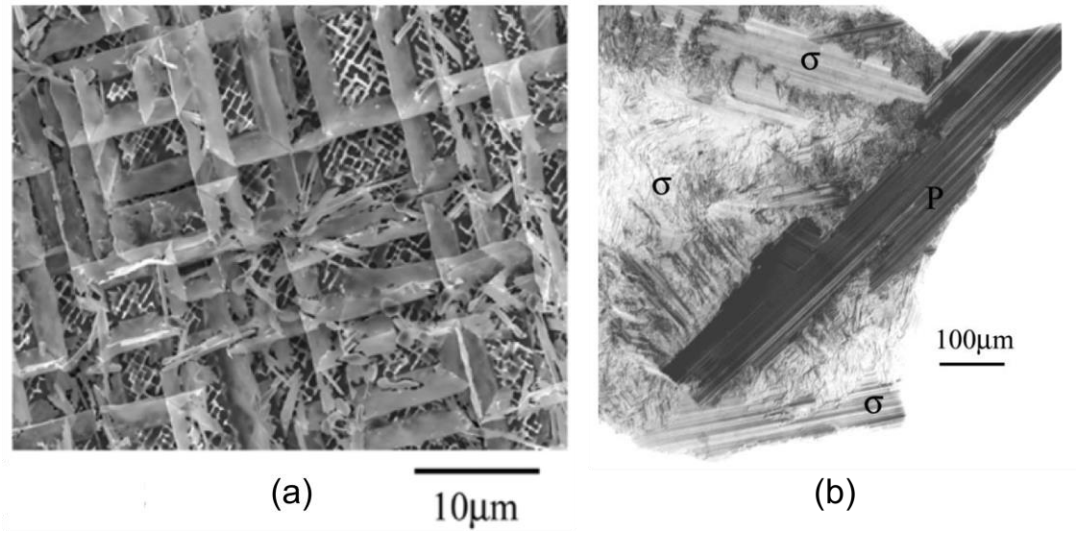

Figure 2.5 TCP precipitates in aged nickel-base superalloy. (a) "Basket weave" microstructure due to TCP formation. (b) Micrograph highlighting σ and P TCP phases.

2.2.6 Carbides

In superalloys, many carbide species occur, the type is dependent on the alloy composition and the processing conditions. Some of the more common forms include MC, M_6C, $M_{23}C_6$, and M_7C_3, where M represents a metal atom such as Cr, Mo, Ti, Ta, or Hf [57]. Carbide can precipitate during solidification, long term thermal exposure, or heat treatment [57, 98, 99]. For example, MC carbides have been observed to precipitate in the interdendritic regions at high temperatures during solidification [98]. As a result, there is no distinct orientation relationship between the carbide and the γ matrix. Some carbides, such as $M_{23}C_6$, develop at lower temperatures (about 750℃) during prolonged service exposure, particularly in Cr-rich alloys [57]. Carbides can have a range of morphologies (Figure 2.6), including globular, blocky, and script morphologies [98]. Carbides can be employed as grain boundary strengtheners. Carbides located at grain boundaries have been reported to improve the creep properties and rupture strength via the inhibition of grain-boundary

sliding [100, 101, 102]. Therefore, carbides are preferred in polycrystalline Ni-based superalloys compared to single-crystal alloys where grain-boundary strengthening is not needed.

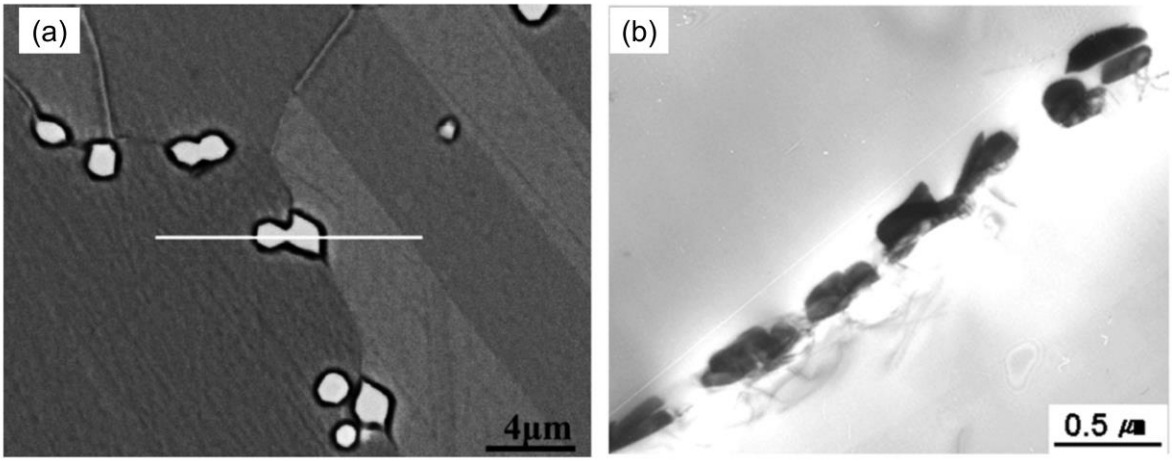

Figure 2.6 (a) Intergranular M_6C carbides in a Hastelloy N type alloy [103] (b) Discontinuous $M_{23}C_6$ particles in Alloy 690 [104]

CHAPTER III

PHASE-FIELD SIMULATION OF GAMMA DOUBLE PRIME PRECIPITATION IN INCONEL 625

3.1 Introduction

Inconel 625 is widely used in the aerospace, chemical processing, power, and marine industries, due to its high strength, outstanding fatigue, corrosion, and oxidation resistance, and excellent fabricability and weldability [105]. Inconel 625 was originally designed as a solid-solution strengthened alloy but was found to be highly susceptible to precipitation hardening by the formation of the body-centered tetragonal (BCT) γ'' phase ($D0_{22}$-Ni_3Nb) after thermal aging between 550–750 ℃ [105, 106, 107]. Aging controls the size distribution, volume fraction, and morphology of the γ''precipitates, which in turn determines the mechanical properties of the alloy. Therefore, understanding the morphological evolution of γ''during aging is critical for evaluating their hardening effects and improving the mechanical properties of the alloy.

Numerical investigation of the process-structure-property relationship in materials is becoming increasingly attractive because of the time and cost saving it can potentially offer [108, 109]. This is especially true for Inconel 625 that requires hundreds or even thousands of hours of aging time to achieve a significant precipitation-hardening effect [107, 110, 111]. Therefore, theoretical analysis or computer simulation is a promising complement to trial-and-error-based experiments in optimizing the heat treatment strategy. Using the Svoboda-Fischer-Fratzl-Kozeschnik (SFFK) and subsequently, Lifshitz-Slyozov-Encounter-Modified (LSEM)

frameworks, Moore *et al*. [78, 112] were able to capture *γ"* evolution trends during heat treatment. The major drawback of these frameworks is that since *γ"* exhibits a plate-shaped morphology, the model parameters have to be calibrated to experimentally measured aspect ratio data at all temperatures and times of interest, which is a laborious undertaking.

The physics-based phase-field method [29], which introduces the diffuse-interface concept to avoid the explicit tracking of interfaces, stands out with the significant potential to accurately predict precipitate morphology, growth, and coarsening kinetics in various alloy systems. Notable examples of its application include: *γ'* and *γ"* precipitates in Ni-alloys [113, 74, 44, 47], *β'* and β_1 precipitates in Mg-rare earth alloys [114, 115, 116] , *θ'* precipitates in Al-Cu-based alloys [117, 118, 119], and *α* precipitates in Ti-alloys [120]. The phase-field model offers two main advantages for simulating the morphological evolution of *γ"* over the SFFK and LSEM models. Firstly, because the lattice misfit strain between the precipitate (*γ"*) and the matrix (*γ*) serves as input for the phase-field model, the model can accurately predict *γ"* aspect ratio evolution. Therefore, eliminating the need to calibrate to experimentally observed aspect ratio evolution data. Secondly, since the phase-field model captures the growth of particles under elastic stresses [121] and compositional strains [122], the "directional encounter" phenomenon observed in *γ"* precipitates [112] is naturally captured by the model. The phase-field method has been used to study *γ"* precipitation kinetics in nickel-based superalloys. For example, Zhou *et al*. [113] studied *γ'*, *γ"*, and *δ* precipitation in Inconel 718. Shi *et al*. [123] investigated the growth behavior of *γ'/γ"* coprecipitates in nickel-base superalloys. Ji *et al*. [74] studied the coherency loss of *γ"* in Inconel 718. However, these existing investigations either exclusively focused on the growth behavior of particles without careful consideration of nucleation kinetics or lacked comprehensive experimental validations in terms of *γ"* mean size, volume fraction, and morphology evolution, all

of which are necessary prerequisites for a reliable and predictive computational model of *γ''* precipitate kinetics and the resultant strengthening effects.

The aim of this study is to develop a phase-field model for predicting the precipitation kinetics and morphology evolution of *γ''* precipitates in Inconel 625 during isothermal and non-isothermal aging conditions. To obtain more quantitative simulation results, we incorporate nucleation and more accurate diffusion-controlled kinetics to the phase-field model developed by Zhou *et al*. [113]. All input parameters are taken from validated experimental measurements, theoretical calculations, or calibration to experimental results. The implemented explicit nucleation method based on the classical nucleation theory enable us to capture the spatial distribution of nuclei as a function of local supersaturation. The simulation results for mean particle size, aspect-ratio, and volume fraction evolution are in agreement with the experimental data for simulations at 600 ℃ and 650 ℃ during isothermal aging. Utilizing the results from the phase-field simulations as input parameters to a macroscale coherency strengthening model, the coherency strengthening effect of *γ''* as a function of aging temperature and time is predicted. Finally, a multistage aging strategy to optimize hardening effects and reduce aging time by utilizing the developed phase-field model and coherency strengthening model is discussed.

3.2 Methodology

Inconel 625 is a multi-component alloy with about twelve or more components. The typical alloying elements in Inconel 625 and their compositions are shown Table 3.1. The main phases occurring in Inconel 625 during thermal aging are *γ''*, *δ,* Laves, MC, M_6C, and $M_{23}C_6$ carbides as shown in the Time-Temperature-Transformation (TTT) diagram in Figure 3.1. Inconel 625 does not precipitate the $L1_2$-ordered *γ'* phase found in most Nickel-base superalloys (e.g. Inconel 718) because of its low aluminum and titanium contents. Only the strengthening *γ''* phase is considered

in this work because of the ageing time, temperatures and the focus on intragranular precipitation in this study.

To save computational efforts while capturing the essential features of the precipitation process, we used a pseudo-ternary (Ni-Al_x-Nb_y) CALPHAD thermodynamic database developed for Ni-based superalloys [124]. This database considers Al_x as a weighted summation of all γ'-forming elements (Al and Ti) and Nb_y as weighted summation of all γ''- and δ-forming elements (Nb and Ta), which will be represented by Al^* and Nb^*, respectively. The system is represented with two composition fields, X_{Al^*} and X_{Nb^*}. As γ'' is a tetragonal phase embedded in the cubic γ matrix and exhibits an orientation relationship of $\{100\}_{\gamma''}//\{100\}_{\gamma}$ and $[001]_{\gamma''}//<100>_{\gamma}$, three orientation variants with different {100} habit planes will appear. Therefore, all three orientation variants of γ'' were considered in the 3D phase-field simulations, with two antiphase domains introduced for each γ'' variant. The existence of the antiphase domains will reduce the frequency of coalescence events between the same variant during the growth and coarsening stages. Therefore, γ'' is represented by three order parameters, $\{\eta_1, \eta_2, \eta_3\}$ to represent the three variants {±1,0,0},{0,±1,0},{0,0,±1}, where the two antiphase domains of the same variant are represented by +1 and -1, respectively (Figure 3.2). With this definition, $|\eta_p| = 0$ corresponds to the matrix phase and $0 < |\eta_p| < 1$ corresponds to the γ/γ'' interface. In order to simulate both isothermal and non-isothermal aging conditions, the temperature dependent total free energy functional for the single crystal system can then be expressed as:

$$F = \int_V \left[f_{bulk}\left(X_{Al^*}, X_{Nb^*}, \eta_p, T\right) + f_{grad}\left(\nabla \eta_p\right) + e_{el} \right] dV \tag{3.1}$$

where f_{bulk} is the bulk free energy density of the system, f_{grad} is the gradient energy due to inhomogeneous distribution of the order parameters, and e_{el} is the elastic strain energy density.

Table 3.1 Composition (at.%) of Inconel 625 [112].

Ni	Cr	Fe	Mo	Nb	C	Mn	Si	P	S	Al	Ti
63.05	24.85	3.05	5.32	2.43	0.10	0.22	0.49	0.02	0.01	0.26	0.20

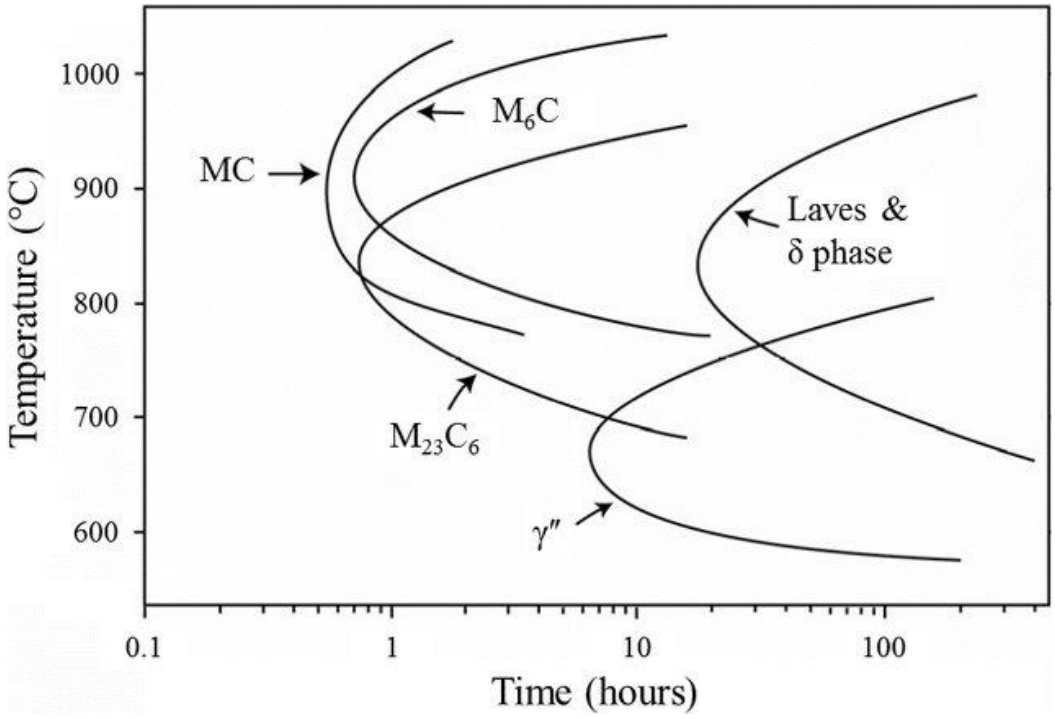

Figure 3.1 Time-Temperature-Transformation (TTT) diagram for Inconel 625. Adapted from Floreen *et al*. [106].

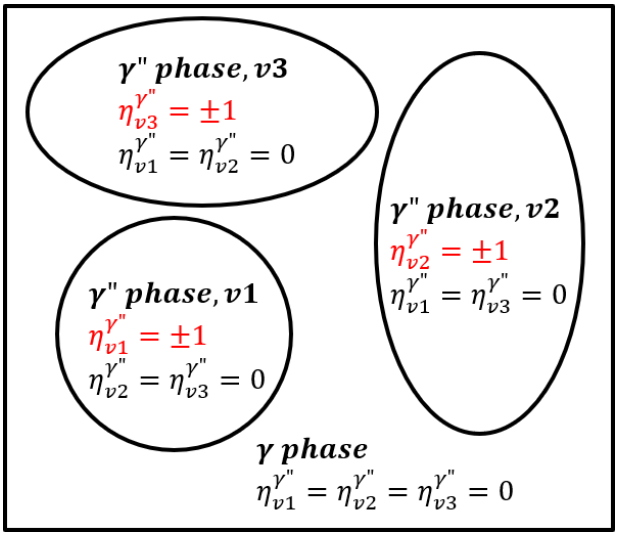

Figure 3.2 Schematic representation of different γ'' variants and antiphase domains in Inconel 625 using a set of three structural order parameters in the phase-field method.

3.2.2 Bulk free energy

The bulk free energy of the system is the sum of the Gibbs free energy of different phases and the energy variation due to structural change and is expressed as the following,

$$f_{bulk}\left(X_{Al^*}, X_{Nb^*}, \{\eta_p\}, T\right) = V_m^{-1} \cdot \left[1 - \sum_{p=1}^{3} h(\eta_p)\right] \cdot f^{\gamma}\left(X_{Al^*}^{\gamma}, X_{Nb^*}^{\gamma}, T\right) + V_m^{-1} \cdot \sum_{p=1}^{3} h(\eta_p) \cdot f^{\gamma''}\left(X_{Al^*}^{\gamma''}, X_{Nb^*}^{\gamma''}, T\right) + g(\{\eta_p\}) \quad (3.2)$$

where $f^{\gamma}\left(X_{Al^*}^{\gamma}, X_{Nb^*}^{\gamma}, T\right)$ and $f^{\gamma''}\left(X_{Al^*}^{\gamma''}, X_{Nb^*}^{\gamma''}, T\right)$ are the molar Gibbs free energy of γ and γ'' phases, obtained from the pseudo-ternary thermodynamic database [124]. V_m is the molar volume, $h(\eta_p)$ is an interpolation function, and $g(\{\eta_p\})$ is the sum of a triple well and interaction energy functions. The expressions for $h(\eta_p)$ and $g(\{\eta_p\})$ are given by the following,

$$h(\eta_p) = 2\eta_p^2 - \eta_p^4 \tag{3.3}$$

$$g(\{\eta_p\}) = w^{\gamma''} \cdot \sum_{p=1}^{3} \eta_p^2 (1 - |\eta_p|)^2 + \alpha \cdot \sum_{p=1}^{3} \sum_{p \neq q}^{3} \eta_p^2 \eta_q^2 \tag{3.4}$$

where $w^{\gamma''}$ defines the free energy hump between the matrix and the precipitate phase. The second term in Eq. (3.4) describes the free energy penalty that prevents different *γ''* variants from occupying the same spatial position and α is a constant parameter which determines the magnitude of the penalty. It is worth noting that the triple well function (first term in Eq. (3.4)) leads to wetting of matrix phase at antiphase boundaries. To incorporate the physical antiphase domains, additional order parameters can be defined and evolved for each type of antiphase domains [125]. However, since the total volume fraction of *γ''* in the present study is quite small (<7%), the current treatment of antiphase boundaries will not lead to significant changes compared to simulations with or without considering the physical antiphase domains. This is because, the small volume fraction would not lead to significant particle coalescence where antiphase domains may play more important roles in precipitation kinetics.

The Kim-Kim-Suzuki (KKS) model [49] is employed to remove the extra double-well potential of composition due to the equal composition assumption at interfaces [50, 51]. It assumes local equilibrium with equal diffusion chemical potential, rather than equal composition, at interfaces. This requires the solution of concentration fields in each phase from the following equations,

$$X_i = X_i^{\gamma} \cdot \left[1 - \sum_{p=1}^{3} h(\eta_p)\right] + X_i^{\gamma"} \cdot \sum_{p=1}^{3} h(\eta_p), \qquad i = Al^*, Nb^* \tag{3.5}$$

$$\frac{\partial f^{\gamma}}{\partial X_i^{\gamma}} = \frac{\partial f^{\gamma"}}{\partial X_i^{\gamma"}}, \qquad i = Al^*, Nb^* \tag{3.6}$$

The non-linear molar Gibbs free energies of f^{γ} and $f^{\gamma"}$ were approximated by Taylor series expansions at equilibrium compositions up to 2nd order as:

$$\begin{aligned} f_{para}^{\theta}\left(X_{Al^*}^{\theta}, X_{Nb^*}^{\theta}, T\right) = A^{\theta} + B_{Al^*}^{\theta}\left(X_{Al^*}^{\theta} - X_{Al^*}^{\theta,eq}\right) + B_{Nb^*}^{\theta}\left(X_{Nb^*}^{\theta} - X_{Nb^*}^{\theta,eq}\right) \\ + \frac{1}{2} C_{Al^*,Al^*}^{\theta}\left(X_{Al^*}^{\theta} - X_{Al^*}^{\theta,eq}\right)^2 + C_{Al^*,Nb^*}^{\theta}\left(X_{Al^*}^{\theta} - X_{Al^*}^{\theta,eq}\right)\left(X_{Nb^*}^{\theta} - X_{Nb^*}^{\theta,eq}\right) \\ + \frac{1}{2} C_{Nb^*,Nb^*}^{\theta}\left(X_{Nb^*}^{\theta} - X_{Nb^*}^{\theta,eq}\right)^2, \qquad \theta = \gamma, \gamma" \end{aligned} \tag{3.7}$$

where $f_{para}^{\theta}\left(X_{Al^*}^{\theta}, X_{Nb^*}^{\theta}, T\right)$ is the parabolic approximation of $f^{\theta}\left(X_{Al^*}^{\theta}, X_{Nb^*}^{\theta}, T\right)$. The temperature dependent equilibrium compositions of Al^* and Nb^* in phase θ are $X_{Al}^{\theta,eq}$ and $X_{Nb}^{\theta,eq}$, respectively. The constants A^{θ}, $B_{Al^*}^{\theta}$, $B_{Nb^*}^{\theta}$, C_{Al^*,Al^*}^{θ}, C_{Al^*,Nb^*}^{θ}, and C_{Nb^*,Nb^*}^{θ} are temperature dependent Taylor expansion coefficients which are calculated from the Ni-Al_x-Nb_y pseudo-ternary database [124] as follows:

$$A^{\theta} = f^{\theta}\left(X_{Al^*}^{\theta,eq}, X_{Nb^*}^{\theta,eq}, T\right) \tag{3.8}$$

$$B_i^{\theta} = \left.\frac{\partial f^{\theta}}{\partial X_i^{\theta}}\right|_{X_i^{\theta} = X_i^{\theta,eq}}, \qquad i = Al^*, Nb^* \tag{3.9}$$

$$C_{i,j}^{\theta} = \left.\frac{\partial^2 f^{\theta}}{\partial\left(X_i^{\theta}\right)^2}\right|_{X_i^{\theta}=X_i^{\theta,eq}}, \qquad i,j = Al^*, Nb^* \tag{3.10}$$

Therefore, the first derivatives of the free energies with respect to concentrations in Eq. (3.6) are linear functions of the concentrations. Hence, Eqs. (3.5) and (3.6) can be solved analytically through matrix inversions [74].

3.2.3 Gradient energy

The gradient energy describes the energy penalty due to the inhomogeneous distribution of phase-field variables near interfaces expressed as the following,

$$f_{grad} = \sum_{p=1}^{3} \frac{\kappa_p}{2} (\nabla \eta_p)^2 \tag{3.11}$$

where k_p is the gradient energy coefficient which together with the barrier height $w^{\gamma"}$ in Eq. (3.4), can be obtained from the interfacial energy (σ) and interface thickness (2λ) according to the following relationships [49]:

$$\sigma = \frac{\sqrt{\kappa \cdot w}}{3\sqrt{2}} \tag{3.12}$$

$$(2\lambda) = 2.2\sqrt{2} \cdot \sqrt{\frac{\kappa}{w}} \tag{3.13}$$

3.2.4 Elastic strain energy

The elastic strain energy contribution due to lattice misfit between the precipitate and the matrix is evaluated by Khachaturyan's microelasticity theory [33],

$$e_{el} = \frac{1}{2} C_{ijkl}\left(\epsilon_{ij} - \epsilon_{ij}^{0}\right)\left(\epsilon_{kl} - \epsilon_{kl}^{0}\right) \tag{3.14}$$

where C_{ijkl} are elastic constants, ϵ_{ij}^{0} is the stress-free transformation strain tensor between the precipitate (γ'') and the matrix (γ). The total strain ϵ_{ij} is calculated from the stress equilibrium equation at each simulation time step. We assume a homogeneous elastic modulus [126] (*i.e.,* the precipitate and matrix phases are assumed to have the same elastic constants) and that stress equilibrium is reached much faster than the diffusional phase transformation.

3.2.5 Nucleation

Nucleation is incorporated into the phase-field model using the method described by Simmons *et al*. [52, 53]. The probability for nucleation at a simulation cell is defined by the following,

$$P = 1 - exp(-J \cdot \Delta t) \tag{3.15}$$

where Δt is the time step and J is the nucleation rate, which, following the classical nucleation theory of Johnson-Mehl-Avrami-Kolmogorov [127, 128, 129], is expressed as the following,

$$J = Z\beta^{*}N_{0}exp\left(\frac{-\Delta G^{*}}{k_{B}T}\right)exp\left(\frac{-\tau}{t}\right) \tag{3.16}$$

here Z is Zeldovich's factor, β^* is atomic attachment rate, N_0 is the number of available nucleation sites in the system, ΔG^* is the nucleation barrier, k_B is Boltzmann's constant, T is temperature, τ is the incubation time for nucleation, and t is elapsed time. These quantities can be calculated from the expressions given in Table 3.2.

At the beginning of the simulations when no precipitate has nucleated in the simulation volume, all grid points are possible nucleation sites. Therefore, the nucleation probability is computed at all grid points. As precipitates nucleate and grow, the grid points occupied by the precipitates (i.e., $|\eta_p| > 0.5$) are excluded from the possible nucleation cites. Therefore, the nucleation probability is only computed for grid points that are not occupied by precipitates (i.e., $|\eta_p| < 0.5$). During nucleation, the nuclei are assumed to be spherical and γ'' variants are randomly selected. The composition of the critical nuclei at a given temperature is set to the equilibrium composition $\left(X_{Nb^*}^{\gamma'',eq}, X_{Al^*}^{\gamma'',eq}\right)$ calculated from the thermodynamic database [124]. Since γ'' is rich in Nb^*, the composition of Nb^* was radially reduced in the matrix phase around the nucleus $\left(|\eta_p| < 0.1\right)$ by exactly the amount required to give the additional solute necessary for the γ'' nucleus. The concentration of Nb^* in the depleted region is set to the equilibrium of Nb^* in the matrix ($X_{Nb^*}^{\gamma,eq}$). Conversely, since γ'' is Al^* poor, the composition of Al^* in the matrix is enriched up to the equilibrium concentration ($X_{Al^*}^{\gamma,eq}$) to accommodate for the reduction of Al^* in the γ'' nucleus. The critical radii of γ'' nuclei were at least three grid points ($3l_0$) to ensure that the nucleating particles are stable. Note that the described seeding method does not satisfy diffusion at the instance of particle nucleation because the initial depleted/enriched layer around the nucleus are sharp. Subsequent simulation time steps will diffuse these boundaries to satisfy Eq. (3.17). Although a nucleation algorithm that naturally satisfies diffusion is available [54], the hold time

required to obtain a stable nucleus is too lengthy because of the slow growth kinetics of γ'' investigated in this study which would increase the computational effort needed to introduce each nucleus.

Table 3.2 Expressions for parameters in the nucleation model (Eq. (3.16)) [130].

Parameters	**Description**	**Expression**
$Z[dim.less]$	Zeldovich factor	$\frac{a^3 \Delta G_c^2}{8\pi\sqrt{\kappa_B T \sigma^3}}$
$\beta^*[s^{-1}]$	Atomic attachment rate	$\frac{4\pi r_c^2}{a^4}\left[\sum_{i=1}^{n}\frac{(X_{ki}-X_{0i})^2}{X_{0i}D_{0i}}\right]^{-1}$
$r_c[m]$	Critical radius	$-\frac{2\sigma}{\Delta G_c}$
$\Delta G^*[J]$	Critical nucleation energy	$\frac{16\pi}{3}\frac{\sigma^3}{\Delta G_c^2}$
$\Delta G_c[J\cdot m^{-3}]$	Nucleation driving force	$\frac{1}{V_m}\sum_{i=1}^{n} X_{ki}(\mu_{ki}-\mu_{0i})$
$\tau[s]$	Incubation time	$\tau = \frac{1}{2\beta^* Z^2}$

where a is matrix atomic distance; k_B is Boltzmann's constant; T is temperature; X_{ki}/X_{0i} is the element compositions in precipitate/matrix; D_{0i} is diffusivities in matrix; and σ is interfacial energy.

3.2.6 Kinetic equations

The diffusion and Allen-Cahn [32] equations are solved to obtain the spatial and temporal evolution of the concentration fields and order parameters, respectively,

$$\frac{\partial X_i}{\partial t} = \nabla\cdot\left(M_i \nabla \frac{\partial f^{\gamma}}{\partial X_i^{\gamma}}\right), \qquad i = Al^*, Nb^* \tag{3.17}$$

$$\frac{\partial \eta_p}{\partial t} = -L\left(\frac{\partial f_{bulk}}{\partial \eta_p} - \kappa_p \nabla^2 \eta_p + \frac{\partial e_{el}}{\partial \eta_p}\right) \tag{3.18}$$

where M_i $(i = Al^*, Nb^*)$ are the chemical mobilities of Al^* and Nb^*, respectively. The mobilities can be estimated as $M_i = \frac{D_i}{V_m \frac{\partial^2 f^\gamma}{\partial X_i^2}}$, where $D_i = D_0 exp\left(\frac{-Q_d}{RT}\right)$ $(i = Al^*, Nb^*)$ are the temperature dependent diffusivities of Al^* and Nb^*. L is the kinetic coefficient for structural evolution. The value of L is selected to ensure diffusion-controlled growth of the precipitates. These governing equations are normalized by the simulation grid size l_0 and a reference energy E_0 and were solved numerically using the spectral method proposed by Chen and Shen [131]. The spectral method offers the advantage of accurate simulation results with fewer interfacial grid points compared to discrete methods like the finite difference [131]. The grid size, $l_0 = 0.75\ nm$ and discretization time step size, $\Delta t^* = 0.01$ were used for all simulations. Real time step can be calculated as:

$$\Delta t = \frac{(l_0)^2 \cdot \Delta t^*}{D_{Nb^*}} \tag{3.19}$$

To provide a sense of the computational times in this work, isothermal aging simulations at 600°C were iterated for 690000 time-steps and took approximately 48 hours. Isothermal aging at 650°C and all multistage aging simulations were iterated for 1530000 time-steps, and each took 96 hours. All simulations were performed on 20 Intel Xeon CPUs E5-2680 at 2.80GHz with OpenMP parallel Fortran Codes.

3.2.7 Parameterization

This section aims to explain the procedure for model parameter selection. Ideally, little to no calibration of model parameters are needed, since all the parameters in the phase-field model described in Section 3.2 have physical meaning, and can be obtained from thermodynamic, lower length scale calculations, or experimental measurements. However, given the sensitivity of the simulation results to the interfacial energy, diffusivity, misfit strain, and the scarcity of data for the aforementioned parameters for Inconel 625 in the literature, we conducted preliminary phase-field simulations to identify parameters that best fit the experimental mean particle size and aspect ratio evolution.

To calculate the elastic energy of the system, the elastic constants and misfit strains are needed. The temperature dependent elastic constants data for Inconel 625 was taken from Wang *et al*. [132] and a linear fit is employed as shown in Figure 3.3. Therefore, only the misfit strains are left to be determined for the elastic energy description. Varying misfit strains have been reported for various γ'' precipitating nickel-based super alloys [133, 134, 72, 73, 135]. The investigation by Schleifer *et al*. [126] reported that for $\epsilon_{33}^0/\epsilon_{11}^0 \geq 3$, ϵ_{33}^0 dictates the plateau aspect ratio. Phase-field aging simulations at 650℃ identified $\epsilon_{11}^0 = \epsilon_{22}^0 = 0.0094$ and $\epsilon_{33}^0 = 0.0372$ [73] to provide close fit to experimental length and aspect ratio time evolution data at the same temperature. Since temperature dependent misfit strain for Inconel 625 is lacking in the literature, these values were used for all temperature investigated in this study.

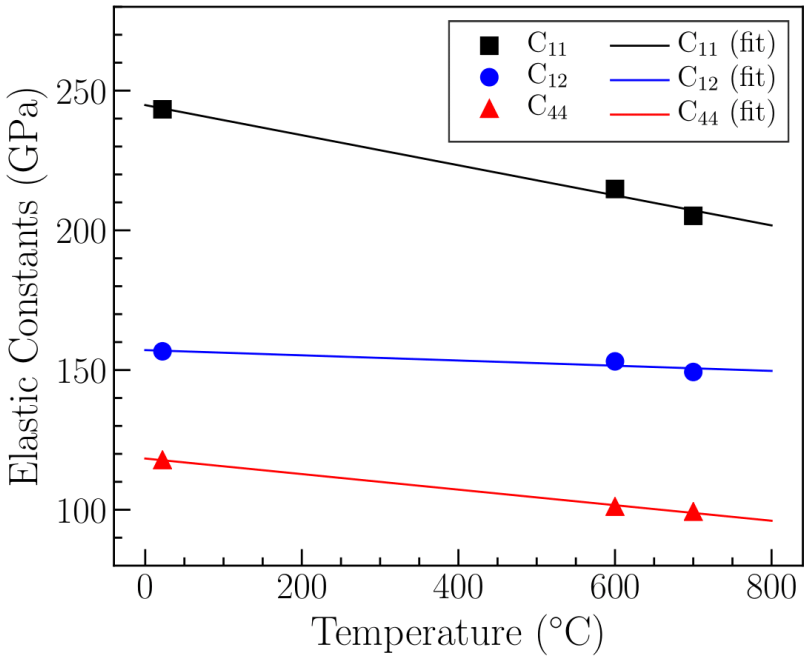

Figure 3.3 Elastic constants for γ phase in Inconel 625. Experimental data are sourced from Wang *et al.* [132] and a linear fit is employed to describe the temperature dependency of the elastic constants.

Values for the diffusion prefactor (D_0) and activation energy (Q) are needed to calculate the temperature dependent diffusivity of Al* and Nb*. Devaux *et al.* [72] reported that the growth of γ'' in Inconel 718 (a related derivative alloy) was controlled by volume diffusion of niobium in the matrix. Therefore, $Q_{Nb^*} = 295\ \mathrm{kJmol^{-1}}$ was calibrated to fit the phase-field results for isothermal aging at 650°C to the linear region of the experimental γ'' length time evolution data since real time is calculated with Eq. (3.19) which requires D_{Nb^*} as input. The linear region of γ'' length time evolution curve represents the free diffusional growth of γ'' particles, with negligible elastic interaction or competition for solute between particles. Although it was observed that the diffusion of Al* had negligible effect on the growth kinetics of γ'', spurious negative concentration

was observed in the γ'' phase during aging simulations at 650℃. Therefore, $Q_{Al^*} = 325$ kJmol^{-1} was chosen to avoid this. $D_0 = 8.8 \times 10^{-5}\ m^2/s$ [72] for both Al* and Nb*.

The interfacial energy is calibrated to obtain the maximum γ'' number density that would allow best fit of phase-field results to experimental γ'' morphological evolution data. The spatial nucleation probability (Eq. (3.15)) is extremely sensitive to the interfacial energy values because of the exponential terms in Eqs. (3.15) and (3.16). Therefore, the interfacial energy was carefully calibrated for isothermal aging at 600℃ ($\sigma = 172.88\ mJ/m^2$) and 650℃ ($\sigma = 151.56\ mJ/m^2$). See Figure 3.4 for the effect of the interfacial energy on γ'' number density and morphological features. The interfacial energy affects the nucleation barrier and therefore, the nucleation rate, nucleation probability, and maximum number density. A large interfacial energy value would lead to a slower nucleation rate, lower γ'' number density and slower growth kinetics. However, the mean length of the precipitates would be larger since there are fewer γ'' particles to compete for solute. Figure 3.4 shows the effect of interfacial energy on the nucleation kinetics and morphological features of γ'' for phase-field simulations at 650℃ aging temperature. From the figure, $\sigma = 151.56\ mJ/m^2$ was chosen for the simulation studies at 650℃ aging temperature in the main text of the manuscript. For $\sigma = 150.10\ mJ/m^2$, the nucleation is much easier, resulting in a maximum number density of 2.37×10^{22} m^{-3}, a reduced mean length, and faster saturation of the precipitate volume fraction. For $\sigma = 151.5756\ mJ/m^2$, the high nucleation barrier impedes the nucleation, resulting in maximum number density of 5.65×10^{21} m^{-3}, higher mean precipitate length, and a slower saturation of the precipitate volume fraction. The reduction in number density for $\sigma = 150.10\ mJ/m^2$ and $\sigma = 151.56\ mJ/m^2$ in Figure 3.4d is due to the coalescence of γ'' particles belonging to the same antiphase domain. Although, the shrinkage of smaller particles as a result of Ostwald ripening was observed for all cases, the complete dissolution of the shrinking

particles was not captured in the time interval simulated. A linear fit is utilized for the temperature dependency of the interfacial energy between 600℃ to 760℃ temperature range investigated in this work. Table 3.3 compares the calibrated parameters used in this study to the values reported in the literature by different authors for γ'' in various alloy systems. It is important to note that apart from the composition and temperature dependency of material properties, the misfit strain and interfacial energy of γ'' are also dependent on the aspect ratio [136] and the degree of coherency [74], further adding to the difficulty of accurate characterization of these properties. A comprehensive list of all inputs used for the simulations is provided in Table 3.4.

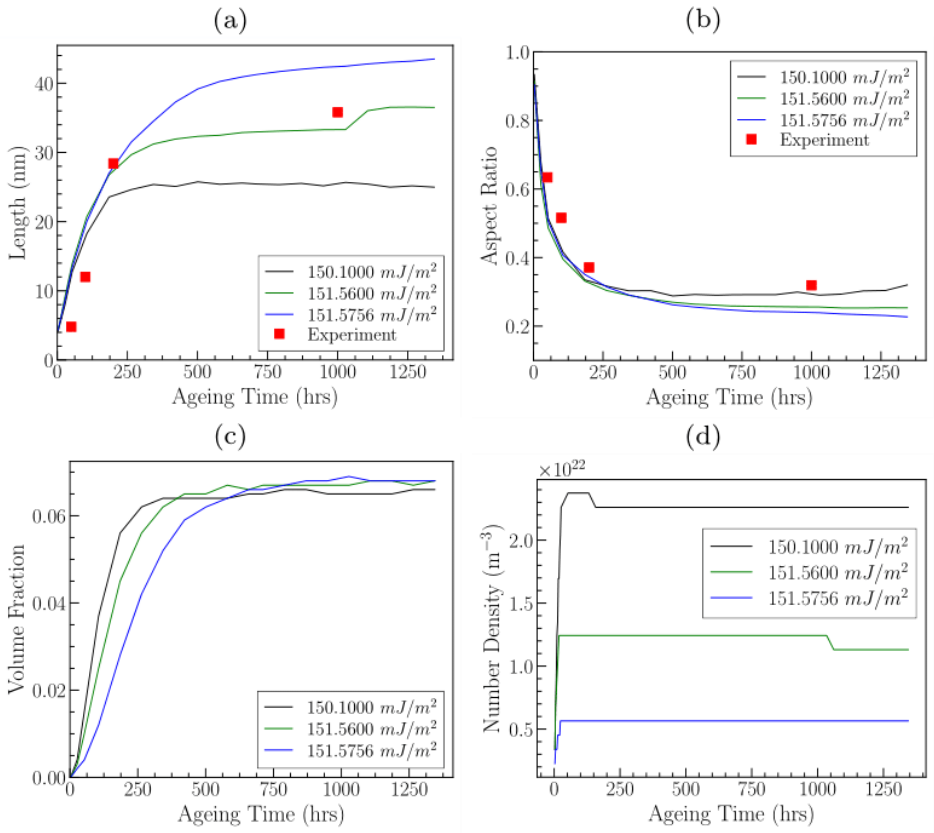

Figure 3.4 Effect of interfacial energy on the Simulated γ'' precipitation kinetics in Inconel 625 aged at 650 ℃ and comparison with experimental measurements [136]. (a) Particle length. (b) Aspect ratio. (c) Volume fraction. (d) Number density.

Table 3.3 Literature values for the interfacial energy and misfit strain of *γ''* precipitates, as well as activation energies for atomic diffusion in nickel-based alloys compared to the values used in this study.

Source	**System**	**Interfacial Energy (mJ/m^2)**	$\epsilon_{11}^0 = \epsilon_{22}^0$ (10^{-2})	ϵ_{33}^0 (10^{-2})	**Activation Energy ($kJ \cdot mol^{-1}$)**
Devaux *et al*. [72]	Inconel 718	95 ± 17	0.67	2.86	272
Cozar *et al*. [73] (25 ℃)	Fe 30.8-Ni 9.1-Ta	145	0.94 ± 0.03	3.72 ± 0.06	–
Cozar *et al*. [73] (750 ℃)	Fe 30.8-Ni 9.1-Ta	185	0.70	3.46	–
This Study	Inconel 625	172.88 at 600 ℃ 151.56 at 650 ℃	0.94	3.72	295

Table 3.4 Parameters for phase-field simulations.

Parameters	Description	Expression
V_m	Molar volume	$1.07 \times 10^{-5}\ m^3/mol$
$X^0_{Al^*}, X^0_{Nb^*}$	Al*, Nb* initial matrix composition	$0.0046, 0.0243$ [112]
D_{0Al^*}, D_{0Nb^*}	Al*, Nb* diffusion prefactor	$8.8 \times 10^{-5}\ m^2/s$ [72]
Q_{Al^*}, Q_{Nb^*}	Al*, Nb* diffusion activation energies	$325\ kJmol^{-1}, 295\ kJmol^{-1}$
σ	Interfacial energy	$(-0.4264T + 428.72)\frac{mJ}{m^2}$ $for\ 600℃ \leq T \leq 760℃$
l_0	Simulation grid size	$0.75\ nm$
E_0	Reference energy density	$2.5\ GPa$
(2λ)	Interface thickness	$2l_0$
L	Kinetic coefficient	$\frac{L^*D}{E_0 l_0^2}$, $L^* = 10$ for all T
C_{11}, C_{12}, C_{44}	Elastic constants	$C_{11} = (-0.05383T + 244.8)\ GPa$ $C_{12} = (-0.009304T + 157.1)\ GPa$ $C_{44} = (-0.02784T + 118.3)\ GPa$ [37]
ϵ^0_{ij}	Misfit strain tensor	$\begin{bmatrix} 0.0094 & 0 & 0 \\ 0 & 0.0094 & 0 \\ 0 & 0 & 0.0372 \end{bmatrix}$ [73]

3.3 Results and discussion

3.3.1 Morphology evolution and precipitation kinetics of γ"

To obtain the morphological features of γ" from the phase-field simulations, the precipitates were identified as regions with $|\eta_p| \geq 0.5$ and all 3D simulation images presented are contour plots of $|\eta_p| = 0.5$. The length of each γ" variant is calculated from the radius of a circle fitted to each precipitate in their respective habit planes, {100}. The thickness is calculated along the distance perpendicular to the habit planes. The aspect ratio is defined as the thickness/length. And the volume fraction was calculated as the fraction of nodes occupied by precipitates in the 3D simulation volume $(|\eta_p| \geq 0.5)$. Figure 3.5 and Figure 3.6 illustrate the simulated γ" precipitate

morphological evolution for isothermal aging at 600 ℃ and 650 ℃. From these figures, it is evident that the time evolution of *γ''* into a disk-shaped morphology are well reconstructed by the phase-field simulations. Since the habit planes of *γ''* are {100} planes, the major axis of the three variants (as indicated by the different colors) are perpendicular to one another. The simulated microstructure and experimental TEM image (Figure 3.7) show that *γ''* precipitates coalesced with each other along their edges except for those in antiphase relationships that align and attach to each other along their edges, leaving antiphase boundaries (APBs) in between. No face-to-face coalescence was observed because of elastic interactions among precipitates.

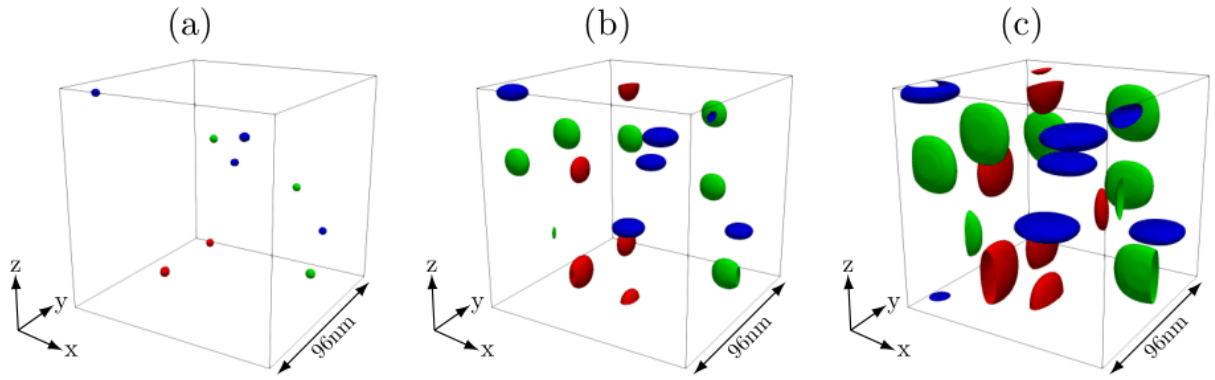

Figure 3.5 Simulated microstructure evolution of *γ''* precipitates in Inconel 625 aged at 600 ℃. The phase-field simulations were performed in a $96 \times 96 \times 96$ nm^3 volume and are shown after aging for (a) 95 hours, (b) 1185 hours, and (c) 5405 hours. The different colors represent different variants of *γ''*. The x-, y-, and z-axis represent [1 0 0], [0 1 0], and [0 0 1] directions, respectively.

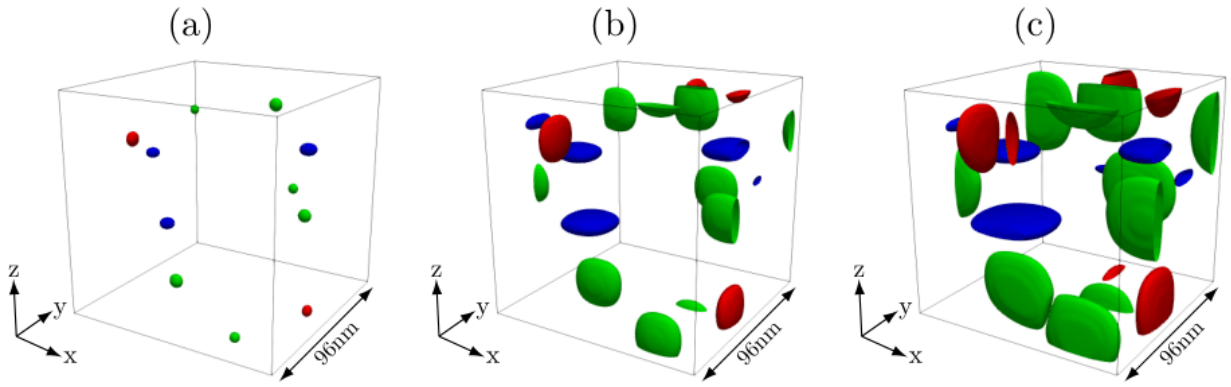

Figure 3.6 Simulated microstructure evolution of γ'' precipitates in Inconel 625 aged at 650 ℃. The phase-field simulations were performed in a $96 \times 96 \times 96$ nm^3 volume and are shown after aging for (a) 10 hours, (b) 105 hours, and (c) 1000 hours. The different colors represent different variants of γ''. The x-, y-, and z-axis represent [1 0 0], [0 1 0], and [0 0 1] directions, respectively.

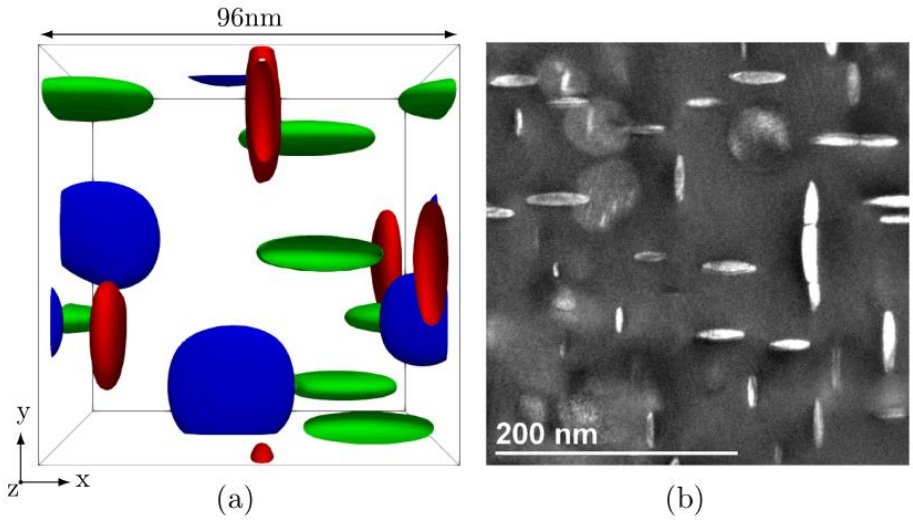

Figure 3.7 Microstructure of γ'' precipitates in Inconel 625 aged at 650 ℃ for 1000 hours. (a) Phase-filed simulation (b) TEM image with a [0 0 1] crystallographic orientation [78]. The different colors represent different variants of γ''. The x-, y-, and z-axis represent [1 0 0], [0 1 0], and [0 0 1] directions, respectively.

Figure 3.8 and Figure 3.9 show the evolution of mean particle length, aspect ratio (thickness/length), and volume fraction calculated from the phase-field simulations. The mean

particle length, aspect ratio, and volume fraction were calculated from the aggregate of all particles from the five simulations with different random seeds. The error bars in the length and aspect ratio indicate the first and third quartiles of the distribution and the error bars in the volume fraction was calculated from the standard deviation between the five simulations. Generally, the simulated precipitate length and aspect ratio agree well with the experimental measurements. Deviations between the phase-field and experimental results occurred mainly in the early aging stages at both temperatures possibly because of the large critical nuclei size imposed on the nucleating particles (see Section 3.3.2 for more details). Note that, although γ'' precipitates were assumed to nucleate as spherical particles, because of the anisotropic misfit strain tensor between γ'' and γ matrix, the growth of the particles along the major axis is faster than the growth along the minor axis. Consequently, the aspect ratio (thickness/length) decreases with aging time at a faster rate during the early growth stages compared to the later growth stages (Figure 3.8b and Figure 3.9b). While the current model utilizing an isotropic interfacial energy and isotropic interface kinetics offers favorable results compared to experimental morphological data, it should be noted that a tetragonal to cubic interface might exhibit strong anisotropic properties [117, 119], which could also be incorporated in the phase-field model to improve the accuracy of the predicted morphological features [119]. To the best of our knowledge, no information about the magnitudes of such anisotropies for the γ/γ'' interface is available in the open literature. Therefore, we assume isotropic interfacial properties.

The volume fraction increases monotonically at the early aging stages for both temperatures (Figure 3.8c and Figure 3.9c). This is due to the free diffusional growth of the nucleated γ'' precipitates in the supersaturated γ matrix. The volume fraction reaches a saturation level as the supersaturation in the matrix decreases and elastic interaction alongside competition for solute

between particles arises. This is more pronounced for aging simulation at 650 ℃ (Figure 3.9c) were the saturation volume fraction is about 6.7%. For aging simulation at 600 ℃, the saturation volume fraction is not reached even after 5480 hours of aging reported here. For comparison, the volume fraction calculated from the thermodynamic database is 10.1% at 650 ℃ [124] which is higher than the result from the phase-field simulation (6.7%). The reason for this deviation can be attributed to the fact that the phase-field model includes the contribution from both the interfacial and misfit strain energies which are not included in the calculation from the thermodynamic database that only considers the bulk free energies of the phases. Besides, the thermodynamic calculations report results as time goes to infinity.

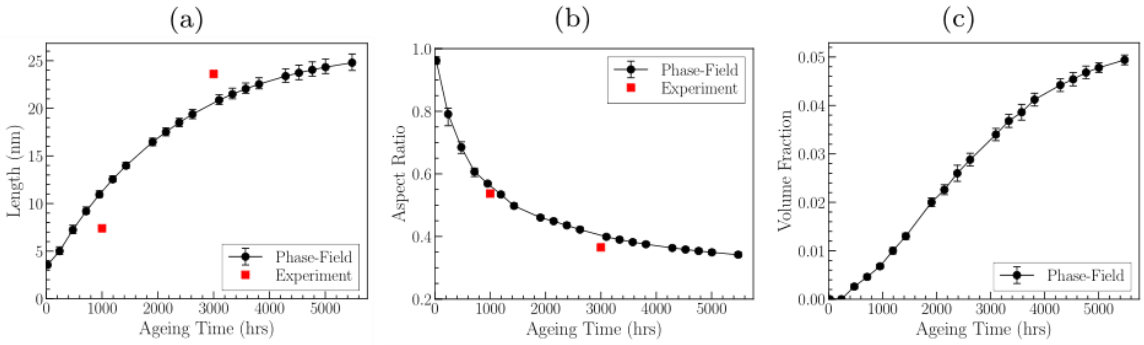

Figure 3.8 Simulated γ'' precipitation kinetics in Inconel 625 aged at 600 ℃ and comparison with experimental measurements [136]. (a) Particle length. (b) Aspect ratio. (c) Volume fraction.

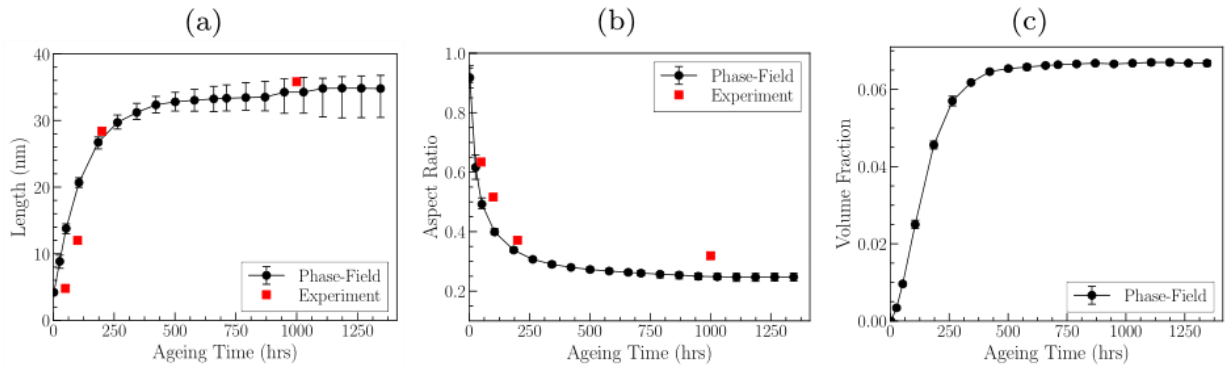

Figure 3.9 Simulated *γ''* precipitation kinetics in Inconel 625 aged at 650 ℃ and comparison with experimental measurements [136]. (a) Particle length. (b) Aspect ratio. (c) Volume fraction.

3.3.2 Nucleation kinetics of *γ''*

The nucleation kinetics controls the number and spatial location of *γ''* nuclei introduced into the simulation volume in each time step according to the probability of nucleation (*P*) calculated form Eq. (3.15). To determine numerically whether a particle nucleate locally or not within each time step, a random number is generated for each untransformed cell and nucleation occurs when the number is smaller than *P*. Figure 3.10 shows the number density evolution for aging at 600 ℃ and 650 ℃ along with contour plot inserts showing the local nucleation probability (*P*) normalized by initial nucleation probability (P_i). As particles nucleate, their growth results in the depletion of Nb^* concentration in the surrounding matrix, resulting in spatially uneven nucleation rates and lower nucleation probability around the particles. From the contour plot inserts in Figure 3.10, the lower probability of nucleation around growing particles due to low local supersaturation can be observed. Also, as the growth of nucleated particles persists, a maximum number density is reached, and nucleation shuts off due to soft impingement. The maximum number density for aging at 600 ℃ (1.67×10^{22} m^{-3}) is greater than that for ageing at 650

℃ (1.27×10^{22} m^{-3}). However, the nucleation rate at 650 ℃ is greater than at 600 ℃ as it takes 19 hours to reach the maximum number density at 650 ℃ compared to 238 hours at 600 ℃. Although, the shrinkage of smaller particles as a result of Ostwald ripening was observed for all cases, the complete dissolution of the shrinking particles was not captured in the time interval simulated for aging at 600 ℃ and 650 ℃. The reduction in number density for aging simulation at 650 ℃ in Figure 3.10b is due to the coalescence of γ'' particles belonging to the same antiphase domain.

One of the challenges with simulating nucleation events in the phase-field method is that the simulation grid size needs to be small enough to resolve the critical nuclei radius (r). This presents a computationally expensive challenge, given that real time is directly proportional to grid size squared (Eq. (3.19)). Using the expressions in Table 3.2, the calculated critical nuclei radii (r) was about 0.6nm for both isothermal aging at 600 ℃ and 650 ℃. Since, the critical radius must be resolved by three grid sizes to ensure that the nucleating particles are stable in the current system, the simulation grid size would have to be about 0.2nm, compared to the 0.75nm used in this study. However, reducing the grid size to 0.2nm would severely affect the real time step of the simulation (Eq. (3.19)). Also, more numerical grid points would be required to simulate the same physical volume. As a result, the computational effort would increase drastically. With this knowledge, we decided against reduction of grid size in order to capture the long aging times of Inconel 625.

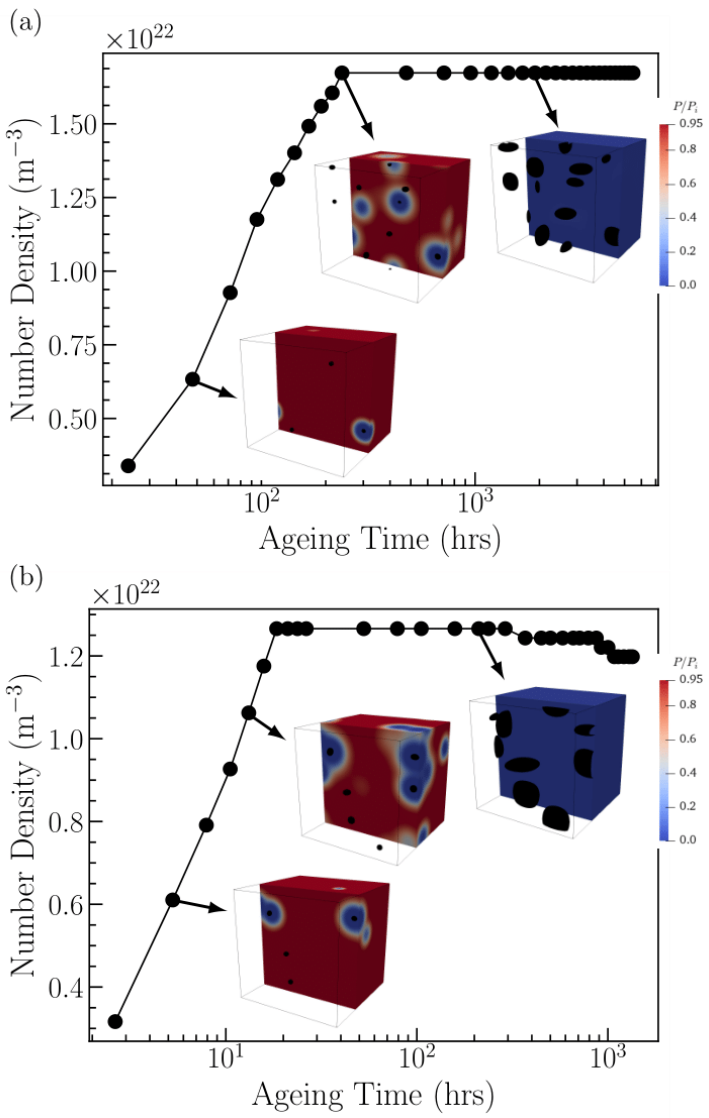

Figure 3.10 Simulated *γ''* number density evolution for aging at (a) 600 ℃ (b) 650 ℃. The contour plot inserts indicate the spatial distribution of nucleation probability (*P*) relative to the initial nucleation probability (P_i). The red regions indicate high nucleation probability and the blue regions indicate low nucleation probability. *γ''* particles are indicated by black spots.

3.3.3 Multistage aging strategy

Inconel 625 was originally designed as a solid-solution strengthened alloy [105], but precipitation hardening provided by the formation of *γ''* secondary phase has been discovered to

about double the yield strength of the alloy, albeit for a strict temperature range (550–750 ℃) and uneconomical aging time (hundreds or even thousands of hours) [105, 110, 111, 137]. Eiselstein *et al*. [105] cited this intermediate-temperature and sluggish aging response, as the major drawback of Inconel 625 compared to its counterpart Inconel 718. To this end, researchers have investigated possible means of decreasing the aging time of Inconel 625. One possible solution is by changes in composition giving raise to the creation of Inconel 625 plus which combines the excellent corrosion resistance of Inconel 625 and age-hardening capability of Inconel 718 [138, 139]. Another solution is by means of multistage heat treatment. For example, Eiselstein *et al*. [105] investigated a high temperature (760 ℃/1hr) heat treatment followed by aging at intermediate temperatures (621–677 ℃) to trigger the precipitation reaction and reduce the nucleation time. Although, the slow growth of γ'' still persists at the intermediate temperatures. In this section, we numerically explore a multistage low-to-high temperature heat treatments, where nucleation at intermediate temperature is followed by higher temperature aging to accelerate the growth of the precipitates, taking advantage of faster solute mobility at higher temperatures.

For the multistage aging, a nucleation treatment at 650 ℃ for 20 hours was chosen to avoid the heterogeneous nucleation of γ'' at grain boundaries, twin boundaries, and dislocations as observed by [107, 136, 140, 141] at higher temperatures. Also, the temperature 650 ℃ provides a reasonable incubation time of about 5 hours [106]. And after 20 hours, the maximum number density at 650 ℃ was achieved (Figure 3.10b). After the nucleation treatment, aging was carried out at higher temperatures (650–760 ℃), as illustrated in Figure 3.11a. The temperature dependent diffusivities, mobilities, elastic constants, interfacial energy, and Gibbs free energy calculated from the thermodynamic database [124] was used for the multistate aging simulations. All other parameters are the same as listed in Table 3.4. It is worth noting that the current model does not

account for heterogeneous nucleation behaviors. Heterogeneous nucleation can be considered in the model by either introducing a phenomenological heterogeneous nucleation factor to match the simulated nucleation number density with experimental observations [119], or by directly incorporating the microstructure features responsible for heterogeneous nucleation such as grain boundaries [142] and dislocations [143]. However, these investigations are beyond the scope of the current study and will be left for future work.

Figure 3.11 shows the microstructure evolution for the aging performed at different temperatures after the nucleation treatment. Qualitative assessment of Figure 3.11 shows that similar microstructure could be obtained if ageing is performed at higher temperatures and shorter times. For example, aging at 710 ℃ for 22 hours after nucleation treatment at 650 °C for 20 hours (Figure 3.11c) resulted in almost identical mean diameter and aspect ratio compared to isothermal aging at 650 ℃ for 366 hours (Figure 3.11b). Figure 3.12 shows the evolution of the mean particle length, aspect ratio, volume fraction, and number density for aging at different temperatures after nucleation treatment at 650 ℃. From Figure 3.12, it is apparent that increasing aging temperature accelerates the growth and coarsening of γ'', albeit at the expense of the volume fraction and number density. This provides an avenue for decreasing the heat treatment time for Inconel 625 when the effect of reduced volume fraction and particle number density (lower coherent strength) is accounted for. The decrease in number density (Figure 3.12d) is due to both the coalescence of γ'' particles belonging to the same antiphase domain and dissolution of smaller particles as a result of Ostwald ripening which is accelerated at elevated temperatures. The calculated mean length of the particles in the simulation volume increases as γ'' particles coalescence and smaller particles dissolve.

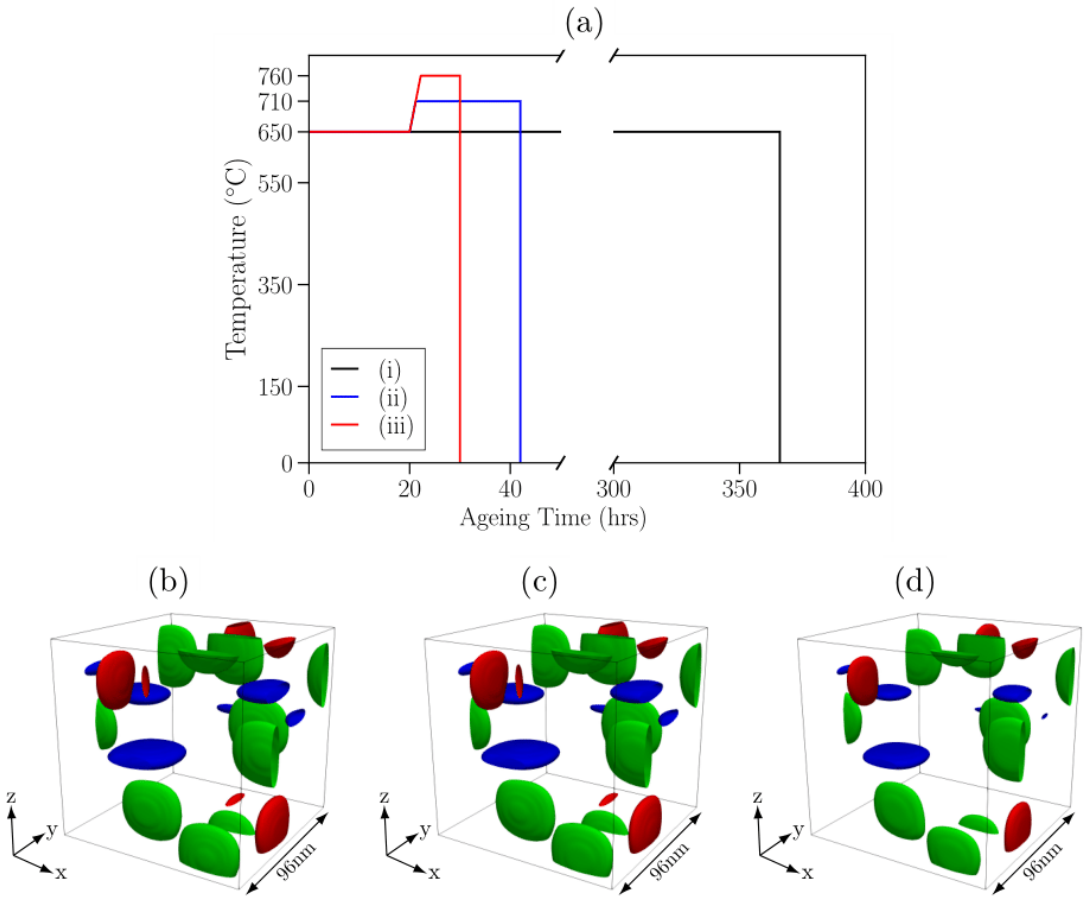

Figure 3.11 Various heat treatment schemes studied: (i) isothermal aging at 650°C for 366 hours; (ii) isothermal aging at 710 °C for 22 hours after nucleation treatment at 650 °C for 20 hours; (iii) isothermal aging at 760 °C for 10 hours after nucleation treatment at 650 °C for 20 hours (b), (c), (d) are the simulated microstructure evolution of γ'' precipitates in Inconel 625 for the various heat treatment schemes (i), (ii), and (iii), respectively. The phase-field simulations were performed in a $96 \times 96 \times 96$ nm^3 volume. The different colors represent different variants of γ''. The x-, y-, and z-axis represent [1 0 0], [0 1 0], and [0 0 1] directions, respectively.

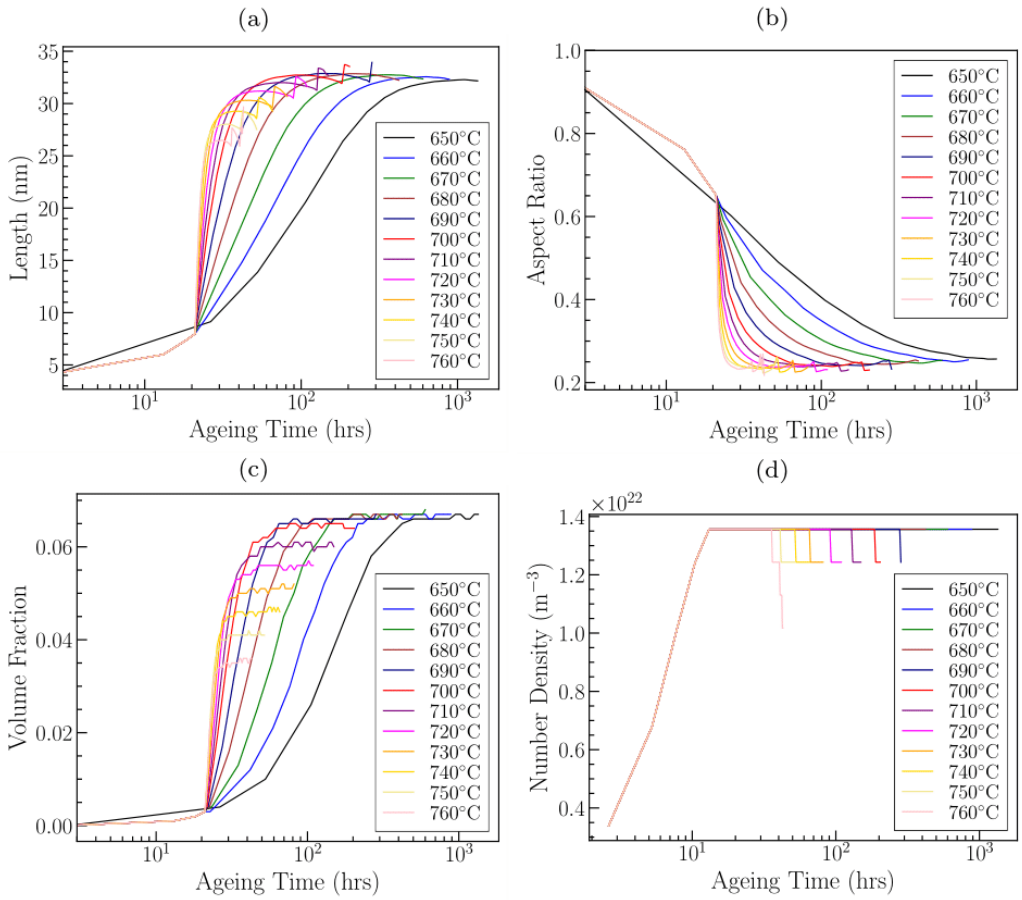

Figure 3.12 Simulated γ'' precipitation kinetics in Inconel 625 after 20 hours of nucleation treatment at 650 ℃ and subsequent aging at different temperatures. (a) Particle length. (b) Aspect ratio. (c) Volume fraction. (d) Number density.

3.3.4 Coherent strengthening effect of γ''

The main purpose of alloy aging is to increase the strength of the material through precipitation hardening. The increase in yield strength as a result of the coherent strengthening effect of γ'' can be calculated as [71, 144]:

$$\psi_{coherent} = 1.7MG|\epsilon|^{\frac{3}{2}}\left[\frac{h^2 f(1-\beta)}{2bR}\right]^{\frac{1}{2}} \tag{3.20}$$

where M is Taylor factor (3.06 for fcc materials), G is the shear modulus, ϵ is the tetragonal lattice misfit, f is the volume fraction of precipitates, R is the radius of the particles, h is the half thickness of the particles, β is a constant equals to $\frac{1}{3}$ when all the three variants are observed, and b is the magnitude of Burger's vector. We set $\epsilon = 0.0372$ [73], $G = 56$ GPa, and $b = 2.56$ Å [74]. R, h, and f are functions of aging time and were obtained from the phase-field simulations. Substituting all the values into Eq. (3.20), the coherent strengthening effect of γ'' as a function of aging time for both isothermal and multistage aging is calculated and plotted in Figure 3.13. From the figure it is apparent that coherent strengthening increases with aging time until a maximum value is reached, after which over-aging results in the decrease of coherent strengthening. For comparison, Eiselstein *et al*. [105] reported an increase in the yield strength at room temperature of about 525 MPa, for Inconel 625 samples isothermally aged at 650 ℃ for 1000 hours while the present calculations reports an increase of 600.0 MPa for the same aging conditions.

To obtain the optimal multistage aging strategy, a cost/benefit analysis was performed by comparing the time required to reach the maximum strength at different multistage aging temperatures with the time required to reach the maximum strength for isothermal aging at 650 ℃ (678.3MPa after 421.8 hours). Figure 3.14a shows the percent reduction in aging time and coherent strength loss as a function of aging temperature. Furthermore, defining the marginal benefit and marginal cost (Figure 3.14b) as the slope of the time reduction and strength loss curves, respectively, an optimal aging temperature of 697 ℃ is obtained (intersect in Figure 3.14b). Although simulation was not performed at 697 ℃, it was observed that multistage aging at 690 ℃ resulted in time reduction of 87% with a strength loss of 2.6%. And multistage aging at 700 ℃ resulted in time reduction of 90% with a strength loss of 5.7%. The intersect in Figure 12b is the point at which the ratio of the marginal benefit to marginal cost equals to unity. Aging at

temperatures above this point would result in the ratio of the marginal benefit to marginal cost being less than unity. Meaning that any incremental benefit gained (time reduction) will result in a much higher incremental strength loss. For example, aging at 710 ℃ will reduce aging time by 91% but will result in a 12.5% strength loss. The properties of γ'' precipitates at the instance of maximum $\psi_{coherent}$ for isothermal aging at 650 ℃ along with multistage aging at 690 ℃ and 700 ℃ is detailed in Table 3.5.

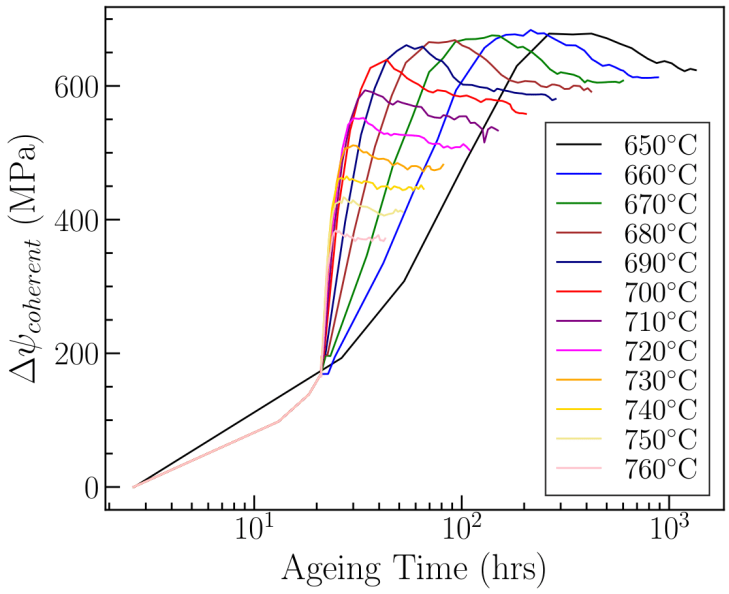

Figure 3.13 Coherent strength evolution in Inconel 625 for multistage aging at different temperatures after a 20-hour nucleation treatment at 650 ℃.

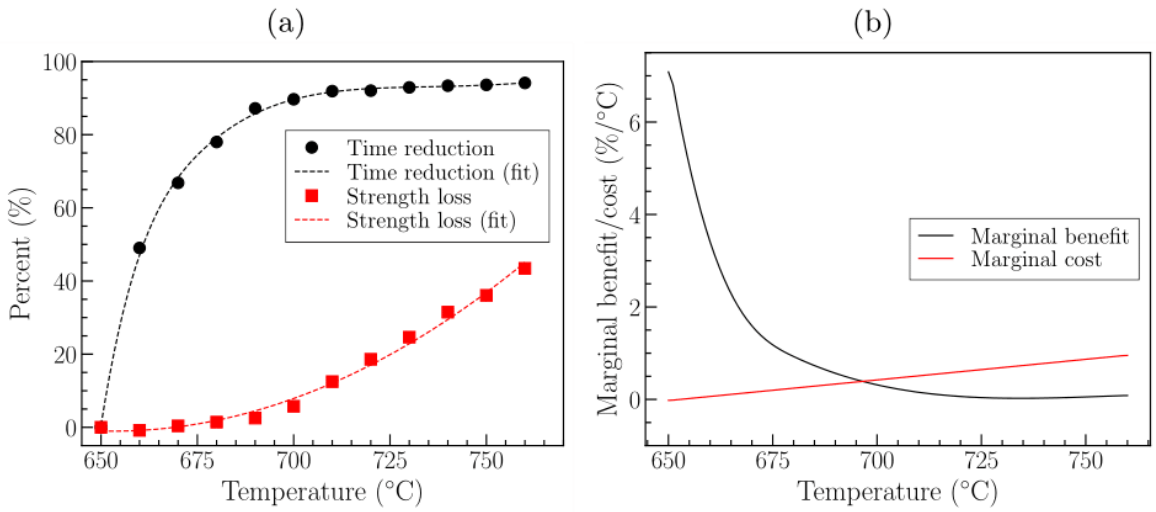

Figure 3.14 Cost benefit analysis. (a) percent reduction in time and strength versus temperature (b) marginal benefit/cost versus temperature.

Table 3.5 Characterization of γ'' in Inconel 625 at the instance of maximum $\psi_{coherent}$. MS refer to the multistage aged samples.

Aging Temperature (℃)	**Length (nm)**	**Thickness (nm)**	**Volume Fraction (%)**	$\boldsymbol{\psi_{coherent}}$ **(MPa)**	**Total Aging Time (hrs)**
650	31.3	8.8	6.5	678.3	421.8
690/MS	30.5	8.8	6.1	661.0	54.0
700/MS	30.8	8.5	6.1	639.3	43.6

3.4 Conclusions

In this study, we have developed a phase-field model to quantitatively investigate the γ" nucleation and growth kinetics in Inconel 625 alloys and its coherency strengthening effect as a function of aging time and temperature. Using validated input parameters, our benchmark 3D simulations under isothermal conditions have well reproduced the experimentally observed γ" morphology and precipitation kinetics. Due to the sluggish precipitation hardening response of

Inconel 625, we have numerically explored multistage non-isothermal aging strategies to reduce aging time and applied an analytical strengthening model to predict the resulting precipitation hardening effect. Based on systematic analyses, we find that:

(1) Increasing the isothermal aging temperature during the multistage treatment would lead to reduction of γ'' number density and volume fraction, which further decreases the γ'' strengthening effect: the balance between strengthening effect and precipitation kinetics is critical for the design of heat treatment strategy.

(2) A 20-hour nucleation treatment at 650 °C followed by aging at 700 °C for 24 hours can reduce the aging time by 90% with less than 6% loss of strength compared to isothermal aging at 650 °C for 422 hours.

(3) A reliable phase-field model for process-structure-property predictions would require careful parameterization and calibration with benchmark experiments or theoretical analysis (see Section 3.2.7 for example), and identification and mitigation of possible sources of any deviations (see Section 3.3.2 for example). The current model will be further improved based on these discussions.

This work is expected to provide practical guidance to optimize the strength of Inconel 625 superalloy while significantly reducing the aging time, subject to experimental corroboration of the proposed multistage aging strategy. Also, the developed methodology can be applied to the design and process optimization of other materials systems during both isothermal and non-isothermal heat treatments.

CHAPTER IV

EFFECT OF ELASTIC INHOMOGENEITY ON THE COARSENING KINETICS OF GAMMA PRIME PHASE IN NICKLE-BASED SUPERALLOYS

4.1 Introduction

Nickel-based superalloys offer a unique combination of outstanding strength, fatigue, corrosion, and oxidation resistance, which are maintained even at elevated temperatures [57]. Hence, their widespread application in critical components within the gas turbine engines used for jet propulsion and electricity generation. Precipitation strengthening through the formation of coherent $Ni_3(Al,Ti)$ γ' particles (ordered $L1_2$-type FCC unit cell structure) dispersed in the γ matrix phase (FCC solid solution) has proven to be a valuable mechanism to achieving the superior high temperature mechanical properties observed in these alloys [57, 63]. The phase transition induced by the heat treatment procedure results in the desired microstructure of finely distributed γ' precipitates inside the grain structures. The required size distribution, volume fraction, and shape of γ' are obtained by interrupting the heat treatment process, which also interrupts the phase transition process. As a result, the optimal γ/γ' microstructure is usually in a thermodynamic metastable state. Therefore, with prolonged high temperature exposure, the particles' size, morphology, and arrangement change continuously in an attempt to lower their energy state, resulting in the deterioration of the materials mechanical properties during in-service usage [145, 146].

One of the design goals for material scientists is to enhance the high temperature stability of the *γ/γ'* microstructure in nickel-based superalloys, thus retaining the high temperature mechanical strength by suppressing property degradation that is associated with microstructural evolution [145, 146, 147]. To achieve this goal, understanding of the coarsening process is paramount. Studies on the coarsening kinetics of *γ'* particles in binary [148, 149, 150, 151] and multicomponent [152, 153, 154, 155, 156] Ni-based alloys have reported that the coarsening kinetics of *γ'* can be described by the Lifshitz-Slyozov-Wagner (LSW) theory of particle coarsening [157, 158]. The LSW theory describes coarsening as a matrix-diffusion-controlled process driven by the free energy changes towards the reduction of precipitate matrix interfacial area/energy, according to which the average particle radius obeys the following temporal power law:

$$\langle R_t \rangle^n - \langle R_0 \rangle^n = Kt \tag{4.1}$$

where n is the growth law or coarsening exponent ($n = 3$ for diffusion controlled coarsening described by the LSW theory), $\langle R_t \rangle$ is the average radius at time t, $\langle R_0 \rangle$ is the mean radius at the start of coarsening or $t = 0$, and K is the coarsening rate constant which is a function of the interfacial energy, σ, the diffusion coefficient in the matrix phase, D_{ij}^m, and the second derivative of the free energy of the matrix phase with respect to the concentration in the matrix $f_{ij}^m \left(= \frac{\partial f^m}{\partial c_i^m \partial c_j^m} \right)$ [159]. One of the important predictions of the LSW theory is the value of the growth law, $n = 3$ for diffusion-controlled coarsening [157, 158]. This has allowed the prediction of the precipitate size as a function of time and the calculation of interfacial energy and the diffusion coefficients from experimental data of precipitate size time evolution [160].

The success of the LSW theory in predicting the coarsening kinetics in metal alloy system is remarkable given that the assumptions made in the development of the theory are not usually met in real alloy systems such as [161, 162]: (i) near zero volume fraction of particles or a dilute solid solution, (ii) the coarsening particles are spherical with no interactions or morphology change during coarsening, and (iii) the particles are fixed in space. Modifications to the classical LSW model has been proposed to address these assumptions. Calderon *et al*. [159] have modified the coarsening rate equation to incorporate substantial solute solubility in both the matrix and precipitate phases. Various modification to the classical LSW model has been proposed to overcome the assumption of near zero volume fraction [163, 164, 165, 166]. Davies *et al*. [167] proposed the "Lifshitz-Slyozov encounter modified theory" to account for the coalesce of particles during coarsening. However, the effect of coherent elastic strain and elastic inhomogeneity on the coarsening kinetics are not well addressed by the coarsening theories.

Coherent elastic strain originates due to the lattice mismatch between the precipitate and matrix phase, which has been shown to affect the morphology, growth and coarsening of the coherent precipitates in Ni-based superalloys [168, 169, 170]. The γ/γ' lattice misfit parameter is usually defined as:

$$\delta = \frac{2\left(a_{\gamma'} - a_{\gamma}\right)}{\left(a_{\gamma'} + a_{\gamma}\right)} \tag{4.2}$$

where $a_{\gamma'}$ and a_{γ} are the lattice parameters of the of the γ' and γ phase, respectively. Alloys with near-zero lattice misfit exhibit near-spherical precipitates morphology and a variety of shapes are usually observed for alloys with $|\delta| > 0$ [57, 169, 60]. Experimental and theoretical works have reported quantitative and qualitative differences between classical interfacial-energy driven

coarsening compared to coarsening in the presence of coherent elastic strain. Ardell and Nicholson [171] have shown that the evolution of γ' precipitates in Ni-Al alloys from spheres to cuboids to plate- or rod-like shapes, and the periodic arrangement of the precipitates along the elastically soft directions is due to the elastic interaction between the particles. Vaithyanathan and Chen [172] computational investigation of coarsening in ordered intermetallic precipitates with coherency stress reported that the coarsening rate constant from the cubic growth law decreases as a function of volume fraction for small volume fractions. This observation explains the "anomalous" coarsening behavior reported in experimental studies by Kim and Ardell [173]. Furthermore, experimental and theoretical reports by Miyazaki et. al. [174, 175] have shown deceleration or even stoppage of coarsening in some Ni-based alloys due to elastic constrain arising from the misfitting particles.

Elastic inhomogeneity describes the difference in the elastic constants between the precipitate phase and matrix phase. In general, elastic constant is defined as C_{ijkl} which can be represented in Voigt notation as C_{ij}. For materials with cubic symmetry, three independent elastic constants are needed to describe cubic anisotropy (C_{11}, C_{12}, C_{44}). From which three independent elastic quantities can be derived namely: bulk modulus, $B = C_{11} + C_{12}$, shear modulus, $G = 2C_{44}$, and anisotropy coefficient, $A = (2C_{44})/(C_{11} - C_{12})$. Although, there is no universal expression for the elastic inhomogeneity, Refs. [176, 177] have shown that the microstructure of γ' in Ni-based alloys is mainly sensitive to the inhomogeneity of $\Delta C'$, where $C' = (C_{11} - C_{22})/2$ is another shear modulus. It has been observed that as the value of $\Delta C'$ increases, the equilibrium distance (s_0) that minimizes the elastic energy between particles of size (s) also increases [177]. Therefore, coalesce of the particles is reduce and the average aspect ratio of the cuboidal particles

(s_{min}/s_{max}) decreases with increase in $\Delta C'$ [177]. Since $s_0 \approx s/2$, at high volume fraction, it might not be possible for the particles to separate by the equilibrium distance (s_0) [177, 178] .

Although, much investigation has been conducted on the effect of elastic inhomogeneity on the microstructure development in materials with cubic symmetry [177, 179, 180, 181, 182], research elucidating the effect of elastic inhomogeneity on the coarsening kinetics in nickel-based alloys is lacking in the open literature. Therefore, it is the aim of this work to investigate the effect of elastic inhomogeneity on the coarsening kinetics of the nickel-based alloys. Specifically, elastic inhomogeneity will be defined as $\Delta C'$. Although the value of $\Delta C'$ is hard to accurately measure in commercial superalloys, it has been reported that $\Delta C'$ could be as high as 50% in some nickle-based alloys [177]. Given that high volume fraction of γ' is desirable for high temperature applications, this research will focus on the coarsening kinetics of nickel-base alloys at high volume fraction of about 70%.

4.2 Methodology

The physics-based phase-field method [29, 8], which introduces the diffuse-interface concept to avoid the explicit tracking of interfaces, offers the significant potential to accurately predict precipitate morphology, growth, and coarsening kinetics in various alloy systems. As such, the phase-field method will be used in this study. The fundamental components in a phase-field model include: (i) a set of continuous order parameters to describe microstructures, (ii) free energies of the system as a function of these order parameters, and (iii) kinetic equations for the evolution of the order parameters.

A binary Ni-Al alloy is used to simulate the coarsening kinetics of γ' precipitates in the γ matrix. The composition (X_{Al}) is used to characterize the composition distribution in the two-phase microstructure. Four order parameters $\{\eta_1, \eta_2, \eta_3, \eta_4\}$ are used to describe the four different

domains in the $L1_2$ phase structure, $\{1,0,0,0\}$, $\{0,1,0,0\}$, $\{0,0,1,0\}$, $\{0,0,0,1\}$. Here, $\eta_p = 0$ corresponds to the matrix phase and $0 < \eta_p \leq 1$ corresponds to the *γ/γ'* interface. The total free energy functional for the system at a given temperature T can then be expressed as

$$F = \int_V \left[f_{bulk}(X_{Al}, \eta_p, T) + f_{grad}(\nabla \eta_p) + f_{el} \right] dV \tag{4.3}$$

where f_{bulk} is the bulk free energy density of the system, f_{grad} is the gradient energy due to inhomogeneous distribution of the order parameters, and f_{el} is the elastic strain energy density.

4.2.1 Bulk free energy density

The bulk free energy of the system is the sum of the Gibbs free energy of the different phases and the energy variation due to structural change. It can be expressed as

$$\begin{aligned} f_{bulk}(X_{Al}, \eta_p, T) = V_m^{-1} \cdot \left[1 - \sum_{p=1}^{4} h(\eta_p) \right] \cdot f^{\gamma}(X_{Al}^{\gamma}, T) \\ + V_m^{-1} \cdot \sum_{p=1}^{4} h(\eta_p) \cdot f^{\gamma'}\left(X_{Al}^{\gamma'}, T\right) + g(\eta_p) \end{aligned} \tag{4.4}$$

where $f^{\gamma}(X_{Al}^{\gamma}, T)$ and $f^{\gamma'}\left(X_{Al}^{\gamma'}, T\right)$ are the molar Gibbs free energy of γ and γ' phases, respectively, which can be obtained from a thermodynamic database. V_m is the molar volume, $h(\eta_p)$ is an interpolation function, and $g(\eta_p)$ is the sum of a double well and interaction energy function. The expressions for $h(\eta_p)$ and $g(\eta_p)$ are given by the following

$$h(\eta_p) = \eta_p^3 (6\eta_p^2 - 15\eta_p + 10) \tag{4.5}$$

$$g(\eta_p) = w^{\gamma'} \cdot \sum_{p=1}^{4} \eta_p^2 (1-\eta_p)^2 + \alpha \cdot \sum_{p=1}^{4} \sum_{p \neq q}^{4} \eta_p^2 \eta_q^2 \tag{4.6}$$

where $w^{\gamma'}$ defines the free energy hump between the matrix and the precipitate phase. The second term in Eq. (4.6) describes the free energy penalty that prevents different γ' variants from occupying the same spatial position and α is a constant parameter which determines the magnitude of the penalty.

The KKS model [49] is employed to remove the extra double-well potential of composition due to the equal composition assumption at interfaces [50, 51]. It assumes local equilibrium, rather than equal composition, at interfaces. This requires the solution of concentration fields in each phase from the following equations:

$$X_{Al} = X_{Al}^{\gamma} \cdot \left[1 - \sum_{p=1}^{4} h(\eta_p)\right] + X_i^{\gamma'} \cdot \sum_{p=1}^{4} h(\eta_p) \tag{4.7}$$

$$\frac{\partial f^{\gamma}}{\partial X_{Al}^{\gamma}} = \frac{\partial f^{\gamma'}}{\partial X_{Al}^{\gamma'}} \tag{4.8}$$

The non-linear molar Gibbs free energies of f^{γ} and $f^{\gamma'}$ were approximated by a Taylor series expansion at equilibrium compositions up to 2nd order as:

$$f_{para}^{\theta}(X_{Al}^{\theta}, T) = A^{\theta} + B_{Al}^{\theta}(X_{Al}^{\theta} - X_{Al}^{\theta,eq}) + \frac{1}{2} C_{Al,Al}^{\theta}(X_{Al}^{\theta} - X_{Al}^{\theta,eq})^2, \qquad \theta = \gamma, \gamma' \tag{4.9}$$

where $f_{para}^{\theta}(X_{Al}^{\theta}, T)$ is the parabolic approximation of $f^{\theta}(X_{Al}^{\theta}, T)$. The temperature dependent equilibrium composition of Al in phase θ is defined as $X_{Al}^{\theta,eq}$. The constants A^{θ}, B_{Al}^{θ},

and $C_{Al,Al}^{\theta}$ are temperature dependent Taylor expansion coefficients which can be calculated from a thermodynamic database as follows:

$$A^{\theta} = f^{\theta}\left(X_{Al}^{\theta,eq}, T\right) \tag{4.10}$$

$$B_{Al}^{\theta} = \left.\frac{\partial f^{\theta}}{\partial X_{Al}^{\theta}}\right|_{X_{Al}^{\theta}=X_{Al}^{\theta,eq}} \tag{4.11}$$

$$C_{Al,Al}^{\theta} = \left.\frac{\partial^2 f^{\theta}}{\partial\left(X_{Al}^{\theta}\right)^2}\right|_{X_{Al}^{\theta}=X_{Al}^{\theta,eq}} \tag{4.12}$$

Therefore, the first derivatives of the free energies with respect to concentration in Eq. (4.8) are linear functions of concentration. Hence, Eqs. (4.7) and (4.8) can be solved analytically through matrix inversions.

4.2.2 Gradient Energy Density

The gradient energy describes the energy penalty due to the inhomogeneous distribution of phase-field variables near interfaces expressed as the following

$$f_{grad} = \sum_{p=1}^{4} \frac{\kappa_p}{2} (\nabla \eta_p)^2 \tag{4.13}$$

where κ_p is the gradient energy coefficient which together with the barrier height w in Eq. (4.6), can be obtained from the interfacial energy (σ) and interface thickness (2λ) according to the following relationships [49]:

$$\sigma = \frac{\sqrt{\kappa \cdot w}}{3\sqrt{2}} \tag{4.14}$$

$$(2\lambda) = 2.2\sqrt{2} \cdot \sqrt{\frac{\kappa}{w}} \tag{4.15}$$

4.2.3 Elastic Energy Density

The elastic strain energy contribution due to lattice misfit between the precipitate and matrix is evaluated by Khachaturyan's microelasticity theory [33]:

$$f_{el} = \frac{1}{2}\sigma_{ij}\epsilon_{ij}^{el} \tag{4.16}$$

where σ_{ij} and are the elastic stress and elastic strain, respectively. If all the phases behave in a linear elastic manner and obey the Hooke's constitutive law, the position dependent stress field can be defined as:

$$\sigma_{ij} = C_{ijkl}(\eta_p)\epsilon_{kl}^{el} \tag{4.17}$$

where $C_{ijkl}(\eta_p)$ is the phase dependent elastic stiffness tensor. It is obtained by smoothly interpolating between the matrix (γ) and precipitate (γ') phases as:

$$C_{ijkl}(\eta_p) = C_{ijkl}^{\gamma}[1 - h(\eta_p)] + C_{ijkl}^{\gamma'}h(\eta_p) \tag{4.18}$$

Here C_{ijkl}^{γ} and $C_{ijkl}^{\gamma'}$ are the elastic constants of the γ and γ' phases, respectively, and $h(\eta_p)$ is the smooth interpolation function given in Eq. (4.5).

The elastic strain is defined as the difference between the total strain ϵ_{ij} and the local stress-free transformation strain $\left(\epsilon_{ij}^{0}\right)$ as [183]:

$$\epsilon_{ij}^{el} = \epsilon_{ij} - \epsilon_{ij}^{0}(\eta) \tag{4.19}$$

The local stress-free transformation strain is calculated as:

$$\epsilon_{ij}^{0}(\eta_p) = \epsilon_{ij}^{T} h(\eta_p) \tag{4.20}$$

where $\left(\epsilon_{ij}^{T}\right)$ is the crystallographic misfit strain tensor between the matrix and precipitate phases defined with respect to the matrix. Finally, the total strain is related to the displacements, u_i, as [183]:

$$\epsilon_{ij} = \frac{1}{2}\left[\frac{\partial u_i}{\partial x_j} + \frac{\partial u_j}{\partial x_i}\right] \tag{4.21}$$

It is assumed that the relaxation dynamics for elasticity are much faster than the diffusional phase transformation. Therefore, the time-independent equation for mechanical equilibrium is solved at each time step,

$$\nabla \cdot \sigma_{ij} = 0 \tag{4.22}$$

The equation of mechanical equilibrium, Eq. (4.22), can be solved numerically using an iterative procedure [184, 185, 181, 186]. The Fourier spectral iterative algorithm described by Moulinec and Suquet [185] is used in this work. The numerical algorithm and benchmark of the microelasticity solution is shown in APPENDIX A.

4.2.4 Kinetic equations

The diffusion and Allen-Cahn [32] equations are solved to obtain the spatial and temporal evolution of the concentration fields and order parameters, respectively:

$$\frac{\partial X_{Al}}{\partial t} = \nabla \cdot \left(M \nabla \frac{\partial f}{\partial X_{Al}} \right) \tag{4.23}$$

$$\frac{\partial \eta_p}{\partial t} = -L \left(\frac{\partial f_{bulk}}{\partial \eta_p} + \frac{\partial f_{el}}{\partial \eta_p} - k_p \nabla^2 \eta_p \right) \tag{4.24}$$

where t is the time, M is the chemical mobility and L is the kinetic coefficient for order parameter relaxation. The value of L is selected to ensure diffusion-controlled growth of the precipitates. The difference in chemical mobility between the precipitate and matrix phases can be taken into account by assuming an order-parameter-dependent chemical mobility as:

$$M(\eta_p) = M^{\gamma}\left[1 - h(\eta_p)\right] + M^{\gamma'} h(\eta_p) \tag{4.25}$$

where M^{γ} and $M^{\gamma'}$ are the chemical mobilities in γ and γ' phases, respectively, and $h(\eta_p)$ is a smooth interpolation function (Eq. (4.5)). The chemical mobility in phase θ can be estimated as:

$$M^{\theta} = \frac{D_{Al}^{\theta}}{V_m^{\theta} \frac{\partial^2 f^{\theta}}{\partial X^2}}, \quad \theta = \gamma, \gamma' \tag{4.26}$$

where $D_{Al}^{\theta} = D_0 exp\left(\frac{-Q_d}{RT}\right)$ $(\theta = \gamma, \gamma')$ is the temperature dependent diffusivity of Al in each phase. The kinetic equations (Eqs. (4.23) and (4.24)) are normalized by the simulation grid size l_0 and a reference energy density E_0 and were solved numerically using the semi-implicit

spectral method proposed by Chen and Shen [131]. Given the simulation gride size, l_0 and the unitless simulation time step size, Δt^*, the real time step can be calculated as:

$$\Delta t = \frac{(l_0)^2 \Delta t^*}{D_{Al}^{\gamma}} \tag{4.27}$$

All simulations were performed on 1 NVIDIA Tesla K20m GPU to improved computational efficiency. Benchmark result of the validation and speed up for the serial CPU code verse the parallel GPU code is shown in APPENDIX B.

4.2.5 Nucleation

The order-parameter-only nucleation algorithm by Jokisaari et. al. [54] was used to introduce the γ' nuclei into the simulation cell. The probability for nucleation at a simulation cell can be expressed as:

$$P = 1 - exp(-J^* \Delta t) \tag{4.28}$$

where Δt is the time interval over which the nucleation probability is calculated and J^* is the nucleation rate expressed as:

$$J^* = k_1 exp\left(\frac{-k_2}{\Delta X_{Al}}\right) \tag{4.29}$$

where k_1 and k_2 are adjustable parameters that control the nucleation rate and ΔX_{Al} is the supersaturation.

4.2.6 Simulation parameters

The parameters used for the phase-field simulation are detailed in Table 4.1. To study the effect of elastic inhomogeneity ($\Delta C'$) on the coarsening kinetics of γ', different alloys with varying $\Delta C'$ values were designed as shown in Table 4.2. Note that the anisotropy coefficient, A was kept as zero for all the cases. Using the simulation parameters, 2D simulations were performed on 2048×2048 simuation cell. To increase the statistical relevance of the result two simulation with different random seed were aggregated in the results presented herein.

Table 4.1 Parameters for phase-field simulation for the cases with misfit strain energy contribution

Parameters	**Description**	**Expression**
V_m	Molar volume	$1.06 \times 10^{-5}\ m^3/mol$
X_{Al}^0	Al initial matrix composition	0.225
D_{0Al}	Al diffusion prefactor	$1.0 \times 10^{-4}\ m^2/s$ [187]
Q_{Al}	Al diffusion activation energies	$260\ kJmol^{-1}$ [187]
σ	Interfacial energy	$0.02\,\frac{J}{m^2}$ [176]
l_0	Simulation grid size	$2.0\ nm$
E_0	Reference energy density	$2.5\ GPa$
(2λ)	Interface thickness	$2l_0$
L	Kinetic coefficient	$\frac{L^* D}{E_0 l_0^2}$, $L^* = 1$
C_{11}, C_{12}, C_{44}	Elastic constants	Table 4.2
ϵ_{ij}^0	Misfit strain tensor	$\begin{bmatrix} 0.005 & 0 & 0 \\ 0 & 0.0050 & 0 \\ 0 & 0 & 0.005 \end{bmatrix}$ [176]
k_1, k_2	Nucleation parameters	$5.26 \times 10^{-4},\ 2.50 \times 10^{-1}$
T	Temperature	$1073\ K$
$X_{Al,eq}^{\gamma}, X_{Al,eq}^{\gamma'}$	Equilibrium X_{Al}	0.141, 0.222

For the cases with no misfit strain energy contribution: $X_{Al}^0 = 0.195$, $k_1 = 5.26 \times 10^{-4}$, $k_2 = 1.5 \times 10^{-1}$

Table 4.2 Elastic constants of γ' phase for the different values of $\Delta C'$. The elastic constants for γ phase was fixed as: $C_{11}^{\gamma'} = 205.60\ GPa$, $C_{12}^{\gamma'} = 148.20\ GPa$, and $C_{44}^{\gamma'} = 93.70\ GPa$ [176].

$\Delta C'$	$C_{11}^{\gamma'}$	$C_{12}^{\gamma'}$	$C_{44}^{\gamma'}$
0%	205.60	148.20	93.70
10%	205.60	142.10	103.65
20%	205.60	135.40	114.60
30%	205.60	127.90	126.84
40%	205.60	119.40	140.70

4.3 Results and discussion

To analyze the phase-field simulation results, γ' precipitates were identified as regions with $|n_p| \geq 0.5$ and the γ matrix is defined as region with $|n_p| < 0.5$.

4.3.1 Morphological evolution of γ' precipitates

Figure 4.1 illustrates the time evolution of the simulated γ' morphology for case with no misfit strain energy contribution and for cases with misfit strain energy contribution with different values of elastic inhomogeneity $(\Delta C')$. The dark region represents the γ matrix phase and the four translational variants of γ' are represented by the different colors. During the nucleation stage (time step < 10^4), random nucleation of the different γ' variants occurred and a total of about 10000 precipitates of size $5l_0$ was introduced into the simulation domain. In Figure 4.1, at time step 10^4, most of the precipitates are near-circular shape, while some random shapes are present due to the interconnection/coalesce of neighboring particle with the same translational variant. The coalesce event is rampant during the early growth and coarsening stages. As the aging time increases, the near-circular shape particles coarsen, and the morphology of the precipitate is mostly cuboidal for cases with misfit strain energy contribution. For simulation with no misfit strain energy contribution, the precipitates maintain their near-circular shape throughout the simulation.

For simulation with misfit strain energy contribution, the change in the morphology of the precipitate from a near-circular to cuboidal shape is due to the interaction between the interfacial and elastic energy of the system. At the initial precipitation stage, the interfacial energy is dominate, resulting in the near-circular shape of most of the precipitates. As the size of the precipitate increases due to growth and coarsening processes, the elastic strain energy originating from the coherent strain dominates, resulting in the development of the cuboidal shaped particles. Another feature of microstructure development attributed to the elastic energy is the alignment of the particles along the vertical and horizontal directions corresponding to the elastically soft ⟨100⟩ directions. The particle alignment is due to the anisotropic elastic interaction (or configurational forces) between the particles [188]. The effect of elastic strain energy on the simulated morphologies of the γ' precipitates are similar to previously obtained experimental and simulation reports [189, 171].

The elastic strain energy effect on microstructure development offers material scientist higher degree of freedom for the development of novel superalloys for high temperature applications. For example, the alignment of particles along the ⟨100⟩ directions due to elastic interactions between particles was used to produce rafted structures in superalloys with improved high temperature creep properties [190]. Fine turning of the precipitate shape by controlling the degree of lattice misfit can also be used to optimize the properties of highly creep resistant Ni-base alloys [169, 191].

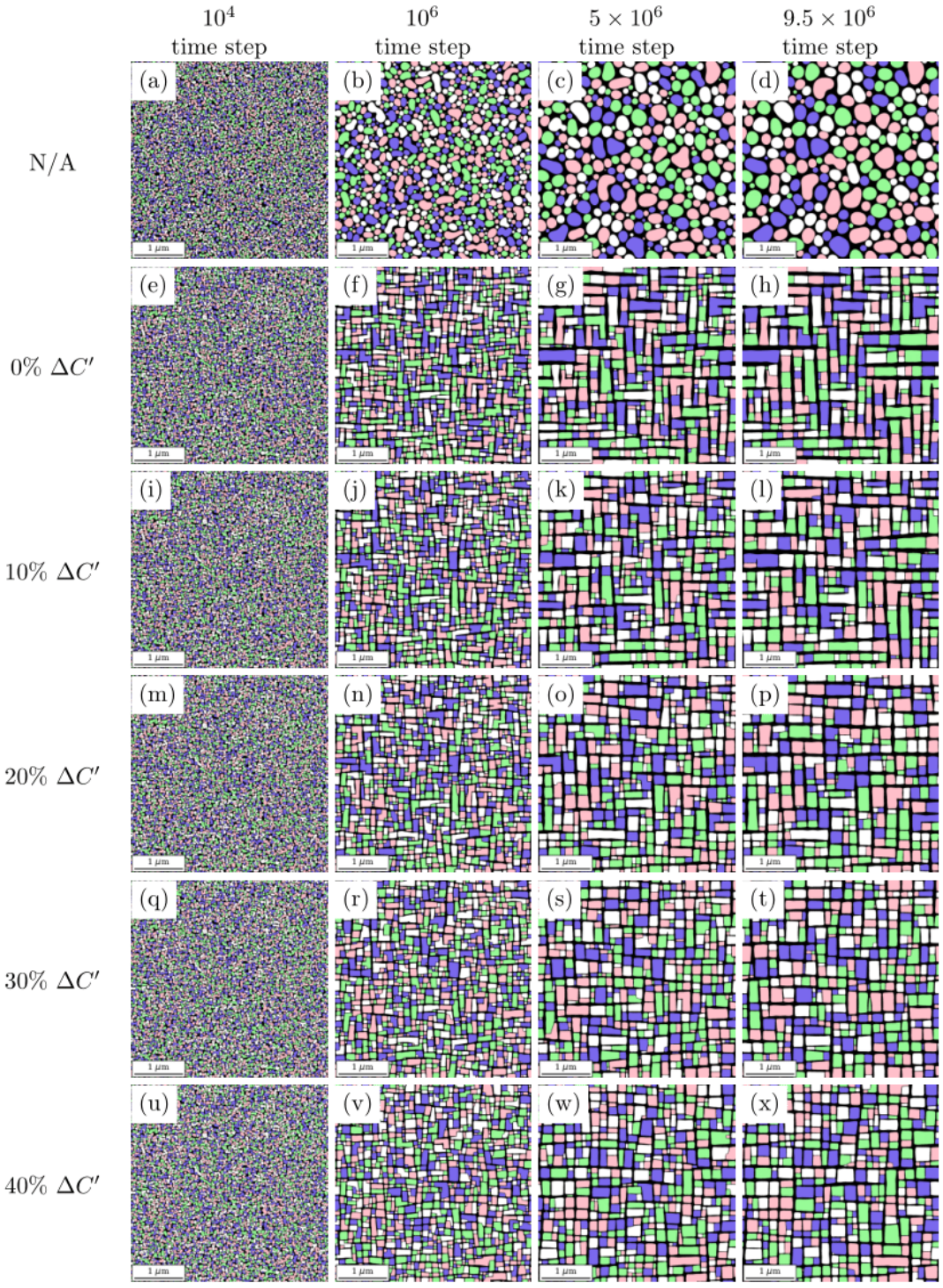

Figure 4.1 Evolution of γ' morphology with simulation time step at different $\Delta C'$ levels (a-d) N/A (e-h) 0% (i-l) 10% (m-p) 20% (q-t) 30% (u-x) 40%

As the coarsening progresses, a total of about 500 precipitates remains in the simulation domain at 9.5×10^6 time step. Similar growth and coarsening morphological development are observed for samples with misfit strain energy contribution. However, the coalescence of same translational variant particles is less frequent as the elastic inhomogeneity, $\Delta C'$ increases. Therefore, the average particle aspect ratio (l_{max}/l_{min}) decreases as $\Delta C'$ increases. Figure 4.2a shows the evolution of the average aspect ratio for all simulated cases. From the figure, the case with no misfit strain energy contribution exhibits a rapid decrease in the average aspect ratio of the precipitates to a pseudo-equilibrium value of about 1.1 which is close to circular shape with aspect ratio of 1.0. Due to misfit strain energy contribution the aspect ratio of the other cases increases with simulation time as the precipitates transition from a near-circular shape (interfacial energy dominated regime) to a cuboidal shape (misfit strain energy dominated regime).

Following Qiu [192], the fraction of precipitates with different aspect ratios (i.e. the volume of precipitates with different aspect ratios, normalized by the total precipitate volume in the microstructure) is calculated for the late stage at time 9.5×10^6 time step for all the simulated cases as shown in Figure 4.2b. The precipitate shapes are represented by different ranges of the aspect ratio (AR): AR = 1 (AR < 1.5) represents precipitates with near-circular or square shapes, AR = 2 (1.5 < AR < 2.5) implies rectangular-shaped precipitates, and AR = 3 (2.5 < AR < 3.5) and AR = 4 (AR > 3.5) represent plate shaped precipitates. From Figure 4.2b. it can be observed that the fraction of precipitates with square shape increases with increasing values of $\Delta C'$ until at $\Delta C' = 20\% - 40\%$ where no difference can be observed. The fraction of precipitates with either rectangular shape or plate-shape generally decrease with increasing values of $\Delta C'$ until at $\Delta C' = 20\% - 40\%$ where no difference can be observed. As observed by [177], the equilibrium distance between the particles increases with increase in $\Delta C'$ because the elastic energy related to C' is

mainly localized along the edges of the precipitate, indicating that particle-particle interaction is mostly sensitive to the value of C'. Therefore, at higher values of $\Delta C'$, the frequency of particles coalesce is lower. It is important to note that the values of AR = 1, AR = 2, AR = 3, and AR = 4 of 0.48, 0.40, 0.10, and 0.03, respectively for homogeneous elastic constants are in agreement with the results of Vaithyanathan and Chen [172] who reported values of 0.44, 0.38, 0.13, and 0.04 for AR = 1, AR = 2, AR = 3, and AR = 4, respectively at 0.7 volume fraction.

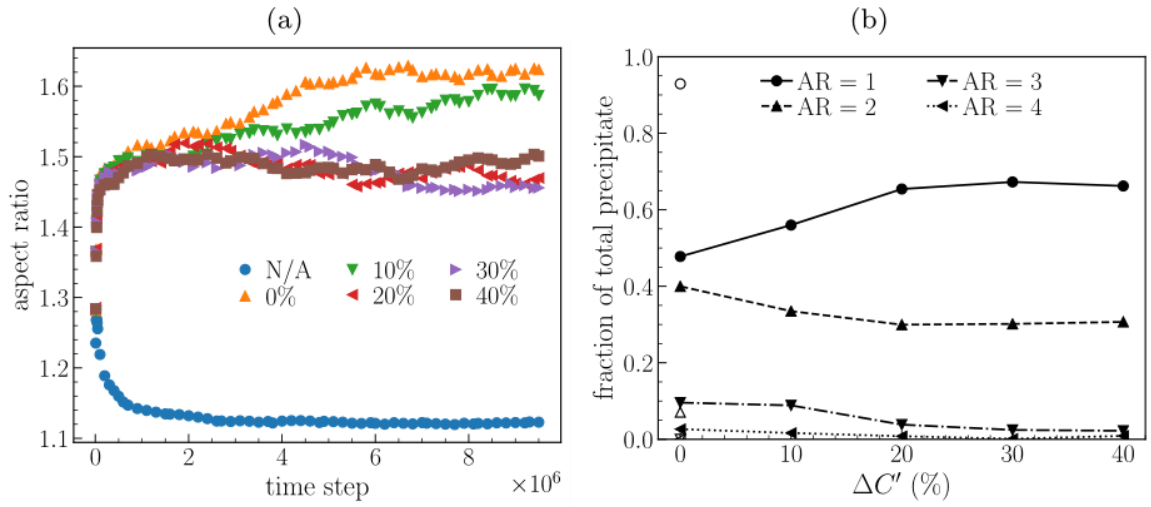

Figure 4.2 Aspect ratio analysis (a) average aspect ratio evolution during aging for different values of $\Delta C'$ (b) fraction of precipitates with different aspect ratios as a function of the equilibrium precipitate volume fraction at 9.5×10^6 time step.

4.3.2 Volume fraction

Figure 4.3 shows the evolution of the volume fraction of γ' with simulation time step for all values of $\Delta C'$. During the early aging stages, the volume fraction of γ' increases monotonically due to free diffusional growth of the nucleated γ' precipitates in the supersaturated γ matrix. During the later aging stages, the volume fraction of γ' reaches a pseudo-equilibrium level due to the

decrease of the supersaturation in the matrix, elastic interactions, and competition for solute between particles. It can be observed that the volume fraction increases with increase in the elastic inhomogeneity ($\Delta C'$) even for the same initial composition value, $X_{Al}^{0} = 0.225$. This is because of the difference in the partitioning of X_{Al} as a function of $\Delta C'$. It is important to mention that $X_{Al}^{0} = 0.195$ for the case with no elastic energy to ensure similar volume fractions. Figure 4.4 shows the distribution of X_{Al} in the microstructure at 9.5×10^{6} time step. From the figure, it is evident that X_{Al} strongly partition into the γ' phase. Further analysis of the average composition of X_{Al} in the γ and γ' phase as a function of $\Delta C'$ is shown in Figure 4.5. As seen from the figure, focusing on the cases with elastic energy contribution (black circular markers), it can be observed that the composition of X_{Al} in both γ and γ' phases decrease as $\Delta C'$ increases, resulting in the increase in the volume fraction (Figure 4.3). It is interesting to highlight that for the case with only interfacial energy contribution (square marker), the average composition in the precipitate and matrix phase are close to the equilibrium composition $\left(X_{Al,eq}^{\gamma} = 0.141,\ X_{Al,eq}^{\gamma'} = 0.222\right)$. The slight increase of the average composition in the precipitate phase is due to the Gibbs Thomson effect which causes an increase in equilibrium compositions at interface [193]. Furthermore, the cases with misfit strain energy contribution display even higher average composition in the precipitate compared to the equilibrium composition.

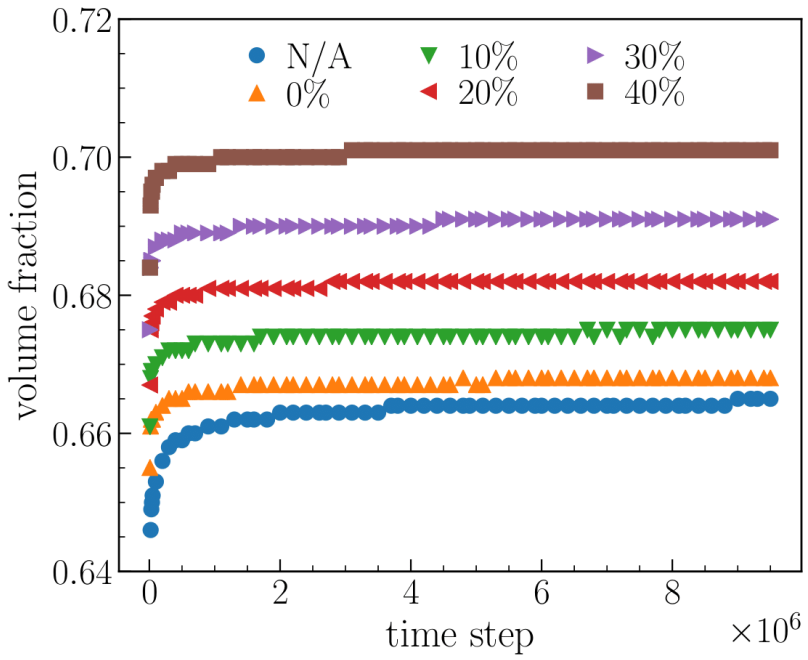

Figure 4.3 Evolution of γ' volume fraction with simulation time step for different values of $\Delta C'$.

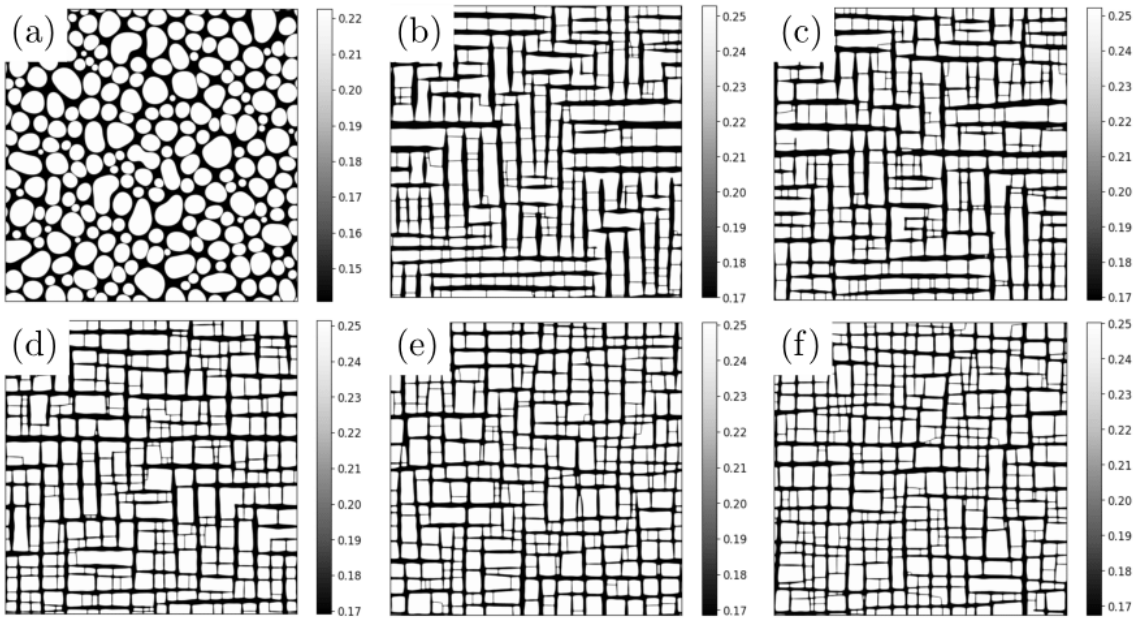

Figure 4.4 Distribution of X_{Al} composition for different values of $\Delta C'$ (a) N/A (b) 0% (c) 10% (d) 20% (e) 30% (f) 40%

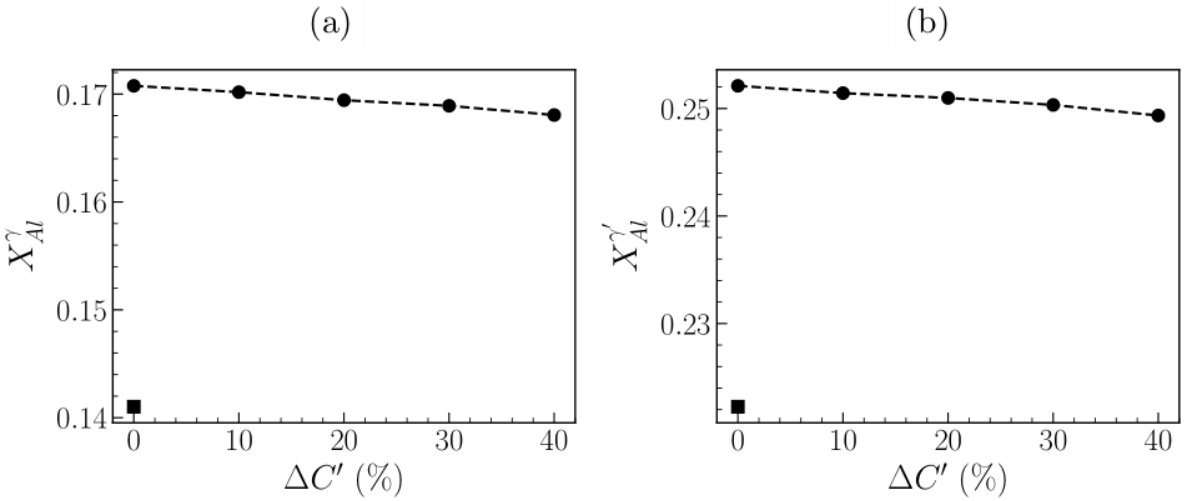

Figure 4.5 Average concentration of X_{Al} for different values of $\Delta C'$ (a) in the matrix, γ (b) in the precipitate, γ'.

4.3.3 γ' precipitate count evolution

Figure 4.6 shows the time evolution of γ' precipitate count. A total of about 10000 precipitates where available after nucleation. The particle count began decreasing due to the coalesce of γ' particles of the same translational variant during the early stages. The decrease in the particle count at the later aging stages is dominated by coarsening, were the smaller particles dissolve due to diffusive mass transfer to fuel the growth of larger particles. It can be observed that the rate at which the number of particles decrease is greater for the case with no misfit strain energy contribution. Also, during the late coarsening stages, the number of particles decreases at a slower rate as the elastic inhomogeneity increases.

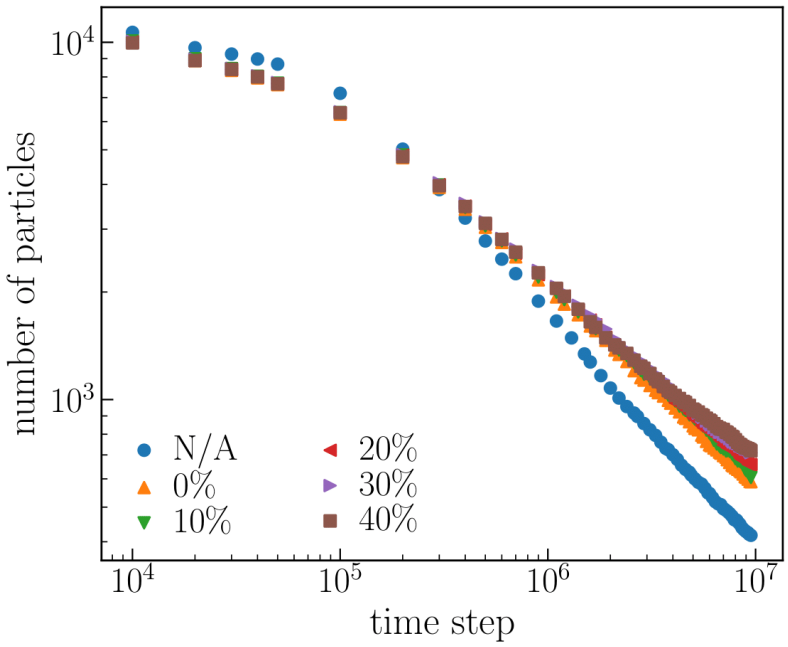

Figure 4.6 Evolution of particle count with simulation time step for different values of $\Delta C'$.

4.3.4 γ' particle size evolution

The average particle size is calculated as:

$$\langle R \rangle = \frac{1}{N}\sum_{i=1}^{N} R_i \tag{4.30}$$

where N is the number of particles in the system and R_i is the dimensionless circularly equivalent radius defined by $R_i = \sqrt{A_i/\pi}$, A_i is the dimensionless area of the i^{th} particle. It is usually customary to plot $\langle R \rangle^3$ versus time, from which, either through visual inspection or examination of the goodness of fit, the cubic rate law as predicted by the LSW theory is confirmed. Such a plot is shown in Figure 4.7. From visual inspection, it can be observed that the particles coarsen according to the cube rate law for low values of $\Delta C'$. However, at higher values of $\Delta C'$, deiviation from the cube rate law can be observed and deceleration of the coarsening rate constant can be observed during the late coarsening stages. The declaration of the coarsening rate during the later coarsening stages is well documented in various experimental studies [155, 174, 175, 194, 195, 196]. Some of these researchers attributed the decelerated coarsening behavior observed to be due to the inverse coarsening, the growth of the smaller particles at the expense of larger once, induced by the elastic interaction energy [174, 175, 194, 195, 196]. However, inverse coarsening was not observed in this study. Instead, the decelerated coarsening can be understood by considering that the increase in elastic inhomogeneity, $\Delta C'$ results in increase in the elastic energy [177]. And as the particle size increases, the buildup in the elastic energy accumulates in the matrix, causing a reduction in the total driving force for coarsening [180].

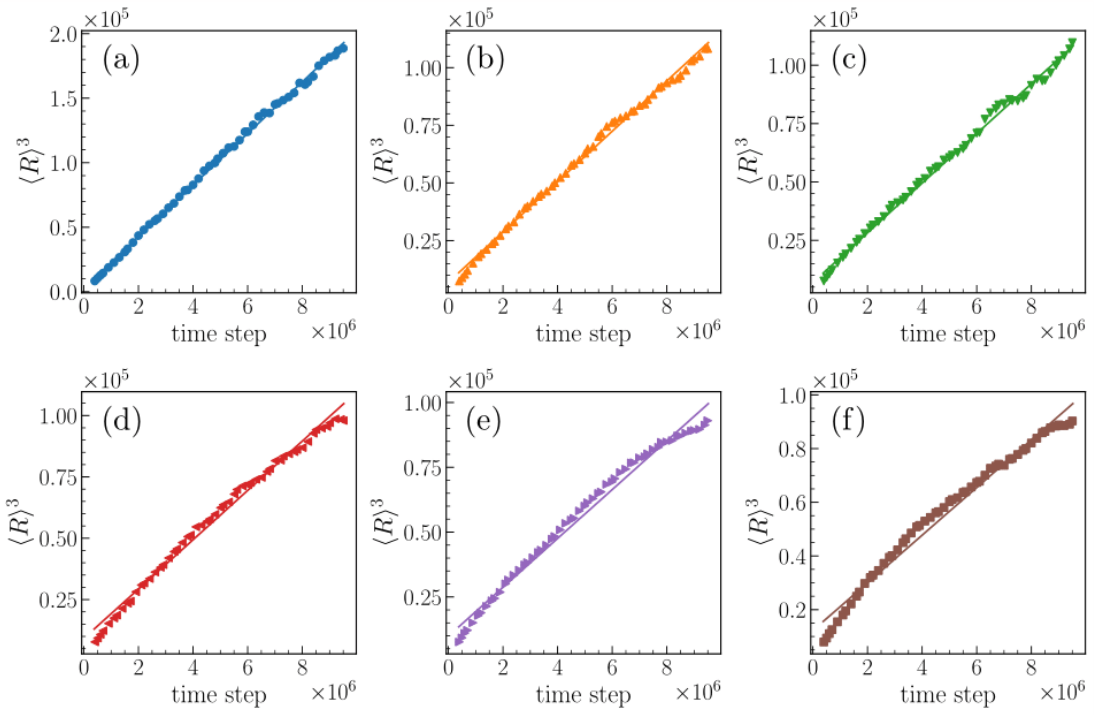

Figure 4.7 The cube of the average size as a function of time for different values of $\Delta C'$ (a) N/A (b) 0% (c) 10% (d) 20% (e) 30% (f) 40%

A nonlinear fit in the form of (Eq. (4.1)) was fitted to the precipitate time growth data with the coarsening exponent, n and coarsening rate constant, K shown in Figure 4.8. For the case with no misfit strain energy contribution, it can be observed that the coarsening exponent, $n = 3.07$ is in agreement with the predicted value by the LSW theory $(n = 3)$ [157, 158]. For the cases with misfit strain energy contribution, the coarsening exponents, was higher than the predicted value by the LSW theory. Generally, n and K value increases as the elastic inhomogeneity, $\Delta C'$ increases, indicating a slower coarsening kinetics. It's worth noting that the coarsening exponent in systems with substantial elastic interactions is still a point of contention. The experiment results for systems with elastic misfit strains may be divided into two groups: one reports that the coarsening exponent value remains constant and follows the LSW theory $(n = 3)$ [197, 198], while the other reports a

change in kinetics represented by a change in the coarsening exponent [175, 192]. Numerical analysis by Leo *et al* [199] shows that if coarsening progresses in a scale invariant manner, then the coarsening exponent in the stress dominated regime is 2. Nishimori and Onuki [179] reported a coarsening exponent of 5 in the late stages. For a homogeneous elastic system, computer simulation by Vaithyanathan and Chen [172] show coarsening exponents close to 3 when either half-edge length or equivalent radius are used for characterizing the length scale. These discrepancy highlights the need for a comprehensive theory of coarsening in system with significant misfit strain and elastic inhomogeneity.

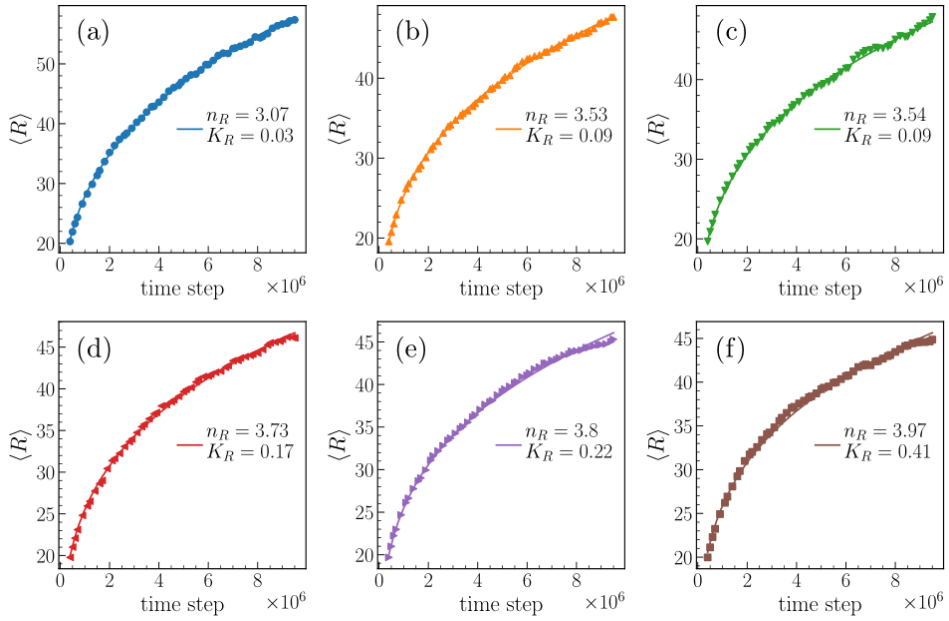

Figure 4.8 Average precipitate size as a function of simulation time along with nonlinear fit using Eq. 4.1 for different values of $\Delta C'$ (a) N/A (b) 0% (c) 10% (d) 20% (e) 30% (f) 40%

4.3.5 Particle size distribution

To characterize the size homogeneity of the precipitates, the particle size distributions (PSD) for all values of $\Delta C'$ at the late ageing stage was plotted in Figure 4.9. The gray histograms

are the simulation results, the red dashed lines are the theoretical values of the LSW theory, and the blue dashed lines are results from the LSEM model. The LSW PSD is narrower and exhibits a higher peak than the simulation results. This deviation is due to infinite small volume fraction assumption by the LSW theory. The LSEM PSD provides a better fit to the simulation results because the model incorporates the effect of volume fraction. However, the peak of the PSD predicted by the LSEM model is higher than the simulation results. It is interesting to mention that no significant difference in the PSD for simulations with varying elastic inhomogeneity was observed.

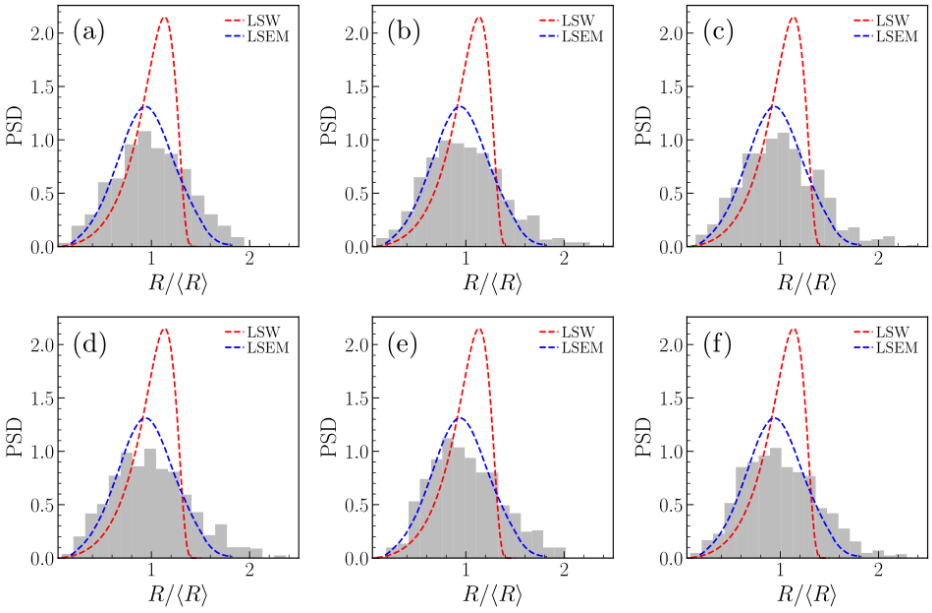

Figure 4.9 Scaled precipitate size distributions at from simulation results at 9.5×10^6 time step compared with theoretical PSD from LSW and LSEM (70% volume fraction) for different values of $\Delta C'$ (a) N/A (b) 0% (c) 10% (d) 20% (e) 30% (f) 40%

4.4 Conclusion

In this chapter, a phase-field model was developed to study the precipitation kinetics of γ' phase in Ni-based alloys. Specifically, the study focused on the effect of elastic inhomogeneity ($\Delta C'$) between the γ' precipitates and γ matrix on the microstructure development, coarsening kinetics, and PSD. Also, a control case with no misfit strain energy effect was simulated. It was observed that the elastic inhomogeneity strongly dictates the aspect ratio of the precipitates. In the presence of misfit strain energy, the precipitates with no elastic inhomogeneity displayed a more rectangular shaped morphology due to coalesce with neighboring precipitates of the same orientation variant. As the elastic inhomogeneity increases, the precipitates exhibit a more square shared morphology and coalesce with neighboring precipitates of the same orientation variant is less frequent. For the control simulation with no misfit strain energy effect, the precipitates are spherical in shape and coarsen according to the LSW theory with coarsening exponent, $(n = 3.07)$. However, the cases with elastic strain energy effect do exhibit higher coarsening exponents values ranging from 3.53 to 3.97. The coarsening exponents was observed to increase as the elastic inhomogeneity increases. No significant difference was observed for the PSD of all simulations.

CHAPTER V

SUMMARY AND FUTURE WORK

5.1 Summary

In this dissertation, the precipitation in nickel-based superalloys was studied. Specifically, the phase-field model was used to elucidate the precipitation kinetic of the strengthening phases, γ' and γ'' in nickel-based superalloys, with the goal of providing a computational tool to understand the microstructure development and optimize processing parameters and mechanical properties of the alloys. The summary of the chapters in this work are as follows:

1. Chapter 1 covers the motivation behind the need for using ICME paradigm for materials engineering. The multiscale approach to modeling precipitation was highlighted. Also, the chapter covers a historic review of the development of the phase-field model for precipitation. Finally, the general recipe for the formulation of the phase-field model for precipitation was discussed.
2. In Chapter 2, the nickel-based superalloy was reviewed. The typical precipitating phases in the alloy during solidification, heat treatment, or prolong high temperature service use was covered along with the effect of the phases on the mechanical properties of the alloy. The main precipitation phases in most nickel-based superalloys are the γ' and γ'', experimental observation of the precipitation kinetic of these phases was discussed.

3. A phase-field model to study the precipitation kinetics of γ'' in Inconel 625 was developed in Chapter 3. The developed model was validated with experimental data for isothermal aging. Using the phase-field model, a non-isothermal multistage aging was proposed that increases the strength of Inconel 625 by 160% and reduces the aging time by 90%.
4. In chapter 4, a phase-field model to study the precipitation kinetics of the γ' phase in nickel-based superalloys was developed. The effect of elastic inhomogeneity on the precipitation kinetics for a higher volume fracture of γ' phase was studied. It was observed the coarsening rate constant does not follow the LSW theoretical value of 3. The coarsening rate constant increases as the elastic inhomogeneity increases.

5.2 Future work

The phase-field method is a high-fidelity approach for simulating the microstructure development in materials. However, it is still very computational expensive to apply the phase-field approach to complex materials systems (e.g., many alloying elements and many precipitating phases). Therefore, future research should focus on designing scalable numerical models for solving the phase-field equations on high performance heterogenous architectures. With performant numerical approach the phase-field method in this work would be extended to study polycrystals alloys with many alloying elements and many precipitating phases. Furthermore, addition of a crystal plasticity framework to the current phase-field model will enable the direct prediction of the mechanical properties of the material from microstructure information.

REFERENCES

[1] M. F. Horstemeyer, Integrated Computational Materials Engineering (ICME) for metals: using multiscale modeling to invigorate engineering design with science, John Wiley & Sons, 2012.

[2] M. F. Horstemeyer, Integrated Computational Materials Engineering (ICME) for Metals: Concepts and Case Studies, John Wiley & Sons, 2018.

[3] W. Yang, Z. Wang, C. Yenusah and Y.-C. Liu, "An Integrated Model for Prediction of Process-Structure-Property Relationship for Additively Manufactured Al-10Si-Mg Alloy," *SAE Technical Paper Series,* vol. 1, 2020.

[4] R. A. Perkins, W. H. Yang, Y.-C. Liu, L. Chen and C. Yenusah, "Finite Element Analysis of the Effect of Porosity on the Plasticity and Damage Behavior of Mg AZ31 and Al 6061 T651 Alloys," in *ASME International Mechanical Engineering Congress and Exposition*, Vol. 59469, p. V009T11A055, 2019.

[5] C. O. Yenusah, Y. Ji, Y.-C. Liu, T. W. Stone, M. F. Horstemeyer and L. Chen, "Investigating the Precipitation Kinetics and Hardening Effects of γ" in Inconel 625 Using a Combination of Meso-Scale Phase-Field Simulations and Macro-Scale Precipitate Strengthening Calculations," in *ASME International Mechanical Engineering Congress and Exposition,* Vol. 84508, p. V003T03A006, 2020.

[6] X. Wang, Y. Liu, L. Li, C. O. Yenusah, Y. Xiao and L. Chen, "Multi-scale phase-field modeling of layer-by-layer powder compact densification during solid-state direct metal laser sintering," *Materials & Design,* vol. 203, p. 109615, 2021.

[7] X. Wang, C. O. Yenusah, K. Tantratian, M. L. Meyerson, A. Guo, C. B. Mullins, L. Zhu and L. Chen, "Understanding the mechanism of stress mitigation in selenium-doped germanium electrodes," *Journal of The Electrochemical Society,* vol. 166, no. 2, p. A364, 2019.

[8] C. O. Yenusah, Y. Ji, Y.-C. Liu, T. W. Stone, M. F. Horstemeyer, L. Q. Chen and L. Chen, "Three-dimensional Phase-field simulation of γ″ precipitation kinetics in Inconel 625 during heat treatment," *Computational Materials Science,* vol. 187, p. 110123, 2021.

[9] W. Yang, Z. Wang, T. Yang, L. He, X. Song, Y.-C. Liu and L. Chen, "Exploration of the Underlying Space in Microscopic Images via Deep Learning for Additively Manufactured Piezoceramics," *ACS applied materials & interfaces,* vol. 13, no. 45, pp. 53439-53453, 2021.

[10] Z. Wang, X. Wang, W. Yang, Y. Xiao, Y.-C. Liu and L. Chen, "yNet: a multi-input convolutional network for ultra-fast simulation of field evolvement," *arXiv: 2012.10575,* 2020.

[11] T. Gladman, "Precipitation hardening in metals," *Materials science and technology,* vol. 15, no. 1, pp. 30-36, 1999.

[12] R. Kampmann and R. Wagner, "Kinetics of Precipitation in Metastable Binary Alloys: Theory and Application to Copper--1. 9 at.% Titanium and Nickel--14 at.% Aluminium(Alloys)," *Decomposition of alloys: the early stages,* pp. 91-103, 1983.

[13] J. Svoboda, F. D. Fischer, P. Fratzl and E. Kozeschnik, "Modelling of kinetics in multi-component multi-phase systems with spherical precipitates: I: Theory," *Materials Science and Engineering: A,* vol. 385, no. 1-2, pp. 166-174, 2004.

[14] W. A. Johnson and R. F. Mehl, "Reaction kinetics in processes of nucleation and growth," *Transactions of the American Institute of Mining and Metallurgical Engineers,* vol. 135, pp. 396-415, 1939.

[15] M. Asta, V. Ozolins and C. Woodward, "A first-principles approach to modeling alloy phase equilibria.," *JOM,* vol. 53, no. 9, pp. 16-19, 2001.

[16] M. A. Blanco, E. Francisco and V. Luana, "GIBBS: isothermal-isobaric thermodynamics of solids from energy curves using a quasi-harmonic Debye model.," *Computer Physics Communications,* vol. 158, no. 1, pp. 57-72, 2004.

[17] Y. Wang, S. L. Shang, H. Fang, Z. K. Liu and L. Q. Chen, "First-principles calculations of lattice dynamics and thermal properties of polar solids.," *npj Computational Materials,* vol. 2, no. 1, pp. 1-10, 2016.

[18] V. Vaithyanathan, C. Wolverton and L. Q. Chen, "Multiscale modeling of precipitate microstructure evolution.," *Physical review letters,* vol. 88, no. 12, p. 125503, 2002.

[19] N. Saunders and A. P. Miodownik, "CALPHAD (calculation of phase diagrams): a comprehensive guide.," *Elsevier,* 1998.

[20] C. Wolverton, "First-principles theory of 250 000-atom coherent alloy microstructure," *Modelling and Simulation in Materials Science and Engineering,* vol. 8, no. 3, p. 323, 2000.

[21] S. L. Shang, W. Y. Wang, B. C. Zhou, Y. Wang, K. A. Darling, L. J. Kecskes, S. N. Mathaudhu and Z. K. Liu, "Generalized stacking fault energy, ideal strength and twinnability of dilute Mg-based alloys: a first-principles study of shear deformation," *Acta materialia,* vol. 67, pp. 168-180, 2014.

[22] M. Mantina, Y. Wang, R. Arroyave, L. Q. Chen, Z. K. Liu and C. Wolverton, "First-principles calculation of self-diffusion coefficients.," *Physical review letters,* vol. 100, no. 21, p. 215901, 2008.

[23] M. Mantina, Y. Wang, L. Q. Chen, Z. K. Liu and C. Wolverton, "First principles impurity diffusion coefficients," *Acta Materialia,* vol. 57, no. 14, pp. 4102-4108, 2009.

[24] Y. Dou, Y.-C. Liu, B. Huddleston, Y. Hammi and M. F. Horstemeyer, "A molecular dynamics study of effects of crystal orientation, size scale, and strain rate on penetration mechanisms of monocrystalline copper subjected to impact from a nickel penetrator at very high strain rates," *Acta Mechanica,* vol. 231, no. 6, pp. 2173-2201, 2020.

[25] G. He, Y. Dou, X. Guo and Y.-C. Liu, "Computational investigation of effects of grain size on ballistic performance of copper," *International Journal for Computational Methods in Engineering Science and Mechanics,* vol. 19, no. 1, pp. 1-10, 2018.

[26] Y.-C. Liu and Y. Dou, "A Computational Study of Crystal Orientation Effects on High Strain Rate Performance of Single Crystal Copper," *SAE Technical Paper (No. 2019-01-0714),* 2019.

[27] Y. Dou and Y.-C. Liu, "A multiscale study of single crystal copper plate with octal orientation struck by a nickel projectile," *SAE Technical Paper (No. 2018-01-1210),* 2018.

[28] G. He, Y. Dou, X. Guo and Y.-C. Liu, "Effects of grain size on ballistic response of copper materials," *ASME International Mechanical Engineering Congress and Exposition,* vol. 58493, p. V014T11A004, 2017.

[29] L.-Q. Chen, "Phase-field models for microstructure evolution," *Annual review of materials research,* vol. 32, pp. 113-140, 2002.

[30] N. Moelans, B. Blanpain and P. Wollants, "An introduction to phase-field modeling of microstructure evolution.," *Calphad,* vol. 32, no. 2, pp. 268-294, 2008.

[31] W. Cahn J and E. Hilliard J, "Free Energy of a Nonuniform System. I. Interfacial Free Energy.," *The Journal of Chemical Physics,* vol. 28, p. 258–267, 1958.

[32] S. M. Allen and J. W. Cahn, "A microscopic theory for antiphase boundary motion and its application to antiphase domain coarsening," *Acta metallurgica,* vol. 27, pp. 1085-1095, 1979.

[33] A. G. Khachaturyan, "Theory of structural transformation in solids," 1983.

[34] L. Q. Chen and A. G. Khachaturyan, "Computer simulation of structural transformations during precipitation of an ordered intermetallic phase," *Acta metallurgica et materialia,* vol. 39, no. 11, pp. 2533-2551, 1991.

[35] H. Zapolsky, S. Ferry, X. Sauvage, D. Blavette and L. Q. Chen, "Kinetics of cubic-to-tetragonal transformation in Ni–V–X alloys," *Philosophical Magazine,* vol. 90, no. 1-4, pp. 337-355, 2010.

[36] T. M. Radchenko, V. A. Tatarenko, H. Zapolsky and D. Blavette, "Statistical-thermodynamic description of the order–disorder transformation of D019-type phase in Ti–Al alloy," *Journal of alloys and compounds,* vol. 452, no. 1, pp. 122-126, 2008.

[37] L. Q. Chen and Y. Wang, "The continuum field approach to modeling microstructural evolution," *Jom,* vol. 48, no. 12, pp. 13-18, 1996.

[38] Y. Wang, H. Wang, L. Q. Chen and A. G. Khachaturyan, "Shape evolution of a coherent tetragonal precipitate in partially stabilized cubic zro2: a computer simulation," *Journal of the American Ceramic Society,* vol. 76, no. 12, pp. 3029-3033, 1993.

[39] L. Q. Chen and W. Yang, "Computer simulation of the domain dynamics of a quenched system with a large number of nonconserved order parameters: The grain-growth kinetics," *Physical Review B,* vol. 50, no. 21, p. 15752, 1994.

[40] D. Fan and L. Q. Chen, "Computer Simulation of Twin Formation during the Displacive c→ t′ Phase Transformation in the Zirconia-Yttria System," *Journal of the American Ceramic Society,* vol. 78, no. 3, pp. 769-773, 1995.

[41] R. Poduri and L. Q. Chen, "Computer simulation of the kinetics of order-disorder and phase separation during precipitation of δ′(Al3Li) in Al-Li alloys.," *Acta materialia,* vol. 45, no. 1, pp. 245-255, 1997.

[42] D. Y. Li and L. Q. Chen, "Selective variant growth of coherent Ti11Ni14 precipitate in a TiNi alloy under applied stresses," *Acta materialia,* vol. 45, no. 2, pp. 471-479, 1997.

[43] V. Vaithyanathan and L. Q. Chen, "Coarsening kinetics of δ′-Al3Li precipitates: phase-field simulation in 2D and 3D.," *Scripta materialia,* vol. 42, no. 10, pp. 967-973, 2000.

[44] J. Z. Zhu, Z. K. Liu, V. Vaithyanathan and L. Q. Chen, "Linking phase-field model to CALPHAD: application to precipitate shape evolution in Ni-base alloys," *Scripta Materialia,* vol. 46, no. 5, pp. 401-406, 2002.

[45] J. Z. Zhu, T. Wang, S. H. Zhou, Z. K. Liu and L. Q. Chen, "Quantitative interface models for simulating microstructure evolution," *Acta materialia,* vol. 52, no. 4, pp. 833-840, 2004.

[46] Y. H. Wen, L. Q. Chen, P. M. Hazzledine and Y. Wang, "A three-dimensional phase-field model for computer simulation of lamellar structure formation in γTiAl intermetallic alloys," *Acta materialia,* vol. 49, no. 12, pp. 2341-2353, 2001.

[47] J. Z. Zhu, T. Wang, A. J. Ardell, S. H. Zhou, Z. K. Liu and L. Q. Chen, "Three-dimensional phase-field simulations of coarsening kinetics of γ′ particles in binary Ni–Al alloys," *Acta materialia,* vol. 52, no. 9, pp. 2837-2845, 2004.

[48] C. Shen, Q. Chen, Y. H. Wen, J. P. Simmons and Y. Wang, "Increasing length scale of quantitative phase field modeling of growth-dominant or coarsening-dominant process.," *Scripta materialia,* vol. 50, no. 7, pp. 1023-1028, 2004.

[49] S. G. Kim, W. T. Kim and T. Suzuki, "Phase-field model for binary alloys," *Physical review e,* vol. 60, p. 7186, 1999.

[50] A. A. Wheeler, W. J. Boettinger and G. B. McFadden, "Phase-field model of solute trapping during solidification," *Physical Review E,* vol. 47, no. 3, p. 1893, 1993.

[51] A. A. Wheeler, W. J. Boettinger and G. B. McFadden, "Phase-field model for isothermal phase transitions in binary alloys," *Physical Review A,* vol. 45, no. 10, p. 7424, 1992.

[52] J. P. Simmons, C. Shen and Y. Wang, "Phase field modeling of simultaneous nucleation and growth by explicitly incorporating nucleation events," *Scripta materialia,* vol. 43, pp. 935-942, 2000.

[53] J. P. Simmons, Y. Wen, C. Shen and Y. Z. Wang, "Microstructural development involving nucleation and growth phenomena simulated with the phase field method," *Materials Science and Engineering: A,* vol. 365, pp. 136-143, 2004.

[54] A. M. Jokisaari, C. Permann and K. Thornton, "A nucleation algorithm for the coupled conserved–nonconserved phase field model," *Computational Materials Science,* vol. 112, pp. 128-138, 2016.

[55] I. Steinbach, "Phase-field models in materials science," *Modelling and simulation in materials science and engineering,* vol. 17, no. 7, p. 073001, 2009.

[56] J. H. Perepezko, "The hotter the engine, the better," *Science,* vol. 326, no. 5956, pp. 1068-1069, 2009.

[57] R. C. Reed, The superalloys: fundamentals and applications, Cambridge university press, 2008.

[58] G. Blaine, H. Leon and X. Huang, Superalloys: alloying and performance, ASM International, 2010.

[59] R. Scharfrik and R. Sprague, "The saga of gas turbine materials, Part III," *Advanced Materials and Processes,* vol. 162, pp. 33-35, 2004.

[60] T. M. Pollock and S. Tin, "Nickel-based superalloys for advanced turbine engines: chemistry, microstructure and properties," *Journal of propulsion and power,* vol. 22, no. 2, pp. 361-374, 2006.

[61] R. Darolia, "Development of strong, oxidation and corrosion resistant nickel-based superalloys: critical review of challenges, progress and prospects.," *International Materials Reviews,* vol. 64, no. 6, pp. 355-380, 2019.

[62] L. Haibo, S. Mao, Y. Liu, Z. Zhang and X. Han, "Microstructural and compositional design of Ni-based single crystalline superalloys—a review," *Journal of Alloys and Compounds,* vol. 743, pp. 203-220, 2018.

[63] C. T. Sims, N. S. Stoloff and W. C. Hagel, Superalloys II (Vol. 8), New York: Wiley, 1987.

[64] T. Murakumo, T. Kobayashi, Y. Koizumi and H. Harada, "Creep behaviour of Ni-base single-crystal superalloys with various γ′ volume fraction," *Acta Materialia,* vol. 52, no. 12, pp. 3737-3744, 2004.

[65] E. Nembach and G. Neite, "Precipitation hardening of superalloys by ordered γ′-particles," *Progress in Materials Science,* vol. 29, no. 3, pp. 177-319, 1985.

[66] M. Chandran and S. K. Sondhi, "First-principle calculation of APB energy in Ni-based binary and ternary alloys.," *Modelling and Simulation in Materials Science and Engineering,* vol. 19, no. 2, p. 025008, 2011.

[67] M. P. Jackson and R. C. Reed, "Heat treatment of UDIMET 720Li: the effect of microstructure on properties," *Materials Science and Engineering: A,* vol. 259, no. 1, pp. 85-97, 1999.

[68] R. Nicholson, Strengthening methods in crystals, halsted Press, 1972.

[69] W. Hüther and B. Reppich, "Interaction of dislocations with coherent, stress-free, ordered particles," *International Journal of Materials Research,* vol. 69, no. 10, pp. 628-634, 1978.

[70] J. S. Van Sluytman, "Microstructure and high temperature creep of platinum group metal modified nickel base superalloys," *Doctoral dissertation, University of Michigan,* 2010.

[71] J. M. Oblak, D. F. Paulonis and D. S. Duvall, "Coherency strengthening in Ni base alloys hardened by $D0_{22}$ γ" precipitates," *Metallurgical Transactions,* vol. 5, p. 143, 1974.

[72] A. Devaux, L. Nazé, R. Molins, A. Pineau, A. Organista, J. Y. Guédou, J. F. Uginet and P. Héritier, "Gamma double prime precipitation kinetic in Alloy 718," *Materials Science and Engineering: A,* vol. 486, pp. 117-122, 2008.

[73] R. Cozar and A. Pineau, "Influence of coherency strains on precipitate shape in a Fe-Ni-Ta alloy," *Scripta Metallurgica,* vol. 7, pp. 851-854, 1973.

[74] Y. Ji, Y. Lou, M. Qu, J. D. Rowatt, F. Zhang, T. W. Simpson and L.-Q. Chen, "Predicting Coherency Loss of γ" Precipitates in IN718 Superalloy," *Metallurgical and Materials Transactions A,* vol. 47, pp. 3235-3247, 2016.

[75] H. Qin, Z. Bi, R. Zhang, L. T. L., H. Yu, H. Chi, D. Li, H. Dong, J. Du and J. Zhang, "Stress-Induced Variant Selection of γ″ Phase in Inconel 718 During Service: Mechanism and Effects on Mechanical Behavior.," *Superalloys,* pp. 713-725, 2020.

[76] H. Zhang, C. Li, Q. Guo, Z. Ma, H. Li and Y. Liu, "Improving creep resistance of nickel-based superalloy Inconel 718 by tailoring gamma double prime variants," *Scripta Materialia,* vol. 164, pp. 66-70, 2019.

[77] E. L. Raymond and D. A. Wells, "Effects of aluminum content and heat treatment on gamma prime structure and yield strength of Inconel nickel-chromium Alloy 706," *Superalloys 1972,* pp. N1-N21, 1972.

[78] I. J. Moore, M. G. Burke and E. J. Palmiere, "Modelling the nucleation, growth and coarsening kinetics of γ" ($D0_{22}$) precipitates in the Ni-base Alloy 625," *Acta Materialia,* vol. 119, pp. 157-166, 2016.

[79] M. Sundararaman, P. Mukhopadhyay and S. Banerjee, "Precipitation of the δ-Ni 3 Nb phase in two nickel base superalloys," *Metallurgical transactions A,* vol. 19, no. 3, pp. 453-465, 1988.

[80] Y. Rong, S. Chen, G. X. Hu, M. Gao and R. P. Wei, "Prediction and characterization of variant electron diffraction patterns for γ″ and δ precipitates in an INCONEL 718 alloy," *Metallurgical and Materials Transactions A,* vol. 30, no. 9, pp. 2297-2303, 1999.

[81] I. Kirman and D. H. Warrington, "The precipitation of Ni3Nb phases in a Ni-Fe-Cr-Nb alloy," *Metallurgical Transactions,* vol. 1, no. 10, pp. 2667-2675, 1970.

[82] J. P. Collier, S. H. Wong, J. K. Tien and J. C. Phillips, "The effect of varying AI, Ti, and Nb content on the phase stability of INCONEL 718," *Metallurgical Transactions A,* vol. 19, no. 7, pp. 1657-1666, 1988.

[83] J. Cardenas, H. Guajardo, C. Harwood and J. A. Manriquez, "Effects of large reductions and heating temperature-times on grain size control of alloy 718 rolled rings," *Proceedings of the international symposium on superalloys 718, 625, 706 and various derivatives,* pp. 119-133, 2005.

[84] H. T. Lee and W. H. Hou, "Influence of precipitated phase formation on recrystallization behavior of superalloy 718," *Materials Transactions,* p. M2012090, 2012.

[85] E. O. Hall, "The deformation and ageing of mild steel: III discussion of results," *Proceedings of the Physical Society. Section B,* vol. 64, no. 9, p. 747, 1951.

[86] N. J. Petch, "The cleavage strength of polycrystals.," *Journal of the Iron and Steel Institute,* vol. 174, pp. 25-28, 1953.

[87] J. H. Moll, G. N. Maniar and D. R. Muzyka, "Heat treatment of 706 alloy for optimum 1200 F stress-rupture properties," *Metallurgical and Materials Transactions B,* vol. 2, no. 8, pp. 2153-2160, 1971.

[88] S. Azadian, L. Y. Wei and R. Warren, "Delta phase precipitation in Inconel 718," *Materials characterization,* vol. 53, no. 1, pp. 7-16, 2004.

[89] V. Shankar, K. B. S. Rao and S. L. Mannan, "Microstructure and mechanical properties of Inconel 625 superalloy," *Journal of nuclear materials,* vol. 288, no. 2-3, pp. 222-232, 2001.

[90] H. J. Penkalla, J. Wosik, W. Fischer and F. Schubert, "Structural investigations of candidate materials for turbine disc applications beyond 700 deg C," *Fifth International Symposium on Superalloys 718, 625, 706 and Various Derivatives,* pp. 279-290, 2001.

[91] G. K. Bouse, "Eta (η) and Platelet Phases in Investment Cast Superalloys," *Superalloys,* vol. 8, p. 163–172, 1996.

[92] B. G. Choi, I. S. Kim, D. H. Kim, S. M. Seo and C. Y. Jo, "Eta phase formation during thermal exposure and its effect on mechanical properties in Ni-base superalloy GTD 111," *Superalloys (Tenth International Symposium),* pp. 163-171, 2004.

[93] R. Darolia, D. F. Lahrman and R. D. Field, "Formation of topologically closed packed phases in nickel base single crystal superalloys," *Superalloys 1988,* pp. 255-264, 1988.

[94] C. M. Rae and R. C. Reed, "The precipitation of topologically close-packed phases in rhenium-containing superalloys," *Acta materialia,* vol. 49, no. 19, pp. 4113-4125, 2001.

[95] M. Simonetti and P. Caron, "Role and behaviour of μ phase during deformation of a nickel-based single crystal superalloy," *Materials Science and Engineering: A,* vol. 254, no. 1-2, pp. 1-12, 1998.

[96] R. C. Reed, D. C. Cox and C. M. F. Rae, "Damage accumulation during creep deformation of a single crystal superalloy at 1150 C," *Materials Science and Engineering: A,* vol. 448, no. 1-2, pp. 88-96, 2007.

[97] C. M. F. Rae, M. S. A. Karunaratne, C. J. Small, R. W. Broomfield, C. N. Jones and R. C. Reed, "Topologically close packed phases in an experimental rhenium-containing single crystal superalloy," *Superalloys 2000,* pp. 767-776, 2000.

[98] S. Tin, T. M. Pollock and W. T. King, "Carbon additions and grain defect formation in high refractory nickel-base single crystal superalloys," *Superalloys 2000,* pp. 201-210, 2000.

[99] M. Sundararaman, P. Mukhopadhyay and S. Banerjee, "Carbide precipitation in nickel base superalloys 718 and 625 and their effect on mechanical properties," *Superalloys,* pp. 625-706, 1997.

[100] Q. Z. Chen, C. N. Jones and D. M. Knowles, "The grain boundary microstructures of the base and modified RR 2072 bicrystal superalloys and their effects on the creep properties," *Materials Science and Engineering: A,* vol. 385, no. 1-2, pp. 402-418, 2004.

[101] L. Z. He, Q. Zheng, X. F. Sun, H. R. Guan, Z. Q. Hu, A. K. Tieu, C. Lu and H. T. Zhu, "Effect of carbides on the creep properties of a Ni-base superalloy M963," *Materials Science and Engineering: A,* vol. 397, no. 1-2, pp. 297-304, 2005.

[102] K. Zhao, Y. H. Ma and L. H. Lou, "Improvement of creep rupture strength of a liquid metal cooling directionally solidified nickel-base superalloy by carbides," *Journal of alloys and compounds,* vol. 475, no. 1-2, pp. 648-651, 2009.

[103] Z. Xu, L. Jiang, J. Dong, Z. Li and X. Zhou, "The effect of silicon on precipitation and decomposition behaviors of M6C carbide in a Ni–Mo–Cr superalloy," *Journal of Alloys and Compounds,* vol. 620, pp. 197-203, 2015.

[104] Y. S. Lim, D. J. Kim, S. S. Hwang, H. P. Kim and S. W. Kim, "M23C6 precipitation behavior and grain boundary serration in Ni-based Alloy 690," *Materials characterization,* vol. 96, pp. 28-39, 2014.

[105] H. L. Eiselstein and D. J. Tillack, "The invention and definition of Alloy 625," *Superalloys,* vol. 718, pp. 1-14, 1991.

[106] S. Floreen, G. E. Fuchs and W. J. Yang, "The metallurgy of Alloy 625," *Superalloys,* vol. 718, pp. 13-37, 1994.

[107] L. M. Suave, J. Cormier, P. Villechaise, A. Soula, Z. Hervier, D. Bertheau and J. Laigo, "Microstructural evolutions during thermal aging of Alloy 625: impact of temperature and forming process," *Metallurgical and materials transactions A,* vol. 45, pp. 2963-2982, 2014.

[108] X. Wang, P. W. Liu, Y. Ji, Y.-C. Liu, M. Horstemeyer and L. Chen, "Investigation on microsegregation of IN718 alloy during additive manufacturing via integrated phase-field and finite-element modeling," *Journal of Materials Engineering and Performance,* vol. 28, no. 2, pp. 657-665, 2019.

[109] P. W. Liu, Z. Wang, Y. H. Xiao, R. A. Lebensohn, Y.-C. Liu, M. F. Horstemeyer, X. Y. Cui and L. Chen, "Integration of phase-field model and crystal plasticity for the prediction of process-structure-property relation of additively manufactured metallic materials," *International Journal of Plasticity,* vol. 128, p. 102670, 2020.

[110] J. F. Radavich and A. Fort, "Effects of long-time exposure in Alloy 625 at 1200 ºF, 1400 ºF and 1600 ºF," *Superalloys,* vol. 718, pp. 635-647, 1994.

[111] C. R. Conder, G. D. Smith and J. F. Radavich, "Microstructural and mechanical property characterization of aged Inconel alloy 625LCF," *Superalloys 718, 625, 706 and various derivatives,* pp. 447-458, 1997.

[112] I. J. Moore, M. G. Burke, N. T. Nuhfer and E. J. Palmiere, "Evaluation of classical precipitation descriptions for in γ" (Ni_3Nb-$D0_{22}$) Ni-base superalloys," *Journal of Materials Science,* vol. 52, pp. 8665-8680, 2017.

[113] N. Zhou, D. C. Lv, H. L. Zhang, D. McAllister, F. Zhang, M. J. Mills and Y. Wang, "Computer simulation of phase transformation and plastic deformation in IN718 superalloy: microstructural evolution during precipitation," *Acta Materialia,* vol. 65, pp. 270-286, 2014.

[114] Y. Gao, H. Liu, R. Shi, N. Zhou, Z. Xu, Y. M. Zhu, J. F. Nie and Y. Wang, "Simulation study of precipitation in an Mg--Y--Nd alloy," *Acta Materialia,* vol. 60, pp. 4819-4832, 2012.

[115] H. Liu, Y. Gao, J. Z. Liu, Y. M. Zhu, Y. Wang and J. F. Nie, "A simulation study of the shape of β' precipitates in Mg--Y and Mg--Gd alloys," *Acta Materialia,* vol. 61, pp. 453-466, 2013.

[116] Y. Z. Ji, A. Issa, T. W. Heo, J. E. Saal, C. Wolverton and L.-Q. Chen, "Predicting β' precipitate morphology and evolution in Mg--RE alloys using a combination of first-principles calculations and phase-field modeling," *Acta Materialia,* vol. 76, pp. 259-271, 2014.

[117] V. Vaithyanathan, C. Wolverton and L. Q. Chen, "Multiscale modeling of θ' precipitation in Al--Cu binary alloys," *Acta Materialia,* vol. 52, pp. 2973-2987, 2004.

[118] S. Y. Hu, J. Murray, H. Weiland, Z. K. Liu and L. Q. Chen, "Thermodynamic description and growth kinetics of stoichiometric precipitates in the phase-field approach," *Calphad,* vol. 31, pp. 303-312, 2007.

[119] Y. Ji, B. Ghaffari, M. Li and L.-Q. Chen, "Phase-field modeling of θ' precipitation kinetics in 319 aluminum alloys," *Computational Materials Science,* vol. 151, pp. 84-94, 2018.

[120] R. Shi, N. Ma and Y. Wang, "Predicting equilibrium shape of precipitates as function of coherency state," *Acta Materialia,* vol. 60, pp. 4172-4184, 2012.

[121] M. A. Zaeem, H. El Kadiri, M. F. Horstemeyer, M. Khafizov and Z. Utegulov, "Effects of internal stresses and intermediate phases on the coarsening of coherent precipitates: A phase-field study," *Current Applied Physics,* vol. 12, no. 2, pp. 570-580, 2012.

[122] M. A. Zaeem, H. El Kadiri, S. D. Mesarovic, M. F. Horstemeyer and P. T. Wang, "Effect of the compositional strain on the diffusive interface thickness and on the phase transformation in a phase-field model for binary alloys," *Journal of phase equilibria and diffusion,* vol. 32, no. 4, pp. 302-308, 2011.

[123] R. Shi, D. P. McAllister, N. Zhou, A. J. Detor, R. DiDomizio, M. J. Mills and Y. Wang, "Growth behavior of γ'/γ" coprecipitates in Ni-Base superalloys," *Acta Materialia,* vol. 164, pp. 220-236, 2019.

[124] F. Zhang, "Ni-Nb-Al pseudo-ternary thermodynamic database," Madison, 2010.

[125] M. Yang, H. Wei, J. Zhang, Y. Zhao, T. Jin, L. Liu and X. F. Sun, "Phase-field study on effects of antiphase domain and elastic energy on evolution of γ′ precipitates in nickel-based superalloys," *Computational Materials Science,* vol. 129, pp. 211-219, 2017.

[126] F. Schleifer, M. Holzinger, Y. Y. Lin, U. Glatzel and M. Fleck, "Phase-field modeling of γ/γ" microstructure formation in Ni-based superalloys with high γ" volume fraction," *Intermetallics,* vol. 120, p. 106745, 2020.

[127] M. Avrami, "Kinetics of phase change. I General theory," *The Journal of chemical physics,* vol. 7, no. 12, pp. 1103-1112, 1939.

[128] M. Avrami, "Kinetics of phase change. II transformation-time relations for random distribution of nuclei," *The Journal of chemical physics,* vol. 8, no. 2, pp. 212-224, 1940.

[129] M. Avrami, "Granulation, phase change, and microstructure kinetics of phase change. III," *The Journal of chemical physics,* vol. 9, no. 2, pp. 177-184, 1941.

[130] E. Kozeschnik, I. Holzer and B. Sonderegger, "On the potential for improving equilibrium thermodynamic databases with kinetic simulations," *Journal of phase equilibria and diffusion,* vol. 28, pp. 64-71, 2007.

[131] L. Q. Chen and J. Shen, "Applications of semi-implicit Fourier-spectral method to phase field equations," *Computer Physics Communications,* vol. 108, pp. 147-158, 1998.

[132] Z. Wang, A. D. Stoica, D. Ma and A. M. Beese, "Diffraction and single-crystal elastic constants of Inconel 625 at room and elevated temperatures determined by neutron diffraction," *Materials Science and Engineering: A,* vol. 674, pp. 406-4012, 2016.

[133] R. Lawitzki, S. Hassan, L. Karge, J. Wagner, D. Wang, J. von Kobylinski, C. Krempaszky, M. Hofmann, R. Gilles and G. Schmitz, "Differentiation of γ′-and γ″-precipitates in Inconel 718 by a complementary study with small-angle neutron scattering and analytical microscopy," *Acta Materialia,* vol. 163, pp. 28-39, 2019.

[134] C. Slama, C. Servant and G. Cizeron, "Aging of the Inconel 718 alloy between 500 and 750 ºC," *Journal of materials research,* vol. 12, pp. 2298-2316, 1997.

[135] R. Y. Zhang, H. L. Qin, Z. N. Bi, J. Li, S. Paul, T. L. Lee, S. Y. Zhang, J. Zhang and H. B. Dong, "Temperature-Dependent Misfit Stress in Gamma Double Prime Strengthened Ni-Base Superalloys," *Metallurgical and Materials Transactions A,* vol. 51, no. 4, pp. 1860-1873, 2020.

[136] I. J. Moore, *Modelling γ" ($D0_{22}$) precipitate nucleation, growth and coarsening in the nickel-base superalloy 625,* PhD thesis: University of Sheffield, 2017.

[137] L. M. Suave, D. Bertheau, J. Cormier, P. Villechaise, A. Soula, Z. Hervier and J. Laigo, "Impact of microstructural evolutions during thermal aging of Alloy 625 on its monotonic mechanical properties," in *MATEC Web of Conferences,* 2014.

[138] N. B. Schmidt, T. A. DeBold and R. B. Frank, "Custom age 625® plus alloy—A higher strength alternative to alloy 625," *Journal of Materials Engineering and Performance,* vol. 1, no. 4, pp. 483-488, 1992.

[139] L.-J. Yu and E. A. Marquis, "Precipitation behavior of Alloy 625 and Alloy 625 plus," *Journal of Alloys and Compounds,* vol. 811, p. 151916, 2019.

[140] M. Sundararaman and P. Mukhopadhyay, "Heterogeneous Precipitation of the γ" Phase in Inconel 625," *Materials Science Forum,* vol. 3, pp. 273-280, 1985.

[141] M. Sundararaman, R. Kishore and P. Mukhopadhyay, "Some aspects of the heterogeneous precipitation of the metastable γ" phase in Alloy 625," *Superalloys 718, 625, 706 and various derivatives,* pp. 405-418, 1994.

[142] R. Shi, T. W. Heo, B. C. Wood and Y. Wang, "Critical nuclei at hetero-phase interfaces," *Acta Materialia,* vol. 200, pp. 510-525, 2020.

[143] H. Liu, Y. Gao, Y. M. Zhu, Y. Wang and J. F. Nie, "A simulation study of β1 precipitation on dislocations in an Mg–rare earth alloy," *Acta materialia,* vol. 77, pp. 133-150, 2014.

[144] J. Oblak, D. Duvall and D. Paulonis, "An estimate of the strengthening arising from coherent, tetragonally-distorted particles," *Materials Science and Engineering,* vol. 13, no. 1, pp. 51-56, 1974.

[145] A. Baldan, "Review Progress in Ostwald ripening theories and their applications to the γ′-precipitates in nickel-base superalloys Part II Nickel-base superalloys," *Journal of materials science,* vol. 37, no. 12, pp. 2379-2405, 2002.

[146] H. Mughrabi, "Microstructural aspects of high temperature deformation of monocrystalline nickel base superalloys: some open problems," *Materials Science and Technology,* vol. 25, no. 2, pp. 191-204, 2009.

[147] S. Meher, M. C. Carroll, T. M. Pollock and L. J. Carroll, "Designing nickel base alloys for microstructural stability through low γ-γ′ interfacial energy and lattice misfit," *Materials & Design,* vol. 140, pp. 249-256, 2018.

[148] A. J. Ardell and R. B. Nicholson, "The coarsening of γ’ in Ni-Al alloys," *Journal of Physics and Chemistry of Solids,* vol. 27, no. 11-12, pp. 1793-1794, 1966.

[149] A. J. Ardell, "An application of the theory of particle coarsening: The γ'precipitate in Ni-Al alloys," *Acta Metallurgica,* vol. 16, no. 4, pp. 511-516, 1968.

[150] P. K. Rastogi and A. J. Ardell, "The coarsening behavior of the γ′ precipitate in nickel-silicon alloys," *Acta Metallurgica,* vol. 19, no. 4, pp. 321-330, 1971.

[151] H. Wendt and P. Haasen, "Nucleation and growth of γ′-Precipitates in Ni-14 at.% Al," *Acta Metallurgica,* vol. 31, no. 10, pp. 1649-1659, 1983.

[152] H. Gleiter and E. Hornbogen, "Precipitation hardening by coherent particles," *Materials science and engineering,* vol. 2, no. 6, pp. 285-302, 1968.

[153] S. Sadiq and D. R. F. West, "The coarsening of γ’ particles in Ni-Al-Mo-Ta and Ni-Al-Mo-W alloys," *Scripta metallurgica,* vol. 19, no. 7, pp. 833-837, 1985.

[154] E. H. Van der Molen, J. M. Oblak and O. H. Kriege, "Control of γ′ particle size and volume fraction in the high temperature superalloy Udimet 700," *Metallurgical Transactions,* vol. 2, no. 6, pp. 1627-1633, 1971.

[155] P. K. Footner and B. P. Richards, "Long—term growth of superalloy γ′ particles," *Journal of Materials Science,* vol. 17, no. 7, pp. 2141-2153, 1982.

[156] D. McLean, "Predicting growth of γ′ in nickel alloys," *Metal science,* vol. 18, no. 5, pp. 249-256, 1984.

[157] I. M. Lifshitz and V. V. Slyozov, "The kinetics of precipitation from supersaturated solid solutions," *Journal of physics and chemistry of solids,* vol. 19, no. 1-2, pp. 35-50, 1961.

[158] C. Wagner, "Theory of precipitate change by redissolution," *Z. Elektrochem,* vol. 65, pp. 581-591, 1961.

[159] H. A. Calderon, P. W. Voorhees, J. L. Murray and G. Kostorz, "Ostwald ripening in concentrated alloys," *Acta metallurgica et materialia,* vol. 42, no. 3, pp. 991-1000, 1994.

[160] Y. F. Han, P. Deb and M. C. Chaturvedi, "Coarsening behaviour of γ″-and γ′-particles in Inconel alloy 718," *Metal Science,* vol. 16, no. 12, pp. 555-562, 1982.

[161] P. W. Voorhees, "The theory of Ostwald ripening," *Journal of Statistical Physics,* vol. 38, no. 1, pp. 231-252, 1985.

[162] A. Baldan, "Review progress in Ostwald ripening theories and their applications to nickel-base superalloys Part I: Ostwald ripening theories," *Journal of materials science,* vol. 37, no. 11, pp. 2171-2202, 2002.

[163] A. J. Ardell, "The effect of volume fraction on particle coarsening: theoretical considerations," *Acta metallurgica,* vol. 20, no. 1, pp. 61-71, 1972.

[164] J. Svoboda and F. D. Fischer, "Generalization of the Lifshitz–Slyozov–Wagner coarsening theory to non-dilute multi-component systems," *Acta materialia,* vol. 79, pp. 304-314, 2014.

[165] P. Streitenberger, "Analytical description of phase coarsening at high volume fractions," *Acta materialia,* vol. 61, no. 13, pp. 5026-5035, 2013.

[166] A. D. Brailsford and P. Wynblatt, "The dependence of Ostwald ripening kinetics on particle volume fraction," *Acta Metallurgica,* vol. 27, no. 3, pp. 489-497, 1979.

[167] C. K. L. Davies, P. Nash and R. N. Stevens, "The effect of volume fraction of precipitate on Ostwald ripening," *Acta metallurgica,* vol. 28, no. 2, pp. 179-189, 1980.

[168] Y. Y. Qiu, "Effect of the Al and Mo on the γ'/γ lattice mismatch and γ' morphology in Ni-based superalloys," *Scripta metallurgica et materialia,* vol. 33, no. 12, pp. 1961-1968, 1995.

[169] J. S. Van Sluytman and T. M. Pollock, "Optimal precipitate shapes in nickel-base γ–γ′ alloys," *Acta Materialia,* vol. 60, no. 4, pp. 1771-1783, 2012.

[170] C. Liu, Y. Li, L. Zhu and S. Shi, "Effect of coherent lattice mismatch on the morphology and kinetics of ordered precipitates," *Journal of Materials Engineering and Performance,* vol. 27, no. 9, pp. 4968-4977, 2018.

[171] A. J. Ardell and R. B. Nicholson, "On the modulated structure of aged Ni-Al alloys: with an Appendix On the elastic interaction between inclusions by JD Eshelby," *Acta metallurgica,* vol. 14, no. 10, pp. 1295-1309, 1966.

[172] V. Vaithyanathan and L. Q. Chen, "Coarsening of ordered intermetallic precipitates with coherency stress," *Acta Materialia,* vol. 50, no. 16, pp. 4061-4073, 2002.

[173] D. M. Kim and A. J. Ardell, "The volume-fraction dependence of Ni3Ti coarsening kinetics-new evidence of anomalous behavior," *Scripta materialia,* vol. 43, no. 4, pp. 381-384, 2000.

[174] T. Miyazaki, K. Seki, M. Doi and T. Kozakai, "Stability bifurcations in the coarsening of precipitates in elastically constrained systems," *Materials Science and Engineering,* vol. 77, pp. 125-132, 1986.

[175] T. Miyazaki and M. Doi, "Shape bifurcations in the coarsening of precipitates in elastically constrained systems," *Materials Science and Engineering,* vol. 110, pp. 175-185, 1989.

[176] A. J. Ardell, " The effects of elastic interactions on precipitate microstructural evolution in elastically inhomogeneous nickel-base alloys," *Philosophical Magazine,* vol. 94, no. 19, pp. 2101-2130, 2014.

[177] M. Cottura, Y. Le Bouar, B. Appolaire and A. Finel, "Role of elastic inhomogeneity in the development of cuboidal microstructures in Ni-based superalloys," *Acta Materialia,* vol. 94, pp. 15-25, 2015.

[178] W. C. Johnson and P. W. Voorhees, "Elastic interaction and stability of misfitting cuboidal inhomogeneities," *Journal of applied physics,* vol. 61, no. 4, pp. 1610-1619, 1987.

[179] H. Nishimori and A. Onuki, "Pattern formation in phase-separating alloys with cubic symmetry," *Physical Review B,* vol. 42, no. 1, p. 980, 1990.

[180] C. Sagui, D. Orlikowski, A. M. Somoza and C. Roland, "Three-dimensional simulations of Ostwald ripening with elastic effects," *Physical Review E,* vol. 58, no. 4, p. R4092, 1998.

[181] S. Y. Hu and L. Q. Chen, "A phase-field model for evolving microstructures with strong elastic inhomogeneity," *Acta materialia,* vol. 49, no. 11, pp. 1879-1890, 2001.

[182] J. Zhu, L. Q. Chen and J. Shen, "Morphological evolution during phase separation and coarsening with strong inhomogeneous elasticity," *Modelling and Simulation in Materials Science and Engineering,* vol. 9, no. 6, p. 499, 2001.

[183] J. D. Eshelby, "The determination of the elastic field of an ellipsoidal inclusion, and related problems," *Proceedings of the royal society of London. Series A. Mathematical and physical sciences,* vol. 241, no. 1226, pp. 376-396, 1957.

[184] A. G. Khachaturyan, S. Semenovskaya and T. Tsakalakos, "Elastic strain energy of inhomogeneous solids," *Physical Review B,* vol. 52, no. 22, p. 15909, 1995.

[185] H. Moulinec and P. Suquet, "A numerical method for computing the overall response of nonlinear composites with complex microstructure," *Computer methods in applied mechanics and engineering,* vol. 157, no. (1-2), pp. 69-94, 1998.

[186] M. P. Gururajan and T. A. Abinandanan, "Phase field study of precipitate rafting under a uniaxial stress," *Acta Materialia,* vol. 55, no. 15, pp. 5015-5026, 2007.

[187] W. Gust, M. B. Hintz, A. Loddwg, H. Odelius and B. Predel, "Impurity diffusion of Al in Ni single crystals studied by secondary ion mass spectrometry (SIMS)," *Physica status solidi,* vol. 64, no. 1, pp. 187-194, 1981.

[188] C. H. Su and P. W. Voorhees, "The dynamics of precipitate evolution in elastically stressed solids—II. Particle alignment," *Acta materialia,* vol. 44, no. 5, pp. 2001-2016, 1996.

[189] M. Doi, "Elasticity effects on the microstructure of alloys containing coherent precipitates," *Progress in Materials,* vol. 40, no. 2, pp. 79-180, 1996.

[190] R. A. MacKay and L. J. Ebert, "The development of γ-γ′ lamellar structures in a nickel-base superalloy during elevated temperature mechanical testing," *Metallurgical Transactions A,* vol. 16, no. 11, pp. 1969-1982, 1985.

[191] P. Caron and T. Khan, "Improvement of creep strength in a nickel-base single-crystal superalloy by heat treatment," *Materials Science and Engineering,* vol. 61, no. 2, pp. 173-184, 1983.

[192] Y. Y. Qiu, "Coarsening kinetics of γ′ precipitates in Ni-Al and Ni-Al-Mo alloys," *Journal of materials science,* vol. 31, no. 16, pp. 4311-4319, 1996.

[193] R. Mukherjee, T. A. Abinandanan and M. P. Gururajan, "Effect of misfit strain and interface curvature," *Acta Materialia,* vol. 57, no. 13, pp. 3947-3954, 2009.

[194] H. J. Ryu, S. H. Hong, J. Weber and J. H. Tundermann, "Effect of elastic interaction energy on coarsening of γ′ precipitates in a mechanically alloyed ODS Ni-base superalloy," *Journal of materials science,* vol. 34, no. 2, pp. 329-336, 1999.

[195] T. Maebashi and M. Doi, "Coarsening behaviours of coherent γ′ and γ precipitates in elastically constrained Ni–Al–Ti alloys," *Materials Science and Engineering: A,* vol. 373, no. 1-2, pp. 72-79, 2004.

[196] M. Berahmand and S. A. Sajjadi, "An investigation on the coarsening behavior of γ′ precipitate in GTD-111 Ni-base superalloy," *Phase Transitions,* vol. 81, no. 1-2, pp. 1-12, 2012.

[197] D. J. Chellman and A. J. Ardell, "The coarsening of γ'precipitates at large volume fractions," *Acta Metallurgica,* vol. 22, no. 5, pp. 577-588, 1974.

[198] C. S. Jayanth and P. Nash, "Experimental evaluation of particle coarsening theories," *Materials science and technology,* vol. 6, no. 5, pp. 405-414, 1990.

[199] P. H. Leo, W. W. Mullins, R. F. Sekerka and J. Vinals, "Effect of elasticity on late stage coarsening," *Acta metallurgica et materialia,* vol. 38, no. 8, pp. 1573-1580, 1990.

[200] T. Mura, Micromechanics of defects in solids, Springer Science & Business Media, 2013.

APPENDIX A

BENCHMARK OF MICROELASTICITY: COMPARISONS OF ANALYTICAL AND NUMERICAL SOLUTIONS

This appendix presents the Fourier spectral method used to solve the mechanical equilibrium (Eq. 4.22), according to the algorithm given by Moulinec and Suquet [185]:

For an elastic inhomogeneous microstructure composed of different phases with stiffness $C_{ijkl}(x)$, the algorithm first considers an auxiliary problem of a homogeneous medium with stiffness C^0_{ijkl} subject to a periodic polarization field $\tau_{ij}(x)$ of which solution can be found in textbooks (e.g., [200]). The solution can be expressed in terms of the Fourier transform of the polarization field by utilizing the Fourier transform of the Green's operator of the following equations (in real space):

$$\begin{aligned} &\sigma_{ij}(x) = C^0_{ijkl}\epsilon_{kl}\big(u^*(x)\big) + \tau_{ij}(x) \\ &div\ \sigma_{ij}(x) = 0, \qquad \sigma_{ij}n_j - \#, \qquad u^*(x)\ \# \end{aligned} \tag{A.1}$$

In Fourier space, these equations can be written as:

$$\begin{aligned} &\hat{\sigma}_{ij}(\xi) = \mathrm{i}C^0_{ijkl}\xi_l\hat{u}^*_k(\xi) + \hat{\tau}_{ij}(\xi) \\ &\mathrm{i}\hat{\sigma}_{ij}(\xi)\xi_j = 0 \end{aligned} \tag{A.2}$$

where ξ is the Fourier frequencies or vectors and $\mathrm{i} = \sqrt{-1}$. Eliminating $\hat{\sigma}_{ij}(\xi)$ between the two equations in (A.2) gives:

$$K^0_{ik}(\xi) \cdot \hat{u}^*_k = \hat{\tau}_{ij}(\xi)\xi_j \tag{A.3}$$

where $K^0(\xi)$ is the acoustic tensor of the homogenous material which is defined as:

$$K^0_{ik}(\xi) = C^0_{ijkl}\xi_l\xi_k \tag{A.4}$$

Then, the displacement field can be expressed as:

$$\hat{u}_k^*(\xi) = \mathrm{i}N_{ki}^0(\xi)\hat{\tau}_{ij}(\xi)\xi_j = \frac{\mathrm{i}}{2}\left(N_{ki}^0(\xi)\xi_j + N_{kj}^0(\xi)\xi_i\right)\hat{\tau}_{ij}(\xi) \tag{A.5}$$

in which the symmetry of τ of has been used and $N^0(\xi)$ represents the inverse of $K^0(\xi)$, i.e.,

$$N^0(\xi) = [K^0(\xi)]^{-1} \tag{A.6}$$

The resulting strain field can then be expressed as:

$$\hat{\epsilon}_{kl}(u^*) = \frac{\mathrm{i}}{2}\left(\xi_l\hat{u}_k^*(\xi) + \xi_k\hat{u}_l^*(\xi)\right) = \hat{\Gamma}_{klij}^0(\xi)\hat{\tau}_{ij}(\xi) \tag{A.7}$$

with

$$\hat{\Gamma}_{klij}^0 = \frac{1}{4}\left[N_{li}^0(\xi)\xi_j\xi_k + N_{ki}^0(\xi)\xi_j\xi_l + N_{lj}^0(\xi)\xi_i\xi_k + N_{kj}^0(\xi)\xi_i\xi_l\right] \tag{A.8}$$

and

$$\hat{\tau}_{ij}(\xi) = \langle\tau_{ij}(x)\mathrm{e}^{-\mathrm{i}\xi,x}\rangle \tag{A.9}$$

The strain field induced at each grid point x of the periodic simulation cell with an initial stress τ can be determined iteratively from Eqs. (A.7), (A.8), and (A.9).

The step-by-step numerical implementation of the algorithm reads as follows:

Initialization:

(a) $\epsilon_{ij}^{(0)}(x) = E_{ij}$

(b) $\sigma_{ij}^{(0)}(x) = C_{ijkl}(x)\epsilon_{kl}^{(0)}(x)$

With $\epsilon_{ij}^{(0)}(x)$ and $\sigma_{ij}^{(0)}(x)$ known at every grid point x, Iteration $(i+1)$ is performed as follows:

(1) $\hat{\sigma}_{ij}^{(i)}(\xi) = FFT\left[\sigma_{ij}^{(i)}(x)\right]$ and $\hat{\epsilon}_{ij}^{(i)}(\xi) = FFT\left[\epsilon_{ij}^{(i)}(x)\right]$

(2) $\hat{\epsilon}_{ij}^{(i+1)}(\xi) = \hat{\epsilon}_{ij}^{(i)}(\xi) - \hat{\Gamma}_{ijkl}(\xi)\hat{\sigma}_{kl}^{(i)}(\xi)$

(3) $\epsilon_{ij}^{(i+1)}(x) = FFT^{-1}\left[\hat{\epsilon}_{ij}^{(i+1)}(\xi)\right]$

(4) $\sigma_{ij}^{(i+1)}(x) = C_{ijkl}(x)\epsilon_{kl}^{(i+1)}(x)$

(5) Check convergence

In the above algorithm, FFT and FFT^{-1}refer to the forward and inverse Fourier transforms of the terms inside the square brackets, respectively. Note that the elastic constants of the reference homogeneous medium, C_{ijkl}^{0}, is typically taken as the arithmetic averages of the elastic constants of the phases. The convergence rate of the algorithm is proportional to the differences in the elastic constants of the phases [185].

Next, the Fourier spectral solver for the microelasticity problem is compared with the analytical solution for an elastically isotropic system $\left(A_z = 1,\ A_Z = \frac{2C_{44}}{C_{11}-C_{12}}\right)$ with a softer precipitate. The elastic constant contrast between the precipitate and the matrix is 50%. The eigenstrain (ϵ^T) value in the particle and matrix is taken to be 0.01 and 0, respectively. The diameter of the particle in the center of the matrix is set as 0.1 of the width of the square domain. The principal stress components (normalized by $C_{44}\epsilon^T$) as a function of normalized distance (r/R) from the center of a circular precipitate along the x-axis is shown in Figure A.1 for both the analytical [200] and numerical solutions. The effect of the domain size and discretization on the results of the numerical solutions is also investigated. It is clear from Figure A.1 that the numerical and analytical solutions are in good agreement. The difference between the mesh sizes is negligible elsewhere, except at the sharp interface between the precipitate and the matrix.

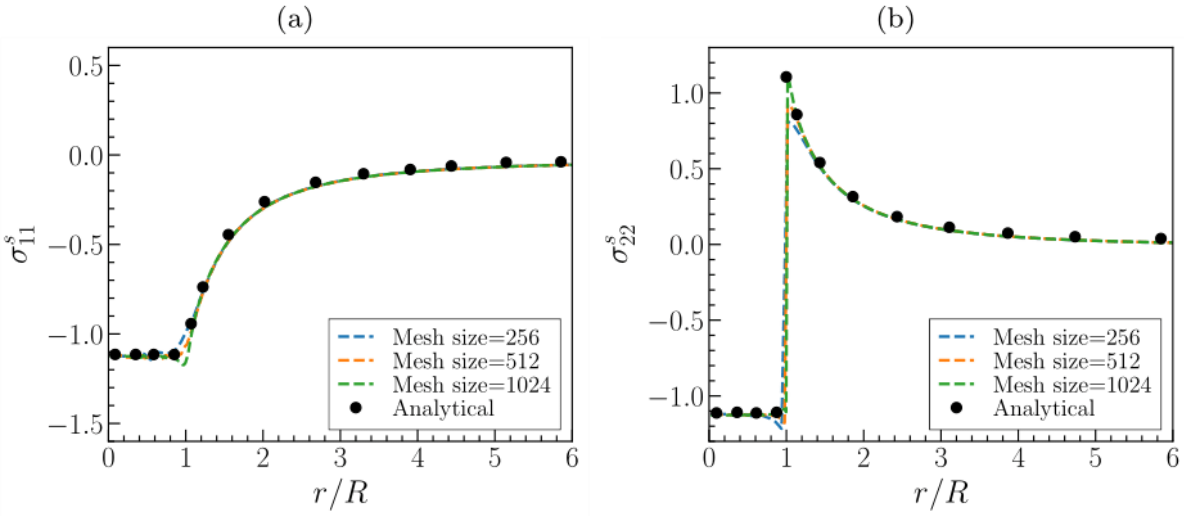

Figure A.1 Comparison of the analytical [200] and numerical solutions for the normalized stress components (a) σ_{11}^s and (b) σ_{22}^s as a function of normalized distance (r/R) along the x-axis, from the center of a circular precipitate. The distance is normalized by R, the precipitate radius, while the stress is normalized by the characteristic stress $(C_{44}\epsilon^T)$. Different domain discretization (256, 512, and 1024) are carried out to test the accuracy of the solver.

APPENDIX B

COMPARISON OF THE CPU AND GPU IMPLEMENTATION OF THE PHASE-FIELD MODEL

This appendix compares the results from the CPU and GPU implementation of the phase-field model. Figure B.1(a) shows the result of the evolution of the diameter of a γ' in a γ matrix for both the CPU and GPU codes. As can be seen from the figure, the results from both codes are in excellent agreement. The speed-up of the CPU code by the GPU is shown in Figure B.1(b). Generally, the speed-up increases with increase in the simulation volume size and a maximum of about 38 times speed-up is seen for a 256^3 simulation volume size.

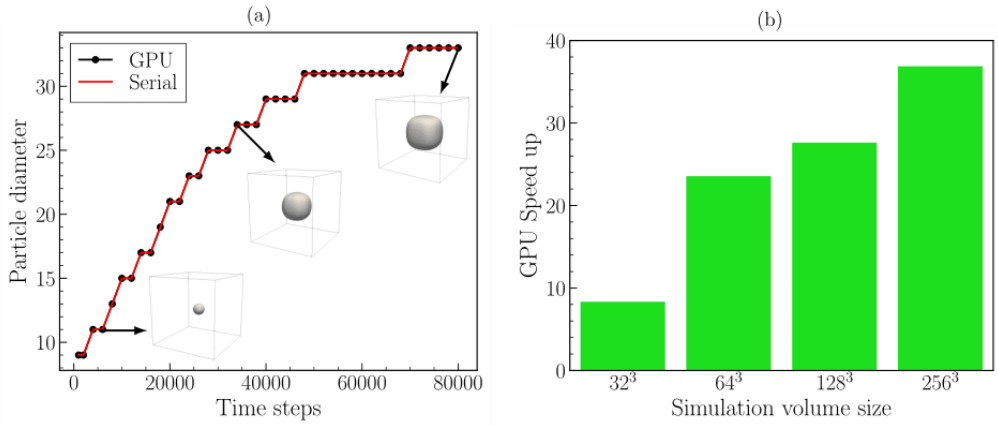

Figure B.1 Benchmark results for the growth of a single γ' particle in a γ matrix. (a) Comparison of the result obtained by the serial CPU code with the GPU code. (b) GPU speed up of the serial code as a function of simulation volume size.

Note: Serial tests were performed on 1 Intel Xeon CPU E5-2680 at 2.70GHz using Fortran codes and Intel/2019.5 compiler. GPU tests were performed on 1 NVIDIA Tesla K20m GPU using CUDA-Fortran codes and PGI/2020 compiler.